Application of an overdamped Langevin dynamics to the study of microstructural evolutions in crystalline materials

Carolina Baruffi

Application of an Overdamped Langevin Dynamics to the study of microstructural evolutions in crystalline materials

École doctorale: 397-Paris 6, Université Paris Sorbonne

THÈSE DE DOCTORAT

pour obtenir le grade de :
DOCTEUR EN PHYSIQUE ET CHIMIE DES MATERIAUX

présentée par

Carolina Baruffi

soutenue le 17 décembre 2018

Jury

Emmanuel Clouet	SRMP (CEA)	Rapporteur
Frédéric Mompiou	CEMES (CNRS, Université Paul Sabatier)	Rapporteur
Maurine Montagnat	IGE (CNRS, UGA)	Examinatrice
Philippe Vermaut	IRCP (CNRS, ChimieParisTech)	Examinateur
Marc Fivel	SIMaP (CNRS, INP Grenoble)	Examinateur
Alphonse Finel	LEM (CNRS, Onera)	Directeur de thèse
Brigitte Bacroix	LSPM (CNRS, Université Paris 13)	Co-directrice de thèse
Oguz Umut Salman	LSPM (CNRS, Université Paris 13)	Encadrant

Alle mie nonne

Contents

List of Figures

List of Tables

Résumé en français

Les propriétés macroscopiques des metaux et des alliages métalliques (telles que la résistance, la ductilité, la ténacité, la résistance à la corrosion et plusieurs autres) dépendent fortement de leur microstructure. La taille des grains avec leurs formes et orientations, la présence de précipités ou de phases différentes sont tous des facteurs qui influencent les propriétés mécaniques d'un matériau. Par conséquent, la compréhension de l'évolution de la microstructure dans des conditions thermomécaniques données est fondamentale pour prévoir ses propriétés finales ou pour développer de nouveaux matériaux à hautes performances. À cet effet la modélisation numérique est un instrument puissant. Plusieurs techniques de modélisation à l'échelle *macro* et *meso*scopique ont été proposées au cours des dernières décennies pour l'étude de la plasticité cristalline, de la recristallisation et des transformations de phase. La capacité de ces approches (qui ont l'avantage de donner accès à des échelles de temps et espace relativement grandes) à saisir les caractéristiques essentielles des phénomènes listés plus haut et à être prédictifs repose sur des lois phénoménologiques et des quantités moyennes utilisées dans leur formulation. Afin de définir ces lois et paramètres, nous devons étudier les mécanismes qui régissent l'évolution de la microstructure à l'échelle *microscopique*. Ce besoin a conduit ces dernières années à un intérêt croissant pour les techniques empiriques de modélisation atomistique, parmi lesquelles l'une des plus largement utilisées est la Dynamique Moléculaire.

La Dynamique Moléculaire (DM) repose sur l'hypothèse de Born-Oppenheimer selon laquelle les électrons peuvent répondre instantanément aux changements de position des noyaux. Les noyaux peuvent alors être traités comme des particules classiques et leurs trajectoires obtenues par intégration des équations de Newton. Cette approche de modélisation présente l'avantage de prendre en compte la nature discrète de la matière et donc d'incorporer automatiquement dans sa formulation tous les processus agissant à l'échelle atomique (tels que la diffusione des lacunes, le glissement et la montée des dislocations, la migration des interfaces, la nucleation et propagation des microfissures) sans qu'aucune hypothèse *a priori* ne soit nécessaire sur leur dynamique. Cependant, il présente également certains

inconvénients. Outre la difficulté à définir le potentiel permettant de décrire les interactions entre atomes, les inconvénients majeurs de la DM sont la limitation des échelles de temps et espaces accessibles. Effectivement, la présence de vibrations à haute fréquence (phonons acoustiques et optiques) nécéssite l'utilisation de pas d'integration de l'ordre de la femtoseconde, ce que limite l'échelle de temps observée à quelques nanosecondes et, au quotidien, le nombre d'atomes considérés typiquement à 10^6 particules i.e. des dimensions linéaires de quelques dizaine de nanomètres.

La présente thèse traite explicitement de la problématique liée à la limite sur l'echelle temporelle caractérisante les techniques de modélisation atomistique. Afin de circonvenir la problématique des phonons, nous proposons l'utilisation d'une dynamique de Langevin suramortie pour décrire l'évolution temporelle des trajectoires atomiques dans les matériaux cristallins. Avec cette dynamique, les vibrations ne sont pas explicitement représentées en raison de la nature du premier ordre des équations utilisées et leur effet sur l'évolution du système est intégré dans le bruit stochastique. À notre connaissance, c'est la première fois que la dynamique de Langevin suramortie est appliquée dans ce contexte de la physique des materiaux. Par conséquent, l'objectif principal de cette thèse a été d'étudier les potentialités de cette méthode en l'appliquant à deux des processus susmentionnés qui régissent l'évolution de la microstructure dans les métaux: la migration des joints des grains et les transformations de phase. Ce travail a également nécessité un effort numérique important, consistant d'une part à développer un code Fortran pour l'implémentation de la dynamique de Langevin dans différents ensembles thermodynamiques utilisant un potentiel interatomique à plusieurs corps et, d'autre part, à analyser diverses méthodes numériques pour l'intégration des équations différentielles stochastiques.

Chapter 1

Introduction

The subject of this thesis is the development and application of a novel approach proposed for the atomistic modelling of crystalline materials. In this chapter, we present the general context of our studies and the main objectives of the work done.

1.1 General context

Macroscopic properties of metals and metallic alloys (such as strength, ductility, toughness, corrosion resistance) are strongly dependent on their microstructure, e.g. grain sizes and shapes, type and number of defects. This microstructure is usually the result of a series of thermo-mechanical treatments during which different processes contribute to the microstructural evolution. The ones which are considered the most relevant in physical metallurgy are [6]:

1. *plastic activity*, which involves dislocation generation, propagation and reaction;

2. *recrystallization*, which contributes to the regeneration of the microstructure by new grain nucleation, grain growth *via* grain boundary migration and defects rearrangement and/or annealing;

3. structural transformations such as *phase transition* and *precipitation*.

In this context, modelisation at the *macro* and *meso*-scale is a powerful instrument to understand how the microstructure evolves and thus to predict final mechanical properties or to develop new high-performances materials. Some modelling techniques frequently used are: continuum crystal plasticity models [7], phase field methods [8], Vertex and Monte Carlo pots models [9], Discrete Dislocations Dynamics [10]. All the models listed above have the advantage of giving access to the

simulation of rather large length and time scales. On the other side, the definition of the phenomenological laws and averaged quantities used in their formulation requires the understanding of the *microscopic* processes which drive dislocation dynamics, grain boundary migration and phase transformation. This need has lead to a growing interest in empirical atomistic models which take into account the discrete nature of matter. At present, one of the best known and most used atomistic modelling technique is Molecular Dynamics.

Molecular Dynamics (MD) relies on the Born-Oppenheimer hypothesis which states that electrons can always respond instantaneously to changes in the atomic positions. A consequence of this hypothesis is that we can write an Hamiltonian H just for the nuclei and embody the effect of electrons in a potential energy function Φ dependent only on nuclear positions. The nuclei are then treated as classical particles and their trajectory is determined by integration of Newton equations of motion [11]. MD has the advantage of automatically incorporate in its formulation all processes acting at the atomistic length scale (such as dislocation glide and climb, diffusion, interface motion) without the need of making any hypothesis *a priori* on their dynamics. The elaboration of interatomic potentials able to reproduce the thermodynamical properties of a specific material or a particular phenomenon is a complex task but there has been several progress in the field with the development of new many-body potentials in early 90's [12, 13]. The major drawbacks of MD is the limitation on the accessible length and time scales. The necessity of memorizing the position and velocity of each atom bounds typical simulations to 10^6 particles (which is equivalent to tens of nanometres). Also, the presence of high-frequency vibrations (phonons) restricts the integration time step to the order of the femtosecond, thus allowing the simulation of only a few nanoseconds with reasonable computational cost.

Several extensions of the original MD have been proposed, such as the Voter's *hyperdynamics* [14] which provides an accelerated scheme that incorporates directly thermal effects or the Laio and Parrinello's *metadynamics* [15] which consists in computing free energy barriers. Most of these approaches rely on the Transition State Theory (TST), which basically consists in treating rare events as Markov processes. Therefore, it is natural to look at other methods that are directly and fully based on the TST, such as Monte Carlo methods or stochastic overdamped dynamics which do not incorporate inertia and, consequently, automatically exclude lattice vibrations.

Indeed, different methods have been developed in the past to get rid of the time scale associated to phonons and to reach time scales associated to diffusion.

At the end of the century, a continuous atomic-scale method, the *Phase Field Crystal* method (PFC), has been introduced [16]. It consists in following the evo-

lution of the atomic density, whose maxima correspond to the positions of atoms. The method is attractive as, despite its simplicity, it automatically incorporates elastic effects, multiple crystal orientation and the nucleation and motion of dislocations. Also, as the dynamics is purely dissipative, it gives access (at least in principle) to diffusive time scales. However, being continuous by nature, the numerical implementation requires the use of a grid with grid spacing much smaller than the smallest length scale incorporated in the model, i.e. the atomic size. Therefore, the method is drastically limited to very small systems.

Another methodology is based on the fact that, at low enough temperature, diffusion events take place at a small rate and, therefore, these events can be considered as Markov processes. This is at the root of the so-called *Kinetic Monte Carlo* method (KMC), which consists in following a Markov chain with a catalog of predefined diffusion mechanisms to compute at every time step the escape rate from a local minimum [17, 18]. However, since this catalog is predefined, the system under study as to be discretized and atomic positions limited to fixed lattice sites. In order to extend KMC to long-range elastic effects and, more importantly, to disordered or distorted configurations (amorphous or liquid state, dislocations, cracks, ...), various off-lattice versions have been developed. Among them, we mention the k-ART method, which stands for "*kinetic Activation-Relaxation Technique*" [19]. This is an off-lattice KMC in which the energy barriers are evaluated "on-the-fly", which relaxes the need for a *predefined* catalog. However, the method still relies on a catalog of events which, now, is not predefined but grows along the route of the Markov chain. The updating of this catalog and its use are rather complex (see for example [20]). As example, starting from a local minimum, the generation of the transition path associated to a new event requires the random identification of the direction of the lowest local instability and the identification of the subsequent path to the nearest saddle point while the energy is minimized in the hyperplane orthogonal to this direction. All together, these steps require a few hundreds (typically 600 to 800) forces evaluation.

The overdamped Langevin method proposed below and the ART KMC belong to the same category, as both rely on Markov dynamics applied to atomic positions. Therefore, they should give access to the same time scales. However, the overdamped Langevin method is much simpler to use, because it does not require the delicate creation and continous updating of a catalog of events.

1.2 Objectives and outline of the thesis

The present thesis explicitly addresses the time scale limit problematic characterizing atomistic modelling techniques. In order to get rid of phonons, we propose the use of an overdamped Langevin dynamics to describe the time evolution of

atomic trajectories in crystalline materials. With this dynamics, high-frequency vibrations are not explicitly represented because of the first-order in time nature of equations and their effect on the system evolution is embedded in the stochastic noise. To our knowledge, it is the first time that the overdamped Langevin dynamics has been applied in the present context. Consequently, the main objective of this thesis has been the investigation of the potentialities of this method by its application to two of the above mentioned processes which govern the microstructural evolution in metals, i.e. grain boundary migration and phase transition. This work has also required a relevant effort from a numerical point of view, which has consisted in: (i) the development of a Fortran code that integrates the Langevin dynamics in different thermodynamical ensembles, (ii) the implementation of a spline-formulated many-body potential and (iii) the analysis of various numerical methods for the time integration of stochastic differential equations.

The thesis is organized as follows:

- the theoretical formulation of the overdamped Langevin dynamics in different thermodynamical ensembles is presented in chapter 2, together with an heuristic justification of its validity;

- chapter 3 deals with the numerical implementation of the model i.e. with the tests of different method for integrating the stochastic differential equations and with the algorithms used for interatomic force calculation;

- in chapter 4 we present a first application of the overdamped Langevin dynamics to the study of grain boundary motion in a 2D Lennard-Jones solid. The main purpose of this study as been the validation of the model by comparing our results with the ones obtained with Molecular Dynamics. However, it has also been the occasion for investigating some particular migration mechanisms characterizing low angle and high angle tilt grain boundaries;

- chapter 5 is devoted to the analysis of the temperature induced $\beta \rightarrow \alpha$ phase transition in pure Titanium, with particular attention on the effect of mechanical constraints in the final microstructural morphology and variant selectivity;

- finally, chapter 6 is dedicated to conclusions and perspectives for future work and route of progresses in this still to-be-explored theory for the atomistic modelling of crystalline materials.

Chapter 2

Modelling approach: overdamped Langevin dynamics for crystalline materials

2.1 Introduction

In this chapter we describe the modelling approach proposed, whose main objective is to avoid the short time scale associated with phonons. In order to do this, a first order in time stochastic dynamics is proposed. A heuristic justification of the hypothesis at the base of the present approach is then given.

2.2 Preliminaries: Langevin equations and statistical physics

Let $\{\phi_i\}$ be a set of stochastic variables and $E(\{\phi_i\})$ be a potential function. Consider that the set $\{\phi_i\}$ follows the following dynamics:

$$\forall i: \quad \frac{\partial \phi_i}{\partial t} = -\nu_i \frac{\partial E}{\partial \phi_i} + B_i \eta_i(t) \tag{2.2.1}$$

where the mobilities ν_i and noise amplitudes B_i are constant (they do not depend on $\{\phi_i\}$, nor on t) and the stochastic terms $\eta_i(t)$ are independent and white Gaussian variables:

$$\begin{cases} \langle \eta_i(t) \rangle = 0 \\ \langle \eta_i(t) \eta_j(t') \rangle = \delta_{ij} \delta(t - t') \end{cases} \tag{2.2.2}$$

with δ_{ij} and $\delta(t - t')$ symbolizing the Kronecker and the Dirac delta respectively. We remark that:

- equations (2.2.1) are a particular case of the general Langevin equation, in which the mobilities ν_i and the noise amplitudes B_i may depend on $\{\phi_i\}$;
- as B_i is constant, the Itô and Stratonovich calculus are identical (see chapter 3, section 3.2.1).

The set of equations (2.2.1) is equivalent to the following Fokker-Planck equation [21]:

$$\frac{dP(\{\phi_i\})}{dt} = \sum_i \frac{\partial}{\partial \phi_i}\left[\nu_i \frac{\partial E}{\partial \phi_i} P(\{\phi_i\})\right] + \frac{1}{2}\sum_i \frac{\partial^2}{\partial \phi_i^2}\left[B_i^2 P(\{\phi_i\})\right] \tag{2.2.3}$$

where $P(\{\phi_i\})$ is the (time-dependent) probability distribution for the set $\{\phi_i\}$.

We consider the case in which the noise term amplitudes are proportional to the square root of the mobility terms:

$$\forall i: \quad B_i^2 = 2\alpha\nu_i \tag{2.2.4}$$

Then, if we suppose to have "natural boundary conditions", i.e:

$$\lim_{\phi_i \to \infty} P(\{\phi_i\}) = 0 \tag{2.2.5}$$

and if we restrict to integrable probabilities densities, it is straightforward to show that the Fokker-Planck equation (2.2.3) admits *only one* fixed point, given by:

$$\begin{aligned} P_{fixed}(\{\phi_i\}) &= A \exp\left(-\frac{E(\{\phi_i\})}{\alpha}\right) \\ A^{-1} &= \int \exp\left(-\frac{E(\{\phi_i\})}{\alpha}\right) \prod_i d\phi_i \end{aligned} \tag{2.2.6}$$

Hence, to recover Gibb's equilibrium, we just need to choose:

$$\alpha = k_B T$$

where k_B is the Boltzmann constant and T is the temperature.

In summary, the non-linear Langevin equations:

$$\forall i: \quad \frac{\partial \phi_i}{\partial t} = -\nu_i \frac{\partial E}{\partial \phi_i} + \sqrt{2k_B T \nu_i}\eta_i(t)$$

with independent white Gaussian noises:

$$\begin{cases} \langle \eta_i(t) \rangle = 0 \\ \langle \eta_i(t)\eta_j(t') \rangle = \delta_{ij}\delta(t-t') \end{cases}$$

converge to the Gibb's equilibrium:

$$t \to \infty : \; P_{eq}(\{\phi_i\}) = A \exp\left(-\frac{E(\{\phi_i\})}{k_B T}\right)$$
$$A^{-1} = \int \exp\left(-\frac{E(\{\phi_i\})}{k_B T}\right) \prod_i d\phi_i$$

Therefore, provided that a first-order in time kinetics may be suitable for the dynamic process we want to follow, the Langevin approach offers a well-defined framework that guarantees convergence to the correct equilibrium state.

2.3 Overdamped Langevin dynamics in the (NVT) ensemble

We consider a crystalline system composed of N atoms with coordinates x_i^n, where the upper index $n = 1, \ldots, N$ refers to a particle and the lower index $i = 1, 2, 3$ to a cartesian coordinate. We suppose that the particles interact through a potential $\Phi(\{x_i^n\})$ and we consider the following first-order in time stochastic dynamics:

$$\frac{dx_i^n}{dt} = -\nu \frac{\partial \Phi}{\partial x_i^n} + B\eta_i^n(t), \tag{2.3.1}$$

where ν is a mobility coefficient and B the amplitude of a white Gaussian noise $\eta_i^n(t)$ such that:

$$\begin{cases} \langle \eta_i^n(t) \rangle = 0 \\ \langle \eta_i^n(t) \eta_j^m(t') \rangle = \delta_{nm}\delta_{ij}\delta(t - t') \end{cases} \tag{2.3.2}$$

with δ_{nm} and δ_{ij} symbolizing the Kronecker delta and $\delta(t - t')$ symbolizing the Dirac delta. The coefficients ν and B are supposed to be constant and independent from particle positions. The N particles are restricted to stay within a fixed volume V by applying periodic boundary conditions on the coordinates $\{x_i^n\}$.

As recalled in section 2.2, the set of equations (2.3.1) is formally equivalent to the following Fokker-Planck equation:

$$\frac{dP(\{x_i^n\})}{dt} = \sum_{n=1}^{N} \sum_{i=1}^{3} \frac{\partial}{\partial x_i^n} \left[\nu \frac{\partial \Phi}{\partial x_i^n} P(\{x_i^n\})\right] + \frac{1}{2} \frac{\partial^2}{\partial x_i^n \partial x_i^n} \left[B^2 P(\{x_i^n\})\right] \tag{2.3.3}$$

which in the long-time limit converges to the steady-state solution:

$$t \to \infty : \; P_{eq}(\{x_i^n\}) = A \exp\left(-\frac{2\nu\Phi(\{x_i^n\})}{B^2}\right) \tag{2.3.4}$$

$$A^{-1} = \int \exp\left(-\frac{2\nu\Phi(\{x_i^n\})}{B^2}\right) \prod_{n=1}^{N} \prod_{i}^{3} dx_i^n$$

This steady state solution corresponds to the Boltzmann equilibrium distribution in the (NVT) thermodynamical ensemble if and only if the mobility coefficient ν and the noise amplitude B are related by the fluctuation-dissipation relation:

$$B = \sqrt{2k_b T\nu}. \tag{2.3.5}$$

Therefore, under this condition, the dynamics given in Eq. 2.3.1 converges to the correct thermodynamical state in the long-time limit.

2.4 Overdamped Langevin dynamics in the (NPT) ensemble

The set of equations (2.3.1) allows the simulation of a system in fixed volume and fixed temperature conditions. However, when working with crystalline materials, we usually want to control the temperature and the stress applied while leaving the specimen free of changing its shape and/or volume. In this section we explain how we extended the dynamics to the (N**P**T) ensemble, where **P** symbolizes the first Piola-Kirchhoff stress tensor. Our procedure is similar in spirit to the one developed by Parrinello and Rahman for classical MD [22].

We need to augment our set of $3N$ DOFs by adding variables to define the shape and volume of the simulation box. At each instant t, the box is supposed to be a parallelepiped defined by three non-coplanar vectors $\mathbf{L}_1(t), \mathbf{L}_2(t), \mathbf{L}_3(t)$. In the hypothesis of homogeneous deformation, we can describe its change in shape *via* a deformation gradient $\mathbf{F}(t)$ so that at each istant t:

$$(\mathbf{L}_\alpha)_i(t) = F_{ij}(\mathbf{L}_\alpha^0)_j \quad \alpha = 1, 2, 3 \tag{2.4.1}$$

where the vectors $\mathbf{L}_\alpha^0 = \mathbf{L}_\alpha(0)$ define the reference configuration and Einstein's summation convention is implied. We choose as additional variables the nine components F_{ij} of the deformation gradient tensor. We need to introduce a coupling between the dynamics on atoms positions and the one on these new DOFs. In order to do this, we define a new set of variables by the following transformation:

$$\tilde{x}_i^n = (G^{-1})_{ij} x_j^n \tag{2.4.2}$$

where $\mathbf{G} = \mathbf{FL}$ and $\mathbf{L}$ is a constant diagonal matrix with components:

$$L_{\alpha\alpha} = \| \mathbf{L}^0_\alpha \|$$

We will refer to the variables $\tilde{x}^n_i$ as "scaled coordinates". We associate to the change in shape of the simulation box the potential energy:

$$U = V_0 P_{\alpha\beta} F_{\alpha\beta} \tag{2.4.3}$$

where $\mathbf{P}$ denotes the first Piola-Kirchhoff stress tensor and V_0 the volume in the reference configuration. From a mechanical point of view, the quantity U corresponds to the strain energy associated to an impose stress. By considering this additional contribution, we define a potential energy for the extended system of $(3N + 9)$ DOFs:

$$\begin{aligned} H(\{\tilde{x}^n_i, F_{\alpha\beta}\}) &= \Phi(\{x^n_i\}) + V_0 P_{\alpha\beta} F_{\alpha\beta} \\ &= \Phi(\{\tilde{x}^n_i, F_{\alpha\beta}\}) + V_0 P_{\alpha\beta} F_{\alpha\beta} \end{aligned} \tag{2.4.4}$$

where H corresponds to the enthalpy of the system.

2.4.1 First tentative of an overdamped Langevin dynamics

Let's consider the following overdamped Langevin dynamics on $\{\tilde{x}^n_i, F_{\alpha,\beta}\}$:

$$\frac{\partial \tilde{x}^n_i}{\partial t} = -\nu \frac{\partial H}{\partial \tilde{x}^n_i} + B\eta^n_i(t) \tag{2.4.5}$$

$$\frac{\partial F_{\alpha\beta}}{\partial t} = -\gamma \frac{\partial H}{\partial F_{\alpha\beta}} + A\zeta_{\alpha\beta}(t) \tag{2.4.6}$$

where $\eta^n_i(t)$ and $\zeta_{\alpha\beta}$ are white Gaussian noise terms defined by:

$$\begin{cases} \langle \eta^n_i(t) \rangle = 0 \\ \langle \zeta_{\alpha\beta}(t) \rangle = 0 \\ \langle \eta^n_i(t) \eta^m_j(t') \rangle = \delta_{ij}\delta_{nm}\delta(t - t') \\ \langle \zeta_{\alpha\beta}(t) \zeta_{\gamma\eta}(t') \rangle = \delta_{\alpha\gamma}\delta_{\beta\eta}\delta(t - t') \\ \langle \eta^n_i(t) \zeta_{\alpha\beta}(t') \rangle = 0 \end{cases} \tag{2.4.7}$$

Using an obvious generalization of equation (2.3.5), we impose that the noise amplitudes B and A respect the fluctuation-dissipation relations:

$$B = \sqrt{2k_b T \nu}$$

$$A = \sqrt{2k_b T \gamma}$$

Then, in the long-time limit equations (2.4.5) and (2.4.6) converge to the steady-state solution:

$$t \to \infty : \ \tilde{P}_{eq}(\{\tilde{x}_i^n, F_{\alpha\beta}\}) = \tilde{Z} \exp\left(-\frac{H(\{\tilde{x}_i^n, F_{\alpha\beta}\})}{k_B T}\right) \tag{2.4.8}$$

$$\tilde{Z}^{-1} = \int \exp\left(-\frac{H(\{\tilde{x}_i^n, F_{\alpha\beta}\})}{k_B T}\right) \prod_{n=1}^{N} \prod_{i=1}^{3} d\tilde{x}_i^n \prod_{\alpha,\beta=1}^{3} dF_{\alpha\beta}$$

The probability of observing a given state $(\tilde{x}_i^n, \mathbf{F})$ within the infinitesimal volume $\prod_{n=1}^{N} \prod_{i=1}^{3} d\tilde{x}_i^n \prod_{\alpha,\beta}^{3} dF_{\alpha\beta}$ in the new scaled phase space is given by the expression:

$$d\tilde{P}(\{\tilde{x}_i^n, F_{\alpha\beta}\}) = \tilde{P}_{eq}(\{x_i^n, F_{\alpha\beta}\}) \prod_{n=1}^{N} \prod_{i=1}^{3} d\tilde{x}_i^n \prod_{\alpha,\beta=1}^{3} dF_{\alpha\beta} \tag{2.4.9}$$

Now, if $P_{eq}(\{x_i^n, F_{\alpha\beta}\})$ is the equilibrium probability density defined in the original configurational phase space $\{x_i^n, F_{\alpha\beta}\}$, we must have:

$$\tilde{P}_{eq}(\{\tilde{x}_i^n, F_{\alpha\beta}\}) \prod_{n=1}^{N} \prod_{i=1}^{3} d\tilde{x}_i^n \prod_{\alpha,\beta=1}^{3} dF_{\alpha\beta} = P_{eq}(\{x_i^n, F_{\alpha\beta}\}) \prod_{n=1}^{N} \prod_{i=1}^{3} dx_i^n \prod_{\alpha,\beta=1}^{3} dF_{\alpha\beta} \tag{2.4.10}$$

where the scaled coordinates $\{\tilde{x}_i^n\}$ and unscaled coordinates $\{x_i^n\}$ are linked by equation (2.4.2). Therefore, we have:

$$dx_1^n dx_2^n dx_3^n = \det \mathbf{G} d\tilde{x}_1^n d\tilde{x}_2^n d\tilde{x}_3^n = V_0 \det \mathbf{F} d\tilde{x}_1^n d\tilde{x}_2^n d\tilde{x}_3^n \tag{2.4.11}$$

Substituting equation (2.4.11) in equation (2.4.10), we obtain:

$$\tilde{P}_{eq}(\{\tilde{x}_i^n, F_{\alpha\beta}\}) \prod_{n=1}^{N} \prod_{i=1}^{3} d\tilde{x}_i^n \prod_{\alpha,\beta=1}^{3} dF_{\alpha\beta} = P_{eq}(\{x_i^n, F_{\alpha\beta}\}) \prod_{n=1}^{N} \prod_{i=1}^{3} d\tilde{x}_i^n \prod_{\alpha,\beta=1}^{3} dF_{\alpha\beta} (V_0 \det \mathbf{F})^N \tag{2.4.12}$$

which with equation (2.4.8) leads to:

$$P_{eq}(\{x_i^n, F_{\alpha\beta}\}) = \tilde{Z} \exp\left(-\frac{H(\{\tilde{x}_i^n, F_{\alpha\beta}\})}{k_B T}\right) (V_0 \det \mathbf{F})^{-N} \tag{2.4.13}$$

$$= \tilde{Z} \exp\left(-\frac{H}{k_B T} - N \ln(V_0 \det \mathbf{F})\right) \tag{2.4.14}$$

which *does not* correspond to the Boltzmann distribution.

In conclusion, if we use the expression (2.4.4) for the enthalpy H in the dynamics (2.4.5) we do not recover the expected Boltzmann equilibrium distribution in the long-time limit.

2.4.2 Second tentative of an overdamped Langevin dynamics

In order to correct for the extra term $(N \ln(V_0 \det \mathbf{F}))$ in equation (2.4.14), we define an "extended enthalpy":

$$\overline{H} = H - N k_B T \ln(V_0 \det \mathbf{F}) = \Phi(\{x_i^n\}) + V_0 \, P_{\alpha\beta} \, F_{\alpha\beta} - N k_B T \ln(V_0 \det \mathbf{F}) \quad (2.4.15)$$

and we replace the Langevin equations (2.4.5) and (2.4.6) by new ones:

$$\frac{\partial \tilde{x}_i^n}{\partial t} = -\nu \frac{\partial \overline{H}}{\partial \tilde{x}_i^n} + B\eta_i^n(t) \quad (2.4.16)$$

$$\frac{\partial F_{\alpha\beta}}{\partial t} = -\gamma \frac{\partial \overline{H}}{\partial F_{\alpha\beta}} + A\zeta_{\alpha\beta}(t) \quad (2.4.17)$$

The new equilibrium probability density is then:

$$\tilde{P}_{eq}^{ext}(\{\tilde{x}_i^n, F_{\alpha\beta}\}) = \tilde{Z}^{ext} \exp\left(-\frac{\overline{H}(\{\tilde{x}_i^n, F_{\alpha\beta}\})}{k_B T}\right) \quad (2.4.18)$$

$$(\tilde{Z}^{ext})^{-1} = \int \exp\left(-\frac{\overline{H}(\{\tilde{x}_i^n, F_{\alpha\beta}\})}{k_B T}\right) \prod_{n=1}^{N} \prod_{i=1}^{3} d\tilde{x}_i^n \prod_{\alpha,\beta=1}^{3} dF_{\alpha\beta}$$

In the original unscaled configurational space, this leads to the following probability density:

$$\begin{aligned} P_{eq}(\{x_i^n, F_{\alpha\beta}\}) &= \tilde{Z}^{ext} \exp\left(-\frac{\overline{H}(\{\tilde{x}_i^n, F_{\alpha\beta}\})}{k_B T} - N \ln(V_0 \det \mathbf{F})\right) \quad (2.4.19) \\ &= \tilde{Z}^{ext} \exp\left(-\frac{H(\{x_i^n, F_{\alpha\beta}\})}{k_B T} + N \ln(V_0 \det \mathbf{F}) - N \ln(V_0 \det \mathbf{F})\right) \\ &= \tilde{Z}^{ext} \exp\left(-\frac{H(\{x_i^n, F_{\alpha\beta}\})}{k_B T}\right) \end{aligned}$$

where:

$$\begin{aligned} \tilde{Z}^{ext} &= \int \exp\left(-\frac{\overline{H}}{k_B T}\right) \prod_{n=1}^{N} \prod_{i=1}^{3} d\tilde{x}_i^n \prod_{\alpha,\beta=1}^{3} dF_{\alpha\beta} \quad (2.4.20) \\ &= \int \exp\left(-\frac{H}{k_B T} + N \ln(V_0 \det \mathbf{F})\right) (V_0 \det \mathbf{F})^{-N} \prod_{n=1}^{N} \prod_{i=1}^{3} dx_i^n \prod_{\alpha,\beta=1}^{3} dF_{\alpha\beta} \\ &= \int \exp\left(-\frac{H}{k_B T}\right) \prod_{n=1}^{N} \prod_{i=1}^{3} dx_i^n \prod_{\alpha,\beta=1}^{3} dF_{\alpha\beta} = Z \end{aligned}$$

Hence the density $P_{eq}(\{x_i^n, F_{\alpha\beta}\})$ may be written as:

$$P_{eq}(\{x_i^n, F_{\alpha\beta}\}) = Z \exp\left(-\frac{H(\{x_i^n, F_{\alpha\beta}\})}{k_B T}\right) \tag{2.4.21}$$
$$Z^{-1} = \int \exp\left(-\frac{H}{k_B T}\right) \prod_{n=1}^{N} \prod_{i=1}^{3} dx_i^n \prod_{\alpha,\beta=1}^{3} dF_{\alpha\beta}$$

which corresponds to the expected Boltzmann distribution.

In conclusion, the correct Langevin dynamics in the (N**P**T) ensemble is given by equations (2.4.16) and (2.4.17) in which the driving forces must be extracted from the extended enthalpy defined in equation (2.4.15).

2.4.3 Driving forces in the configurational space $\{x_i^n, F_{\alpha\beta}\}$

We now derive the expression of the forces acting on atoms and the ones associated with the change in the box shape. Combining the definition of scaled coordinates with the expression of $\overline{H}$ we obtain the three components of the force acting on the atom n:

$$\begin{aligned} \frac{\partial \overline{H}}{\partial \tilde{x}_i^n} &= \frac{\partial}{\partial \tilde{x}_i^n}\left(\Phi(\{x_i^n\}) + V_0 P_{\alpha,\beta} F_{\alpha\beta} - N k_B T \ln(V_0 \det \mathbf{F})\right) \\ &= \frac{\partial \Phi}{\partial \tilde{x}_i^n} = \frac{\partial \Phi}{\partial x_l^n} G_{li} \end{aligned} \tag{2.4.22}$$

Next, considering that:

$$\frac{\partial x_i^n}{\partial F_{\alpha\beta}} = \delta_{i\alpha} L_\beta \tilde{x}_\beta^n \tag{2.4.23}$$

and that the determinant of $\mathbf{F}$ can be expressed in function of its cofactors $C_{\alpha\beta}$ as:

$$\det \mathbf{F} = \sum_{\beta=1}^{3} (-1)^{\alpha+\beta} F_{\alpha\beta} C_{\alpha\beta} \tag{2.4.24}$$

we obtain the following expression for the forces acting on the deformation gradient components $F_{\alpha\beta}$:

$$\begin{aligned} \frac{\partial \overline{H}}{\partial F_{\alpha\beta}} &= \frac{\partial}{\partial F_{\alpha\beta}}\left(\Phi(\{x_i^n\}) + V_0 P_{\alpha\beta} F_{\alpha\beta} - N k_B T \ln(V_0 \det \mathbf{F})\right) \\ &= \sum_{n=1}^{N} \sum_{i=1}^{3} \frac{\partial \Phi}{\partial x_i^n} \frac{\partial x_i^n}{\partial F_{\alpha\beta}} + V_0 P_{\alpha\beta} - N k_B T \frac{1}{\det \mathbf{F}} \frac{\partial \det \mathbf{F}}{\partial F_{\alpha\beta}} \\ &= \sum_{n=1}^{N} \frac{\partial \Phi}{\partial x_\alpha^n} L_\beta \tilde{x}_\beta^n + V_0 P_{\alpha\beta} - N k_B T \frac{C_{\alpha\beta}}{\det \mathbf{F}} (-1)^{\alpha+\beta} \end{aligned} \tag{2.4.25}$$

Equations (2.4.22) and (2.4.25) give the driving forces that enter in the Langevin dynamics given by equations (2.4.16) and (2.4.17).

2.4.4 Virial term and pressure computation

The coherency of the extended dynamics can be further demonstrated by showing how equations (2.4.16) and (2.4.17) leads to the same relation between external pressure acting on the system and the virial that can be derived from statistical mechanics [23].

We consider equation (2.4.17) and we multiply both sides by $F_{\alpha\beta}$ thus obtaining:

$$F_{\alpha\beta}\frac{\partial F_{\alpha\beta}}{\partial t} = \frac{1}{2}\frac{\partial F_{\alpha\beta}^2}{\partial t} = -\gamma\frac{\partial \overline{H}}{\partial F_{\alpha\beta}}F_{\alpha\beta} + A\zeta_{\alpha\beta}F_{\alpha\beta} \tag{2.4.26}$$

We then average equation (2.4.26) over its equilibrium probability distribution $\tilde{P}_{eq}(\{x_i^n, F_{\alpha\beta}\})$:

$$\frac{1}{2}\left\langle\frac{\partial F_{\alpha\beta}^2}{\partial t}\right\rangle_{\tilde{P}_{eq}} = -\gamma\left\langle\frac{\partial \overline{H}}{\partial F_{\alpha\beta}}F_{\alpha\beta}\right\rangle_{\tilde{P}_{eq}} + A\left\langle\zeta_{\alpha\beta}F_{\alpha\beta}\right\rangle_{\tilde{P}_{eq}} \tag{2.4.27}$$

The left side of (2.4.27) is zero because averages at equilibrium are obviously no time dependent. Moreover, using Itô calculus (see for example [21]) we have $\langle\zeta_{\alpha\beta}F_{\alpha\beta}\rangle_{\tilde{P}_{eq}} = 0$ so that we obtain, using equation (2.4.25):

$$\left\langle\frac{\partial \overline{H}}{\partial F_{\alpha\beta}}F_{\alpha\beta}\right\rangle_{\tilde{P}_{eq}} = \left\langle\sum_{n=1}^{N}\frac{\partial\Phi}{\partial x_\alpha^n}F_{\alpha\beta}L_\beta\tilde{x}_\beta^n + V_0F_{\alpha\beta}P_{\alpha\beta} - Nk_BT\frac{C_{\alpha\beta}F_{\alpha\beta}}{\det\mathbf{F}}(-1)^{\alpha+\beta}\right\rangle_{\tilde{P}_{eq}} = 0 \tag{2.4.28}$$

with $\alpha = 1,2,3$ and $\beta = 1,2,3$. Remembering the equalities (2.4.2) and (2.4.24), we sum over the column index β and we obtain:

$$\left\langle\sum_{n=1}^{N}\frac{\partial\Phi}{\partial x_\alpha^n}x_\alpha^n + V_0\sum_{j=1}^{3}F_{\alpha j}P_{\alpha j}\right\rangle_{\tilde{P}_{eq}} - Nk_BT = 0 \tag{2.4.29}$$

We now sum over α and finally obtain:

$$\frac{1}{3}V_0\sum_{i,j=1}^{3}\left\langle P_{ij}F_{ij}\right\rangle_{\tilde{P}_{eq}} = Nk_BT - \frac{1}{3}\sum_{i=1}^{3}\left\langle\sum_{n=1}^{N}\frac{\partial\Phi}{\partial x_i^n}x_i^n\right\rangle_{\tilde{P}_{eq}} \tag{2.4.30}$$

Equation (2.4.30) relates the virial, the second term on the left-hand side of equation (2.4.30), to the pressure acting on the system.

For the sake of completeness, we consider the simple case of an initially cubic box of volume V_0 submitted to an hydrostatic pressure p. Before to proceed, we must first remind the link between the Cauchy stress $\boldsymbol{\sigma}$ and the first Piola-Kirchhoff stress $\mathbf{P}$ used in our theory. The reason why we introduced above the

first Piola-Kirchhoff stress is that, in order to let the simulation box relax, we introduced the elements F_{ij} of the deformation gradient as new degrees of freedom. Therefore, a new potential term had to be added to the Hamiltonian and this term must be the product of the elements F_{ij} and their corresponding conjugate forces, which are precisely the elements of the first Piola-Kirchhoff stress. Now, when we consider a pressure p, we refer to a pressure that is applied to the *deformed* configuration, whereas the first Piola-Kirchhoff stress is a mesure of the forces acting on the elemental area of the *reference state*. Therefore, we need to use the relation between the Cauchy stress $\boldsymbol{\sigma}$, which is a measure of the forces acting on the deformed configuration, and the first Piola-Kirchhoff tensor $\mathbf{P}$. This relation is [24]:

$$J\sigma_{ij} = P_{ik}(F^T)_{kj} \tag{2.4.31}$$

where $\mathbf{F}^T$ is the transpose of the deformation gradient $\mathbf{F}$ and J is the determinant of $\mathbf{F}$. In the situation considered here, the tensors $\boldsymbol{\sigma}$, $\mathbf{P}$ and $\mathbf{F}$ are diagonal and isotropic:

$$\begin{aligned} \sigma_{ij} &= p\delta_{ij} \\ P_{ij} &= P_{11}\delta_{ij} \\ F_{ij} &= F_{11}\delta_{ij} \end{aligned} \tag{2.4.32}$$

Using equations (2.4.31) and (2.4.32), we immediately get that the left-hand side of equation (2.4.30) is equal to JpV_0. Hence, as the deformed volume V is simply given by $V = JV_0$, equation (2.4.30) becomes the well known equation of state for a fluid [25]:

$$pV = Nk_BT + \frac{1}{3}\left\langle \sum_{n=1}^{N} \mathbf{r}^n \cdot \mathbf{f}^n \right\rangle_{\tilde{P}_{eq}} \tag{2.4.33}$$

where $\mathbf{r}^n$ is the vector denoting the position of an atom n while $\mathbf{f}^n$ denotes the force acting on it. If now we imagine that all the N particles are indipendent, i.e. $\mathbf{f}^n = \mathbf{0}$, we obtain the equation of state of a perfect gas.

2.4.5 Virial stress components computation under periodic boundary conditions

Periodic boundary conditions (PBC) are a common way to avoid finite size effects. The concept is the following: the simulation is performed on a set of atoms contained within a finite simulation cell, where the positions of atoms outside the simulation cell are obtained by generating periodic images of the simulated atoms in accordance with the periodicity of the cell. As already highlighted in previous works concerned with pressure calculation in atomistic simulations [26, 27, 28], we

must be careful in calculating the variation of the potential energy Φ as a function of the deformation gradient components $F_{\alpha\beta}$ when PBC are applied. In this case, the potential energy of the unit cell will be function of the atom positions $\{x_i^n\}$ *and* of the box shape/size define by the three vectors $\mathbf{L}_\gamma$, which depend on the deformation gradient $\mathbf{F}$:

$$\Phi = \Phi(\{x_i^n\}, \mathbf{L}_\gamma) = \Phi(\{x_i^n, F_{\alpha\beta}\}) \tag{2.4.34}$$

Equation (2.4.34) highlights the fact that in this case Φ depends *explicitly* on the components $F_{\alpha\beta}$ and not just through the scaling of coordinates. Consequently, when periodic boundary conditions are applied, the variation of the unit cell potential energy with respect to $F_{\alpha\beta}$ will be:

$$\frac{\partial \Phi}{\partial F_{\alpha\beta}} = \sum_{n=1}^{N}\sum_{i=1}^{3} \frac{\partial \Phi}{\partial x_i^n}\frac{\partial x_i^n}{\partial F_{\alpha\beta}} + \sum_{\gamma=1}^{3}\sum_{i=1}^{3} \frac{\partial \Phi}{\partial (\mathbf{L}_\gamma)_i}\frac{\partial (\mathbf{L}_\gamma)}{\partial F_{\alpha\beta}} \tag{2.4.35}$$

In equation (2.4.35) two contributions are present: (i) the variation of Φ with respect to $F_{\alpha\beta}$ with atom position fixed i.e. bringing the atoms in one cell closer/farther to the atoms in another cell (ii) the variation of Φ due to the scaling of atoms positions. The problem is how to compute the additional contribution to the potential energy variation.

In the case of potential for which the energy of the system can be computed as a sum of pair interaction terms it is possible to bypass the problem by avoiding an explicit dependence of Φ on $F_{\alpha\beta}$. In order to do this, it is sufficient to write the potential energy per unit cell as a sum of pair contributions i.e. as a function of the relative distances between atoms:

$$\Phi = \Phi(\{\Delta x_i^{n,m\mathbf{k}}\}) = \sum_{\mathbf{k}\in Z^3}\sum_{n=1}^{N}\sum_{m>n}^{N} \phi(r^{n,m\mathbf{k}}) + \sum_{\mathbf{k}\in Z^3}\sum_{n=1}^{N} \phi(r^{n,n\mathbf{k}}) \tag{2.4.36}$$

$$\Delta x_i^{n,m\mathbf{k}} = (x_i^n - x_i^{m\mathbf{k}}), \quad , r^{n,m\mathbf{k}} = \sum_{i=1}^{3} (\Delta x_i^{n,m\mathbf{k}})^2, \quad x_i^{m\mathbf{k}} = x_i^m + G_{ij}k_j$$

where $r^{n,m}$ denotes the distance between the atoms n and m, G_{ij} is the matrix containing the periodic cell vectors $\mathbf{L}_\gamma$, $\mathbf{k} \in Z^3$ is a vector of three integers representing the offset in the three directions of the periodic images so that $x_i^{m\mathbf{n}}$ defines the position of one of the periodic images of atom m. The restriction $m > n$ avoid interactions to be computed twice. The second summation handles self-interactions between periodic images of the same atom (which typically are not relevant because of the presence of the cut-off). This implies that when periodic boundary conditions are used, the formula to be used for calculating the variation of Φ in function of $F_{\alpha\beta}$ is:

$$\frac{\partial \Phi}{\partial F_{\alpha\beta}} = \sum_{\mathbf{k}\in Z^3}\sum_{n=1}^{N}\sum_{m>n}^{N} \frac{\partial \Phi}{\partial r^{n,m\mathbf{k}}}\frac{\partial r^{n,m\mathbf{k}}}{\partial F_{\alpha\beta}} \tag{2.4.37}$$

The second derivative on the right-hand side of equation (2.4.37) is equal to:

$$\begin{aligned}\frac{\partial r^{n,m\mathbf{k}}}{\partial F_{\alpha\beta}} =& \sum_{i=1}^{3}\left(\frac{\partial r^{n,m\mathbf{k}}}{\partial x_i^n}\frac{\partial x_i^n}{\partial F_{\alpha\beta}} + \frac{\partial r^{n,m\mathbf{k}}}{\partial x_i^{m\mathbf{k}}}\frac{\partial x_i^{m\mathbf{k}}}{\partial F_{\alpha\beta}}\right) \\ =& \frac{\partial r^{n,m\mathbf{k}}}{\partial x_\alpha^n}\tilde{x}_\beta^n F_{\alpha\beta} + \frac{\partial r^{n,m\mathbf{k}}}{\partial x_\alpha^{m\mathbf{k}}}\tilde{x}_\beta^{m\mathbf{k}} F_{\alpha\beta} \\ =& \frac{\Delta x_\alpha^{n,m\mathbf{k}}}{r^{n,m\mathbf{k}}}\tilde{x}_\beta^n F_{\alpha\beta} - \frac{\Delta x_\alpha^{n,m\mathbf{k}}}{r^{n,m\mathbf{k}}}\tilde{x}_\beta^n F_{\alpha\beta}\end{aligned} \tag{2.4.38}$$

Combining equations (2.4.37) and (2.4.38) we obtain:

$$\begin{aligned}\frac{\partial \Phi}{\partial F_{\alpha\beta}} &= \sum_{\mathbf{k}\in Z^3}\sum_{n=1}^{N}\sum_{m>n}^{N}\frac{\partial \Phi}{\partial r^{n,m\mathbf{k}}}\frac{\Delta x_\alpha^{n,m\mathbf{k}}}{r^{n,m\mathbf{k}}}\Delta\tilde{x}_\beta^{n,m\mathbf{k}} F_{\alpha\beta} \\ &= \sum_{\mathbf{k}\in Z^3}\sum_{n=1}^{N}\sum_{m>n}^{N} f_\alpha^{n,m\mathbf{k}}\Delta\tilde{x}_\beta^{n,m\mathbf{k}} F_{\alpha\beta}\end{aligned} \tag{2.4.39}$$

where $f_\alpha^{n,m\mathbf{k}}$ is the component α of the force between atom n and a given periodic image of atom m.

In our code, we implemented a Lennard-Jones potential, which will be used in chapter 4 to analyse grain boundary migration, and a MEAM potential, that will be used in chapter 5 to analyse the $\beta \to \alpha$ phase transition in pure titanium. In both cases, the virial stress components can be calculated by the use of equation (2.4.39).

2.5 Heuristic justification of the overdamped Langevin dynamics

We have seen in the previous sections that, whether we consider the (NVT) or (N**P**T) ensemble, the overdamped Langevin dynamics converges to the correct thermodynamic equilibrium in the long-time limit. We propose now a heuristic argument to justify that, at a proper time scale, this overdamped dynamics reproduces also the *out-of-equilibrium* dynamics. For that purpose we analyse the auto-correlation functions of particles positions $\{x_i^n\}$ and velocities $\{v_i^n\}$. In order to do this, we examine the time-evolution of an atom trajectory in a defect-free single crystal by the use of Molecular Dynamics simulations. We simulated a 2D perfect crystal where atomic interactions are represented by a Lennard-Jones potential. The simulation box size was taken as 5000 x 5000 σ^2 with periodic boundary conditions in order to approach the ideal condition of an infinite media with reasonable computational costs. The initial positions were set on a perfect

triangular lattice and the initial velocities were randomly assigned using a temperature value of T =0.125 ϵ_{LJ}/k_B (for units definition see chapter 4, section 4.4.2). We integrated the trajectories via the Verlet scheme in the microcanonical ensemble (NVE). After thermal equilibrium was reached, we considered the trajectory (i.e. momentum and position) of a single atom in a time span $[0, T_{max}]$ and we calculated the following auto-correlation functions:

$$\langle v_i(t)v_i(t+\tau)\rangle = \frac{1}{T_{max}}\int_0^{T_{max}} \frac{(v_i(t)-\bar{v}_i)(v_i(t+\tau)-\bar{v}_i)}{\sigma^2_{v_i}}dt$$

$$\langle x_i(t)x_i(t+\tau)\rangle = \frac{1}{T_{max}}\int_0^{T_{max}} \frac{(x_i(t)-\bar{x}_i)(x_i(t+\tau)-\bar{x}_i)}{\sigma^2_{x_i}}dt$$

where $\bar{v}_i$ and $\bar{r}_i$ are time averages over T_{max} of velocity and position components while $\sigma^2_{v_i}$ and $\sigma^2_{x_i}$ are the variances (as we consider here a single particle, the upper index n has been omitted). The value of T_{max} was chosen in order to be at least 100 times the maximum value of τ for which the auto-correlation functions were calculated. The results of these calculations are reported in Fig.2.5.1, where we observe that the velocity auto-correlation function relaxes at a much smaller time scale than the position auto-correlation function. Calling τ_v the velocity auto-correlation time, we infer that, at any time scale Δt larger than τ_v, the velocities reach a quasi-static equilibrium state with respect to the positions. Therefore, at time scales $\Delta\tau > \tau_v$, we may consider that velocities relax and that, consequently, the phase space may be restricted to the set of positions $\{x_i^n\}$. This in turn implies that the dynamics should involve only the first order time derivative of x_i^n. Keeping in mind that this dynamics must converge to the correct equilibrium state, we conclude that, at time scales $\Delta\tau > \tau_v$, the kinetics of $\{x_i^n\}$ is given by overdamped Langevin dynamics such as the ones given in section 2.3 and 2.4, provided that the amplitudes of the noise terms fulfill the appropriate fluctuation-dissipation relation.

Of course, an exact formulation of the overdamped Langevin dynamics should proceed through an explicit coarse-graining procedure over the initial Newtonian dynamics. The outcome of this *time* coarse-graining would naturally lead to a coarse-grained potential $\Phi_{cg}(\{x_i^n\})$ that will differ from the original $\Phi(\{x_i^n\})$, as phonons will be adiabatically embedded into $\Phi_{cg}(\{x_i^n\})$. Moreover, explicit expressions for the mobility ν and noise amplitude B would arise. In the present work, we propose a simplification which consists in replacing the coarse-grained potential by the original one:

$$\Phi_{cg}(\{x_i^n\}) \approx \Phi(\{x_i^n\}) \tag{2.5.1}$$

Consequently, for the numerical applications reported in chapter 4 and 5 we have been working with the same potentials as the ones used in Molecular Dynamics

simulations.

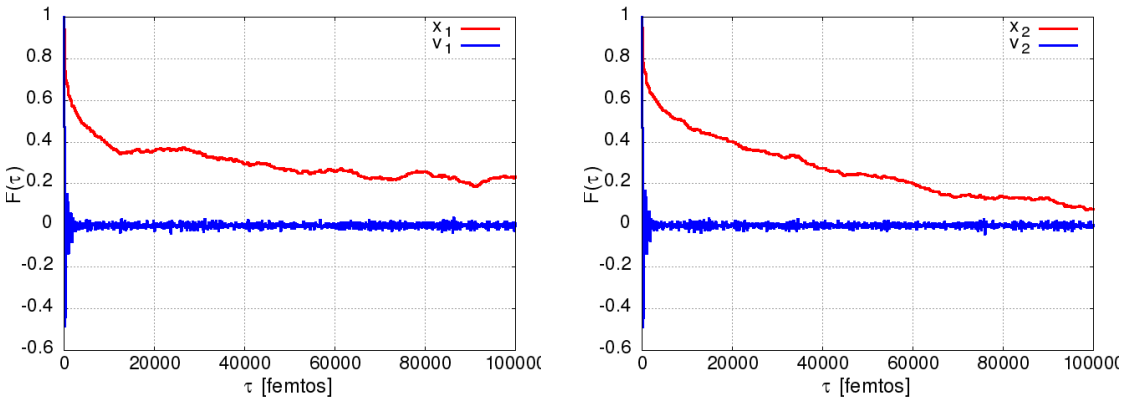

Figure 2.5.1: *The normalized auto-correlation functions for the first and second components of the velocity (blue curves) and position (red curves) of an atom in a defect-free 2D crystal calculated from Molecular Dynamics simulations. As we can see, the velocity components loose memory of their initial value much faster than the position components.*

Chapter 3

Numerical implementation

3.1 Introduction

In this chapter, we give the details of the numerical implementation of the model proposed. The chapter is divided into two parts. The first part deals with the numerical integration of stochastic differential equations (SDEs). The second one is dedicated to algorithms that we used in our home-made code to accelerate the search of pairs of atoms within the range of cut-off radius for force calculation.

3.2 Time integration of stochastic differential equations

In this section, we illustrate the numerical methods tested for the time integration of the system of SDEs used in our model. This field is still an active domain of research. The section is organized as follows. We begin with a review of some general concepts about time integration of SDEs, emphasizing the differences from ordinary differential equations (ODEs). We then describe the methods implemented in the present work for integrating the equations formalized in chapter 2 and report the results of the numerical tests performed that motivated the final decision of the algorithm used throughout this thesis.

3.2.1 Stochastic differential equations and stochastic integrals: general concepts

Without loss of generality, a stochastic differential equation is a differential equation containing a stochastic process. In its more general form, for the one-dimensional

case, it can be written as [29]:

$$\frac{dX}{dt} = G(X(t), \eta(t), t) \tag{3.2.1}$$

where G is a given function that depends, in general, on the variable *X(t)*, on the time t and on a stochastic process $\eta(t)$. The function G can have different forms as a result of the underlying physical mechanism which it describes, see for instance references [30, 31] as examples in microstructural evolution in alloys, plasticity, and magnetism. In the present work, we are interested in the numerical solution of SDEs of the form:

$$\frac{dX}{dt} = a(X(t)) + b(X(t))\eta(t) \tag{3.2.2}$$

where the function $a(X(t))$ corresponding to the deterministic part is referred as *drift* term, the function $b(X(t))$ is referred as *diffusion* term and $\eta(t)$ is a white Gaussian random noise such that $\langle \eta(t) \rangle = 0$ and $\langle \eta(t)\eta(t') \rangle = \delta(t - t')$. The noise term in Eq. 3.2.2 is called multiplicative or additive noise according to the dependence of the function b on the variable $X(t)$. The random term in the overdamped Langevin approach formulated in this thesis does not depend on the state variable $X(t)$ and hence we deal with an additive noise. However, in the following discussion, we consider the general case of multiplicative noise for the completeness. Equation 3.2.2 can be seen as an ordinary differential equation to which random fluctuations have been added. The "family" of solutions $X(t)$, one for each realization of $\eta(t)$, is also a stochastic process which inherits all the stochastic properties of the noise. In order to solve Eq. 3.2.2, we compute its integral in the time span $[t_1, t_2]$ with $t_1 < t_2$:

$$X(t_2) = X(t_1) + \int_{t_1}^{t_2} a(X(s))ds + \int_{t_1}^{t_2} b(X(s))\eta(s)ds \tag{3.2.3}$$

The first term on the right-hand side of equation (3.2.3) is a Riemann integral while the second is a stochastic integral. The evaluation of this integral is not obvious because the function $\eta(t)$ is continuous everywhere but non-differentiable. It can be thought as a sequence of delta peaks which cause jumps in the solution so that the values of $X(t)$ and $b(X(t))$ are undetermined at the time the delta functions arrives. To be more precise, we recast the stochastic integral above as

$$\int b(X(t))\eta(t)dt = \int b(X(t))dW, \tag{3.2.4}$$

where $dW = \eta(t)dt$ is the elementary increment of the Wiener process $W(t)$. This particular function is continuous but non-differentiable in any point. By definition of Riemann integral, we have:

$$\int b(X(t))dW = \lim_{n\to\infty} \sum_{l=1}^{n} b(X(\tau_l))[W(t_l) - W(t_l - 1)], \tag{3.2.5}$$

where we consider a discrete time interval $[t_l, t_l - 1]$ to which τ_l belongs. One can show that the above limit converges to a unique value for any choice of τ_l within the interval $[t_l, t_l - 1]$ if $W(t)$ is a smooth function. On the other hand, for a non-differentiable function $W(t)$, the limit depends on the location of τ_l in this interval. The decision on the place of τ_l leads to well known Itô– Stratonovich dilemma. In the *Itô interpretation* [32], the function $b(X(t))$ is evaluated at the beginning of an interval such that:

$$\int_{t_1}^{t_2} b(X(s))\eta(s)ds = b(X(t_1))[W(t_2) - W(t_1)] \tag{3.2.6}$$

In the *Stratonovich interpretation* [33], the function $b(X(t))$ is evaluated in the middle of the interval so that:

$$\int_{t_1}^{t_2} b(X(s))\eta(s)ds = b\left(\frac{X(t_2) + X(t_1)}{2}\right)[W(t_2) - W(t_1)] \tag{3.2.7}$$

The two interpretations above are particular cases of the general formula:

$$\int_{t_1}^{t_2} b(X(s))\eta(s)ds = b\left((1-\alpha)X(t_2) + \alpha X(t_1)\right)[W(t_2) - W(t_1)] \tag{3.2.8}$$

with any arbitrary α such that $0 \leq \alpha \leq 1$. Each particular choice of α generates a different stochastic evolution and, once the choice is fixed, the stochastic dynamics is unambiguously defined. Therefore, both the Itô and Stratonovich formulae are correct from a purely mathematical point of view although they follows different calculus rules. The choice depends on the underlying microscopic mechanism from which the stochastic equation is derived. In general, when the noise is due to external environmental effects, it can be argued that its intensity in the transition from the t_1 to t_2 time instant is independent from ΔW (Itô interpretation). On the other side, the Stratonovich interpretation seems more appropriate when the white noise is used as an idealization of a smooth real noise process i.e. of a colored noise process with small but in any case finite autocorrelation time [21]. The noise in overdamped Langevin equations is an *additive* noise i.e. its amplitude does not depend on the state of the system at time t. In this particular case, the Itô and Stratonovich calculi coincide.

3.2.2 SDEs numerical integration

In this section, we briefly outline the numerical methods that we used for the time integration of the SDEs in this work. We first begin with the introduction of some basic concepts on numerical convergence and stability.

3.2.3 Convergence and stability of numerical methods for SDEs

When working with stochastic differential equations it is important to distinguish between two different convergence criteria [34]:

1. in problems involving explicit simulations, the important point is the closeness of simulated trajectories to the real stochastic process. In this case we talk about *strong convergence*. A measure of the closeness of a sample path $X_{num}(t)$ to the real process $X(t)$ at the end of the time interval $[0, T]$ is given by the absolute error:

$$\epsilon(\Delta t) = E(|X_{num}(T) - X(T)|) \tag{3.2.9}$$

   where $E(\cdot)$ is the average over different trajectories and Δt is the step size adopted for the time integration. We say that an approximating process $X_{num}(t)$ converges in the strong sense with order γ if there exists a constant K and a positive constant Δt_0 such that:

$$\epsilon(\Delta t) = E(|X(T) - X_{num}(T)|) \leq K\Delta t^{\gamma} \quad \forall \Delta t \in (0, \Delta t_0) \tag{3.2.10}$$

2. in some applications, we are not interested in close path-wise approximation of $X(t)$ but in some function g of its value at time T or, more generally, in the expectation $E(g(X(T)))$. In this case, it suffices to have a good approximation of the probability distribution of the random variable $X(t)$ and we talk about *weak convergence*. An approximating process $X_{num}(t)$ is said to converge in the weak sense with order γ if there exists a constant K and a positive constant Δt_0 such that:

$$\bar{\epsilon}(\Delta t) = |E(g(X(T))) - E(g(X_{num}(T)))| \leq K\Delta t^{\gamma} \quad \forall \Delta t \in (0, \Delta t_0) \tag{3.2.11}$$

   where $g(X)$ is a given functional of the stochastic process $X(t)$ e.g. the mean value or the standard deviation of the process.

Convergence gives us a measure of the rate at which we can improve the accuracy of the numerical solution $X_{num}(t)$ by lowering the step size Δt. Another important property of a numerical method is its *stability domain* i.e. the maximum Δt for which an initial error remains bounded without growing in uncontrolled fashion during integration. This concept is really important for stiff system i.e. set of equations characterized by the presence of really different time scales where small time scales imply strong limitations on the maximum Δt for time integration.

3.2.4 Schemes for SDEs time integration

In the present work three different numerical schemes were tested: an explicit scheme, a predictor-corrector and an implicit scheme.

The explicit Euler scheme

One of the simplest time-discrete approximations of (3.2.2) is the explicit Euler approximation. We consider the stochastic process $X = \{X(t), 0 \leq t \leq T\}$ in the time interval $[0, T]$ and rewrite equation (3.2.2) in the following differential form:

$$dX = a(X)dt + bdW(t) \tag{3.2.12}$$

For a given discretization $0 < \tau_1 < \ldots < \tau_n = T$ of the time interval, the explicit Euler approximation is given by the following iterative scheme:

$$X_{num}(t + \Delta t) = X_{num}(t) + a(X_{num}(t))\Delta t + b\Delta W \tag{3.2.13}$$

where $\Delta t = (\tau_{n+1} - \tau_n)$ is the step-size and $\Delta W = W_{n+1} - W_n$ is the increment of the Wiener process i.e. an independent random variable with distribution $N(0, \Delta t)$. In practice, ΔW can be calculated as $\Delta W = \xi(t)\sqrt{\Delta t}$ where $\xi(t)$ is an independent random variable with distribution $N(0, 1)$. We can easily see that if $b = 0$ this scheme reduces to the classical explicit Euler for ordinary differential equations. In the present case, we deal with a multi-dimensional stochastic process such that $\mathbf{X}(t) \equiv x_i^n(t)$, where $i = 1, 2, 3$ and $n = 1, ..., N$ with N the total number of particles. The time approximation for the single component x_i^n is given by (we omit the pedex *num* for sake of clearness):

$$x_i^n(t + \Delta t) = x_i^n(t) + a(\{x_i^n(t)\})\Delta t + b\Delta W_i^n \tag{3.2.14}$$

The explicit Euler scheme has the advantages of an easy implementation, a low computational cost and a "simple" interpretation. On the other side, its stability domain is usually really limited. Its convergence is of order 1/2 in the strong sense, so lower than the convergence of order 1 obtained for the corresponding deterministic scheme. This is due to the fact that the increments of the Wiener process ΔW are of order $\Delta t^{1/2}$. In the weak sense, we can show that the scheme converges with order 1 [34].

The Heun's method

As mentioned before, implicit schemes have the advantage of a higher numerical stability when compared to the explicit ones but one needs to solve a non-linear set of equations. This can be quite tough and computationally expensive when

working with a high number of DOF as it is the case for atomistic simulations. Predictor-corrector schemes can represent a good compromise between numerical stability and computational efficiency. In our work, we used the well-known Heun's method, also known as modified Euler's method, which is given by:

$$\begin{aligned} \overline{x}_i^n &= x_i^n(t) + a(\{x_i^n(t)\})\Delta t + b\Delta W_i^n \\ x_i^n(t+\Delta t) &= x_i^n(t) + \frac{1}{2}\left(a(\{x_i^n(t)\}) + a(\{\overline{x}_i^n\})\right)\Delta t + b\Delta W_i^n \end{aligned} \tag{3.2.15}$$

Theoretically, the method has the same order of convergence as the explicit Euler scheme, 0.5 in the strong and 1 in the weak senses. However, as reported in [34], it could happen that in some particular cases the order of convergence is higher. From the stability point of view, the fact of using the prediction $\overline{x}_i^n$ for the evaluation of the drift term could lead to a higher numerical stability. From a computational point of view, the method is more expensive than the explicit Euler method because we evaluate forces twice at each time step. On the other hand, as we will show later, the error significantly decreases. It is worth to mention that this procedure can be considered as a two-stage second-order Runge–Kutta method and therefore one can envision to use four or higher stage Runge–Kutta methods. However, in our numerical tests, we found that the computational cost of fourth stage Runge–Kutta method, due to the requirement of calculating forces four times in each iteration, was higher than the largest possible increase in time-step size that we can implement. Therefore, we did not use higher order Runge-Kutta schemes in our simulations.

The implicit Euler scheme

Implicit integration schemes have the advantage of a higher numerical stability compared to explicit integration schemes. The simpler one is the implicit Euler scheme which can be seen as a generalization of the backward Euler scheme used for classical ODEs. For a given time discretization, the implicit Euler approximation is given by the following iterative scheme (we report directly the equations for the multi-dimensional case):

$$x_i^n(t+\Delta t) = x_i^n(t) + a(\{x_i^n(t+\Delta t)\})\Delta t + b\Delta W_i^n \tag{3.2.16}$$

with the same meaning of symbols used before. This scheme has the same order of convergence of the explicit one previously illustrated but the evaluation at time $(t+\Delta t)$ of the drift term strongly increases the stability domain so that bigger time steps can be used. On the other side, we need a good solver for the non-linear set of equations (3.2.16). For this purpose, we used the L-BFGS conjugate gradient method where the solution for the first iteration was obtained by the explicit

Euler scheme. While we observed that this method may drastically increase the time-step size, the number of iterations within the conjugate gradient step can also increase and this, in turn, implies several calculations of forces in each time step. Consequently, our implementation of the implicit Euler method was not very effective to perform large scale simulations from computational point of view.

3.2.5 Numerical tests

In this section, we report the results of the tests performed in order to check the convergence and stability of the integration schemes previously illustrated. The test performed consisted in the equilibration of a 2D defect-free crystal on a time span $[0, T]$ at given temperature. We used a Lennard-Jones potential Φ to describe atomic interactions with coefficients 8-4 and applied periodic boundary conditions in all directions. In the present work, we are not interested in path-wise closeness of the single atomic trajectories. We are rather interested in the overall evolution of the system. Consequently, we studied the convergence of the method in the weak sense taking as a functional of $\mathbf{X}(t) = \{x_i^n(t)\}$ the mean potential energy of the system $\overline{\Phi}$:

$$g(\{x_i^n\}) = \overline{\Phi} = \frac{1}{N} \sum_{n=1}^{N} \Phi^n(\{x_i^n\}) \tag{3.2.17}$$

We then analyse the step size dependence of the error:

$$\bar{\epsilon}(\Delta t) = |E(\overline{\Phi}(\mathbf{X}_{num}(T))) - E(\overline{\Phi}(\mathbf{X}_{exact}(T)))| \tag{3.2.18}$$

Since we do not know the analytical solution of our equations, we approximately assumed $\mathbf{X}_{exact}$ equal to the numerical solution obtained by taking an integrating time step $\Delta t = 5 \times 10^{-8}\ \epsilon_{LJ}^{-1}\nu^{-1}$ (for units, we refer the reader to chapter 4, section 4.4.2). As we will see later, this time step is really small if compared to the range of accuracy and stability characterizing the methods tested. To evaluate $\bar{\epsilon}(\Delta t)$, instead of taking an average of $\overline{\Phi}$ over several trajectories for each Δt considered, we took a time average over a single trajectory after the system has reached equilibrium. The substitution of an ensemble average with a temporal average is justified by ergodicity. We then performed 20 simulations for each Δt by changing the seed of the random noise in order to calculate a confidence interval for $\bar{\epsilon}(\Delta t)$. The results of our calculations for the different integration schemes adopted are reported in Tab. 3.1. The data are plotted in logarithmic scale in Fig. 3.2.1. We can see that for a time step $\Delta t < 5 \times 10^{-4}\ \epsilon_{LJ}^{-1}\nu^{-1}$ the round-off errors become more important than the error linked to time discretization. The explicit Euler and the Heun's method converge both linearly although for the same time step size the Heun's method has an higher level of accuracy. From the point of view of numerical stability, the maximum Δt achievable with the explicit Euler scheme is

$10^{-3}\ \epsilon_{LJ}^{-1}\nu^{-1}$ whereas, with the Heun's method, we can increase the time step size to $4 \times 10^{-3}\ \epsilon_{LJ}^{-1}\nu^{-1}$. For these two reasons, we choose to use the Heun's method to integrate our equations.

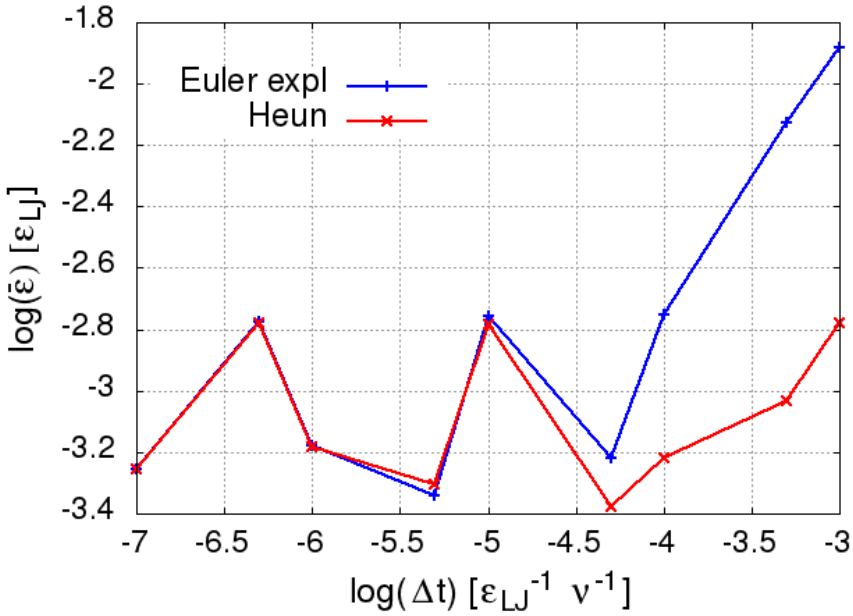

Figure 3.2.1: *The error $\bar{\epsilon}$ as a function of the step size Δt for the explicit Euler scheme and the Heun scheme (both axis are on logarithmic scale).*

	Euler explicit		Heun	
$\Delta t\ [\nu^{-1}\epsilon_{LJ}^{-1}]$	$\bar{\epsilon}\ [\epsilon_{LJ}]$	$\Delta\bar{\epsilon}\ [\epsilon_{LJ}]$	$\bar{\epsilon}\ [\epsilon_{LJ}]$	$\Delta\bar{\epsilon}\ [\epsilon_{LJ}]$
10^{-3}	1.308×10^{-3}	9.52×10^{-5}	1.67×10^{-3}	9.38×10^{-5}
5×10^{-4}	7.50×10^{-3}	2.03×10^{-4}	9.30×10^{-4}	2.04×10^{-4}
10^{-4}	1.77×10^{-3}	1.66×10^{-4}	6.07×10^{-4}	1.52×10^{-4}
5×10^{-5}	6.01×10^{-3}	1.63×10^{-4}	4.20×10^{-4}	9.74×10^{-5}
10^{-5}	1.76×10^{-3}	1.06×10^{-4}	1.64×10^{-3}	1.06×10^{-4}
5×10^{-6}	4.55×10^{-4}	9.36×10^{-5}	4.96×10^{-4}	1.00×10^{-4}
10^{-6}	6.66×10^{-4}	1.89×10^{-4}	6.60×10^{-4}	1.88×10^{-4}
5×10^{-7}	1.67×10^{-3}	1.36×10^{-4}	1.67×10^{-3}	1.36×10^{-4}
10^{-7}	5.58×10^{-4}	1.00×10^{-4}	5.57×10^{-4}	1.00×10^{-4}
5×10^{-8}	-	-	-	-

Table 3.1: *The error calculated from the numerical test performed with its confidence interval for the explicit Euler scheme and for the Heun scheme.*

3.3 Algorithms for forces computation

One of the most expensive operations in an atomistic model is forces computation. As an example, consider a system of N particles where interactions are described by a pair potential Φ. If we assume that interactions are inherently local, the force acting on a given atom n depends on the interatomic distances between n and all the N_n neighbouring atoms inside a certain cut-off radius r_{cut}:

$$f^n = \sum_{m=1}^{N_n} \frac{\partial \Phi}{\partial r}\bigg|_{r^{n,m}} \tag{3.3.1}$$

In order to find the N_n neighbours, a straightforward approach would be the direct evaluation of the inequality $r^{nm} \leq r_{cut}$ for each atom n composing the system. This search would require a double loop and so N^2 operations for each force evaluation, which is really computationally inefficient. Furthermore, between two time steps the positions of atoms usually do not change so much and consequently also their neighbours. There are two methods generally used to avoid useless computations of interatomic distances: the Verlet list and binning.

3.3.1 The Verlet list

The idea of the Verlet list method [35] is to store for each atom n a list of the atoms inside a radius r_{ver} defined in function of the cut-off radius and a skin distance ϵ:

$$r_{ver} = r_{cut} + \epsilon \tag{3.3.2}$$

At each iteration, to calculate the force on a given atom n, we need to check only the atoms contained in its list. Of course, atoms move during a simulation so that a suitable criterion must be stated in order to choose when the lists have to be updated. A possible approach is to verify if the two largest distances $d_{max,1}$ and $d_{max,2}$ travelled by the atoms are less than the skin distance. If:

$$d_{max,1} + d_{max,2} < \epsilon \tag{3.3.3}$$

it is not possible that any lists have changed. This approach assumes that the two most mobile atoms are near and have moved directly toward each other. In our code, we used the more restrictive criterion:

$$d_{max,1} < \frac{\epsilon}{2} \tag{3.3.4}$$

With the Verlet list, the force computations requires pN operations, where p is the number of neighbours contained in the list, and occasionally N^2 operations to rebuild the lists. The computational gain is difficult to estimate because it depends on the atom mobility (so, for example, on the temperature at which we are simulating the system) and on the skin distance ϵ.

3.3.2 Binning

Binning [36] consists in dividing the simulation box containing the atoms in cubic cells with side length $l_{cell} > r_{cut}$. When looking for the neighbours of a certain atom, only the atoms within its own bin or within one of the 26 neighbouring bins are checked. The computational cost is dominated by the assignment of each atom to a bin, which needs N calculations. When the simulation box is allowed to change shape, it is easier to make the cell assignment in the *scaled* reference configuration where atom positions are identified by the coordinates $\{\tilde{x}_i^n\}$. Consider a bin in the current configuration (Fig. 3.3.1) identified by the three non-orthogonal vectors $\{\mathbf{e}_1, \mathbf{e}_2, \mathbf{e}_3\}$ with norm:

$$\| \mathbf{e}_i \| = \frac{L_i^0 \sum_{j=1}^{3} (F_{ji})^2}{n_{cell,i}} \tag{3.3.5}$$

where L_i^0 is the box length in the reference configuration and n_{cell_i} is the number of subdivisions along the i direction. To define $n_{cell,i}$, we will impose that the height of this prism in this direction must be equal to l_{cell}. This is equal to the norm of the vector $\boldsymbol{\alpha}_i = \mathbf{e}_k \wedge \mathbf{e}_j / (|\mathbf{e}_k||\mathbf{e}_j|)$ which can be written as:

$$\| \boldsymbol{\alpha}_i \| = \frac{L_i^0 \sum_{j=1}^{3} (F_{ji}^{-T})^2)}{n_{cell,i}} \tag{3.3.6}$$

The number of cells in the direction i would be the highest integer approximating the value:

$$n_{cell_i} = \frac{L_i^0}{l_{cell}\sqrt{\sum_{j=1}^{3}(F_{ji}^{-T})^2}} \tag{3.3.7}$$

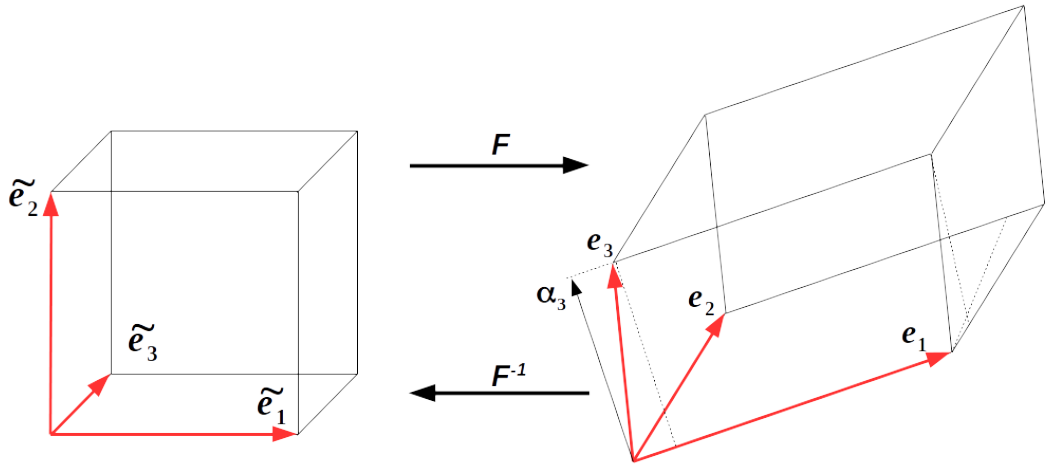

Figure 3.3.1: *An undeformed bin in the reference configuration (identified by the vectors* $\{\tilde{\mathbf{e}}_1, \tilde{\mathbf{e}}_2, \tilde{\mathbf{e}}_3\}$*) mapped by the deformation gradient* $\boldsymbol{F}$ *in the deformed one identified by the three vectors* $\{\mathbf{e}_1, \mathbf{e}_2, \mathbf{e}_3\}$.

3.3.3 Combining the binning algorithm and the Verlet list

In our code, we combine binning with the Verlet list in order to further speed up the forces computation. The forces are computed by using the neighbour lists which allows to check a lower number of neighbours. When necessary, we use the binning method with cell length $l_{cell} = 1.01 r_{ver}$ in order to rebuild the neighbour lists thus lowering of a factor N the computational cost of this operation. Furthermore, for both the potentials used in our simulations the total force $\mathbf{f}^n$ acting on atom n can be expressed as a sum of interactions between pairs $\mathbf{f}^{n,m}$. Considering that $\mathbf{f}^{n,m} = -\mathbf{f}^{m,n}$ we need to compute the forces for each pair just one time.

Consequently, we need to consider half of the surrounding bins of each atom to form its list. This is done by storing atom m in atom n list, but not atom n in atom m list, thus further reducing the number of computations. Finally, we recall that the open-source code LAMMPS that we used to perform MD simulations uses the combination of the binning algorithm with the Verlet list as well. We checked that the performance of our implementation is comparable to the one implemented in LAMMPS.

Chapter 4

1st application: coupling effect during grain boundary migration

4.1 Introduction

In this chapter we report the results of the first application of the model formalized in chapter 2, for which we decided to focus on the study of grain boundary migration. The reasons for this choice are multiple. First of all, details of grain boundary migration are of prominent interest to understand grain growth and grain nucleation i.e. the kinetics of recrystallization. Secondly, the multiplicity of microscopic processes involved in this phenomenon (dislocations glide and climb, interaction between dislocations, atomic jumps, ...) represents a challenging test for the model. The main objective of this part of our work has been the validation of the modelling approach proposed by comparison with Molecular Dynamics simulations. However, it has also been the occasion to highlight some peculiarities of GB migration.

The chapter is organized as follows. We firstly introduce some general concepts on grain boundaries, grain boundary migration and coupled motion. After that, we show the comparison between the results of our simulations and those obtained by Molecular Dynamics. Finally, we present a deeper analysis of different mechanisms of migration for low and high angle grain boundaries.

4.2 Grain boundaries and grain boundary motion

In the present section, we give a brief introduction to grain boundaries and their kinetics. For a more detailed treatment of the subject we address the reader to the specific literature cited.

4.2.1 What is a grain boundary?

We define a grain boundary (GB) as the interface separating two regions of different crystallographic orientation [37]. We can describe this entity in different ways, as a function of the level of detail adopted [38].

From a continous point of view, 5 parameters are needed to define the geometry of a plane grain boundary; an axis $\mathbf{l}$ and an angle θ defining the rotation between the two crystals (3 parameters) and the normal to the grain boundary plane $\mathbf{n}$ (2 parameters). On the basis of this first coarse-grained description, we distinguish between:

- *high angle* and *low angle* GB as a function of the misorientation angle θ;
- *symmetrical* and *asymmetrical* GB as a function of the position of the GB plane relatively to the two grains;
- *tilt* GB (the rotation axis lying on the GB plane) and *twist* GB (the rotation axis lying orthogonal to the GB plane). In a general framework, a GB can have a mixed character.

This macroscopic description is in fact rather poor. It provides a geometric reference of the orientation between the two lattices without incorporating any information about the *local* GB structure. Effectively, once the 5 macroscopic parameters have been fixed, at the atomic level different boundary structures can be obtained by relative translation of the two crystals along the normal to the boundary plane and along the plane itself.

From a discrete point of view, a GB can be described by using dislocation models. The basic idea of these models is that the misorientation between two contiguous grains can be accommodated by an array of dislocations. These dislocations are called *intrinsic*, since they are strictly necessary in terms of number and type to reproduce the boundary structure. The first dislocation model for symmetric tilt low angle grain boundaries was proposed by Bragg and Burgers in early 40's [39] and was further extended by Frank to general low misorientation GB [40]. The description *via* dislocation models is more refined than the previous one but still has some drawbacks. First, it is generally restricted to the case of low

angle grain boundaries. For high misorientation angles, the spacing between dislocations becomes small and single cores are no longer identifiable. Bilby proposed a generalization to the high-misorientation case [41] which relies on the definition of a *continous* dislocation distribution. Secondly, when a grain boundary has a complex geometry different dislocations arrangement are possible i.e. the Frank equation has multiple solutions. Energetic calculations are then needed in order to find the minimum energy structure.

Finally, a grain boundary structure can be described as an ensemble of structural units i.e. regular polyhedrons with atoms at the vertex. A boundary can be composed by a single structural unit or, in a more general case, by different units. Depending on the grain boundary, these structures can have a short range or a long range periodicity. This last description takes into account the local atomic arrangement to give a complete description of the GB structure and has general applicability. However, it is not easy to use for describing general grain boundaries and, as for the case of dislocation models, needs energetic calculations to choose the most probable structure among the multiple possibilities.

4.2.2 Basics on grain boundary motion and coupling effect

After defining what is a grain boundary and how it can be described at the macro and microscopic level, we give some notions about its kinetics. We also give some basics on the possibility of *coupled-motion* during grain boundary migration, which will be useful to analyse the results reported in section 4.4 and 4.6.

The motion of a GB can be *non-conservative* or *conservative* [1]. Non-conservative motion refers to a situation on which the interface migration is linked to long-range mass transport across it. Conservative motion refers to a situation on which there is only a local transfer of atoms across the interface from one crystal to the other. The velocity of the boundary is linked to its crystallographic structure, to the temperature and to the driving force. There are different types of driving forces. In general, a driving force occurs if a boundary displacement allows a decrease in the total free energy of the system. The most relevant sources of driving forces are the following [42]:

- an excess density of defects (e.g. dislocations) in one of the adjoining grains;
- the free energy excess associated to the interface itself;
- the anisotropy of any physical properties between the two grains e.g. elastic constants or magnetic susceptibility;
- the gradient of any intensive thermodynamic variable such as temperature, pressure, contents of impurity and so on.

When the motion of an interface requires thermal activation to overcome energy barriers, its migration may be viewed as a viscous process and, therefore, its migration rate v can be expressed as:

$$\mathbf{v} = M\mathbf{P} \tag{4.2.1}$$

where M is a mobility parameter and $\mathbf{P}$ is the driving force. $\mathbf{P}$ can be expressed in terms of the free energy change G for a displacement $\delta\boldsymbol{r}$ of the interface:

$$\mathbf{P} = -\frac{\delta G}{\delta \mathbf{r}} \tag{4.2.2}$$

The mobility M should reflect the thermally-activated aspect of the migration process and, therefore, an Arrhenius type law is usually adopted:

$$M = M_0 \exp\left(-\frac{E}{k_B T}\right) \tag{4.2.3}$$

where M_0 is a prefactor and E is the activation energy.

Describing a grain boundary as an interface, it can move tangentially or normally with reference to its plane. These two displacements components are usually coupled, although pure sliding is possible especially in high temperatures conditions or if a high mechanical stress is applied. Consider the low angle symmetric tilt GB in Fig. 4.2.1. In this simple case, the GB can be described by an array of dislocations. If a stress is applied, dislocation glide will cause a normal motion of the GB and the resulting growth of crystal 1 in crystal 2. At the same time, the necessity of continuity of crystal planes impose that the specimen will be sheared with a tangential movement of the interface. *A priori*, coupled GB motion is possible for low angle as well as for high angle boundaries and strongly depends on the migration mechanism of the interface i.e. on its structure at the atomic level. This particular phenomenon potentially plays an important role in the evolution of a microstructure. For example, coupled motion of non-flat grain boundaries has been pointed as responsible for grain rotation during grain growth or grain shrinking [43, 44] and during plastic deformation of nanocrystalline materials [45, 46, 47]. Various theoretical models have been proposed in order to understand and predict the occurrence of coupling during GB migration [48, 49, 50]. The possibility of grain rotation induced by GB migration is further investigated in the following sections.

4.3 Post-processing tools

Before showing the results of our numerical simulations, we describe in this section the post-processing tools used for the analysis.

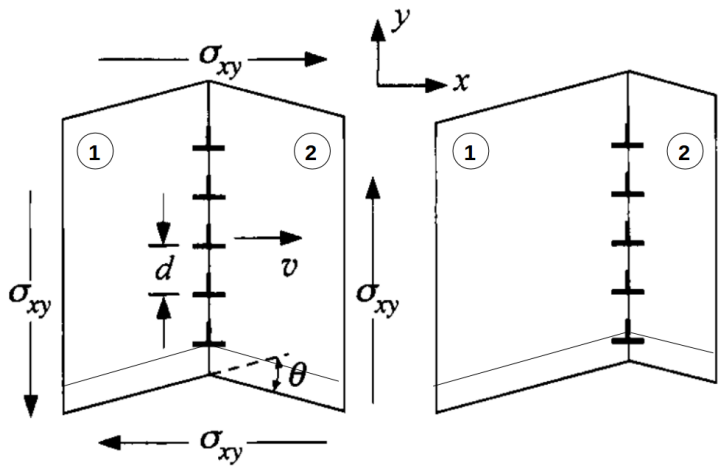

Figure 4.2.1: *A schematic representation of coupled motion explained via dislocation model. Dislocation glide has two effects: i) the growth of crystal 1 in crystal 2 with normal displacement of the interface ii) the shearing of the specimen with consequent tangential displacement of the interface. Figure adapted from [1].*

4.3.1 Grain boundary description and defects identification

We characterize the grain boundaries in terms of number and type of defects. In order to do this, we use the Delaunay triangulation to find the nearest neighbours of each atom. In a perfect 2-dimensional hexagonal grid, an atom has 6 nearest neighbours (NN). Along grain boundaries, we observe the formation of topological defects that consist in pairs of particles having 5 and 7 nearest neighbours respectively [51]. In the following sections, we will refer to this defect as a 5-7 pair.

4.3.2 Grain misorientation calculation

An important observable used to analyse our simulations is the misorientation between the grain and the matrix. In order to calculate the grain orientation at a given time step we operate as follows:

- we identify the crystalline defects by the use of the Delaunay triangulation;
- we "numerically" define the GB as the polygon connecting these defects (n.b.

this definition excludes the possible defects emitted from the grain boundary toward the matrix.);

- for each atom inside the grain, we calculate a local orientation parameter using the algorithm proposed in [52]. We compare the local positions $\Delta\mathbf{r}_{ij}$ of the six nearest neighbours of an atom i with the positions $\Delta\mathbf{r}_{ik}(\alpha)$ of the six nearest neighbours of an atom in a perfect 2D hexagonal grid rotated of an angle α. In order to do this, we define the parameter $\psi_i(\alpha)$:

$$\psi_i(\alpha) = \sum_{j=1}^{6}\sum_{k=1}^{6}\sum_{l=1}^{2}\exp\left(-\frac{[(\Delta\mathbf{r}_{ij})_l - (\Delta\mathbf{r}_{ik}(\alpha))_l]^2}{a_0^2}\right)$$

  where a_0 denotes the equilibrium lattice constant at the given temperature. The quantity $\psi_i(\alpha)$ is calculated for sixty equally spaced rotations between $0°$ and $60°$. The rotation delivering the maximum value of $\psi_i(\alpha)$ and thus corresponding to the best match between the actual and ideal lattice orientations is assigned to atom i as its orientation parameter;

- the grain orientation is defined as the average of the local orientations, excluding the atoms which forms topological defects.

4.3.3 Local deformation gradient calculation

To understand the microscopic mechanisms at the origin of the grain boundary migration in the high misorientation case, we will see below that we need to analyse the local atomic movements around a given atom. To do this, we use the following approach.

We consider the relative position $\Delta\mathbf{r}_{ij}(t^*)$ between the atom i and its first neighbour j at time $t = 0$ and at time t^* after the GB passage. Then, following the approach proposed in [53], we try to identify a local linear transformation $\mathbf{F}^i$ that describes the atomic movements around atom i. In order to do this, we minimize the mean-square difference between $\Delta\mathbf{r}_{ij}(t^*)$ and the local displacement that would result from the action of $\mathbf{F}^i$ on $\Delta\mathbf{r}_{ij}(0)$, $j = 1, \ldots, 6$:

$$D^{(i)^2} = \sum_{j=1}^{6}\|\Delta\mathbf{r}_{ij}(t^*) - \mathbf{F}^i\Delta\mathbf{r}_{ij}(0)\|^2 \tag{4.3.1}$$

Numerically, the matrix $\mathbf{F}^i$ which minimizes $D^{(i)^2}$ is given by:

$$\begin{aligned}(Y_i)_{km} &= \sum_{j=1}^{6}(\Delta\mathbf{r}_{ij}(0))_k(\Delta\mathbf{r}_{ij}(0))_m \quad , (X_i)_{lr} = \sum_{j=1}^{6}(\Delta\mathbf{r}_{ij}(t^*))_l(\Delta\mathbf{r}_{ij}(0))_r \\ (F_i)_{lm} &= (X_i)_{lr}(Y_i)^{-1}_{rm}\end{aligned} \tag{4.3.2}$$

If, for a given atom i, this minimization process leads to a small enough $D^{(i)^2}$ then we may interpret the dynamics around the atom i as a uniform transformation associated to the deformation gradient $\mathbf{F}^i$, i.e.:

$$\Delta\mathbf{r}_{ij}(t^*) \approx \mathbf{F}^i \Delta\mathbf{r}_{ij}(0) \tag{4.3.3}$$

Conversely, if the minimization does not lead to a small $D^{(i)^2}$, atomic movements around atoms i cannot be described by an affine transformation.

4.4 Validation of the modelling approach proposed

As previously highlighted, the main focus of this first application has been the validation of the modelling approach proposed. Consequently, we limited our study to the "simple" case where curvature is the only driving force for GB motion. Furthermore, we performed 2D simulation thus limiting our study to the case of pure tilt grain boundaries. In the following section we describe the particular case study considered, the details of the simulation setup and finally show the comparison between our results and those obtained by Molecular Dynamics simulations.

4.4.1 Case study

A simple example of GB motion driven only by curvature is the shrinking of a circular island grain embedded in a monocrystalline matrix when there is no strain energy difference between the two. This is a phenomenon well known in literature which has already been study numerically [54, 55, 56, 57, 58, 59, 52, 60] and experimentally [61, 62, 63]. All the numerical observations agree on the possible presence of coupling during GB motion with rotation of the island grain as a consequence of the interface curvature. On the other side, no grain rotation has been seen during experiments. The discrepancy between experiments and simulations may find an explication in a recent study [54] on mixed tilt-twist GB and so in the possible non-ideal tilt character of the island grains in experiments. It must be also underlined that the observation of coupled GB migration is not easy to realize during *in situ* experiments since there is the need to measure simultaneously the GB displacements in three directions as well as the change in orientation. A discussion on the differences between the experimental evidence and numerical modelling of curvature GB migration is beyond the scope of the present work but we wanted to at least mention this point.

4.4.2 Simulation setup

In our simulations, we consider the shrinkage of an initially circular 2D grain embedded in a monocrystalline matrix. Atomic interactions are described by a Lennard-Jones type potential:

$$\Phi = \epsilon_{LJ}\left[\left(\frac{\sigma}{r_{ij}}\right)^n - \frac{n}{m}\left(\frac{\sigma}{r_{ij}}\right)^m\right]$$

where r_{ij} is the interatomic distance, σ is the unit length and ϵ_{LJ} the energy scale (see the appendix A). The values of the exponents are set equal to $n = 8$, $m = 4$. This particular pair-interaction potential is chosen for its simplicity and numerical efficiency. At equilibrium, the resulting crystalline grid has an hexagonal geometry. The cut-off distance for the forces calculation was set equal to 2.2 σ. We apply periodic boundary conditions in all directions and set the rectangular simulation box equal to $180 \times 180\ \sqrt{3}/2\sigma^2$. Simulations were performed in the (N**P**T) ensemble at zero pressure, in order to avoid stresses generated by the volume change during the shrinking of the grain. The temperature was set equal to 0.125 ϵ_{LJ}/k_B, which corresponds to approximately 1/3 of the melting temperature. This temperature was previously calculated by performing several simulations of a perfect monocrystal at different temperature and following the evolution of the mean potential energy of the system. In the 3D case, a sharp increase of this variable takes place at the melting point. In our 2D geometry, a rapid variation of the potential energy was also clearly visible and used as a definition of the melting temperature (even though, strictly speaking, a real melting transition does not exist at finite temperature in a 2D system).

Special care was taken to create an initial GB structure as close to equilibrium as possible. For this purpose, the following procedure has been developed. Starting from a perfect lattice previously relaxed at the desired temperature, a circular central area is rotated. To avoid the occurrence, at the grain/matrix interface, of atoms that are too close to each other, the monocrystalline matrix is slightly expanded. Then, the system is shortly relaxed by integration in the isothermal-isobaric ensemble. The final result of this procedure is an initial relaxed GB configuration. In our simulations, we have always used a grain diameter smaller than half the smallest dimension of the simulation box to minimize the interactions with periodic images.

To perform LG dynamics simulations, we implemented the equations formalized in chapter 2 in a code that we developed (written in Fortran). To perform MD simulations we used the open-source code LAMMPS with a Nose-Hoover style thermostat and barostat [64, 65].

4.4.3 Comparison between LG and MD

In comparing the Langevin dynamics with MD, we consider three initial misorientations: $\theta_0 = 10°$, $45°$, $38.2°$. In Fig. 4.4.1, we present the evolution as a function of the grain size of (i) the misorientation angle θ (ii) the number of 5-7 defects at the boundary. The results obtained from the LG model are presented in red and the ones obtained from MD in blue. From the diagrams we observe that:

- the coupling effect is well capturated by the Langevin dynamics as well as by MD. Both methods highlight the presence of grain rotation during the boundary migration for $\theta = 10°$ and $\theta = 45°$ while for the value of $\theta = 38.2°$ no rotation is present;

- there is a good agreement between the Langevin and MD simulations in terms of increase rate of the misorientation angle and sense of rotation (left hand side of Fig. 4.4.1). Local mismatches between the curves are justified by the fact that the dynamics is, in both simulations method, stochastic (the Langevin dynamics is of course explicitly stochastic as it includes noise terms; MD equations are formally deterministic but, as we know, they generate chaotic dynamics -even in the microcanonical ensemble- whose trajectories are extremely sensible to initial conditions, which confers to the overall dynamics a stochastic character);

- the evolution of the number of 5-7 defects as a function of the grain size also demonstrates a very good agreement between the simulation results obtained by the two methods (right hand side of Fig. 4.4.1). This indicates that the atomic mechanisms at the origin of the GB migration are similar in both methods.

We can conclude from this comparison that the Langevin dynamics is able to catch the complex dynamics of coupled GB migration and that the results obtained by this new methodology strongly agrees with the ones obtained with more established methods such as Molecular Dynamics.

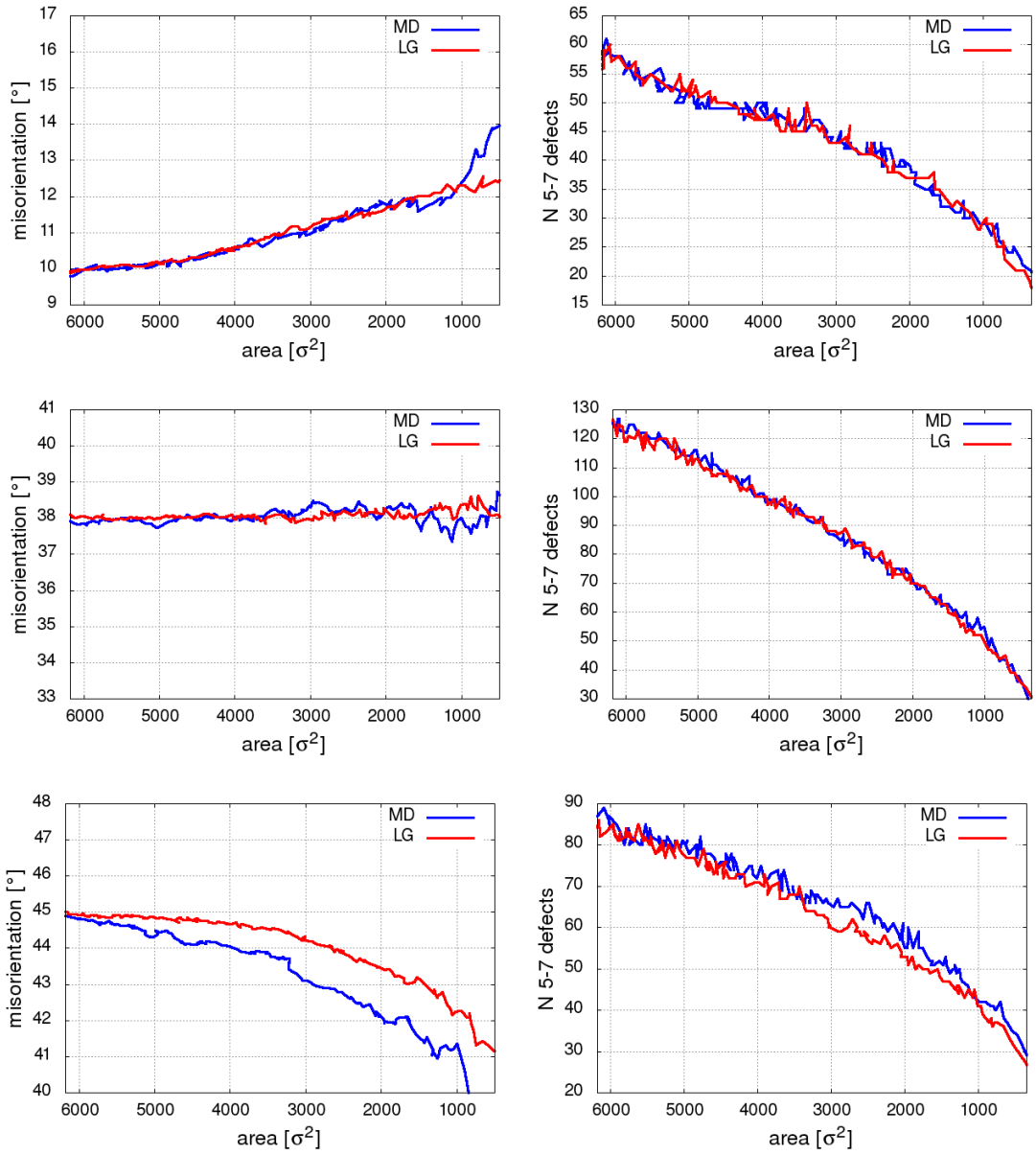

Figure 4.4.1: *Evolution of the misorientation angle θ and of the number of 5-7 defects along the grain boundary as a function of the grain area, for the initial values $\theta_0 = 10°$ (top row), $38.2°$ (middle row), $45°$ (bottom row). The results obtained with the LG model (in red) are compared with the ones obtained with MD simulations (in blue).*

4.5 Study of the GB migration mechanism

In this section we report our investigation on the GB migration mechanism for the low and high misorientation cases. For both cases, we first make some observations on the GB structure, which deeply influence the migration mechanism, and then we analyse its dynamics during shrinking.

4.5.1 Low misorientation case

The following observations are referred to the initial misorientation value $\theta_0 = 10°$. However, similar migration mechanisms act for other low misorientation angles so that the considerations here reported can be thought of general validity for all the range of angles between 0° and 10°.

Grain boundary structure The GB structure consists of several well spaced single 5-7 pairs (see Fig. 4.5.1). These defects can be interpreted as dislocation cores. Six different edge dislocations were observed in our simulations whose Burgers vectors are:

$$\pm[1,0,0]a_0, \pm 1/2[1,\sqrt{3},0]a_0, \pm 1/2[1,-\sqrt{3},0]a_0$$

where a_0 denotes the equilibrium lattice constant. At the simulation temperature $T = 0.125\ \epsilon_{LJ}/k_b$, a_0 is equal to 0.95σ. In the following notation, we will omit the constant a_0 for sake of clarity. The arrangement of these dislocations along the boundary changes accordingly to the orientation of the GB plane as shown in Fig. 4.5.3, where four different snapshots of the GB during shrinkage are reported. When the normal to the boundary plane is nearly parallel to one of the above listed Burgers vectors, the boundary mainly consist of only one dislocation type. Indeed, we frequently observe the formation of facets during the GB migration, as pointed out in previous works [58, 55]. These facets contain homogeneous dislocation arrays with Burgers vectors parallel to the facet normal. An example of faceting is also reported in Fig. 4.5.2.

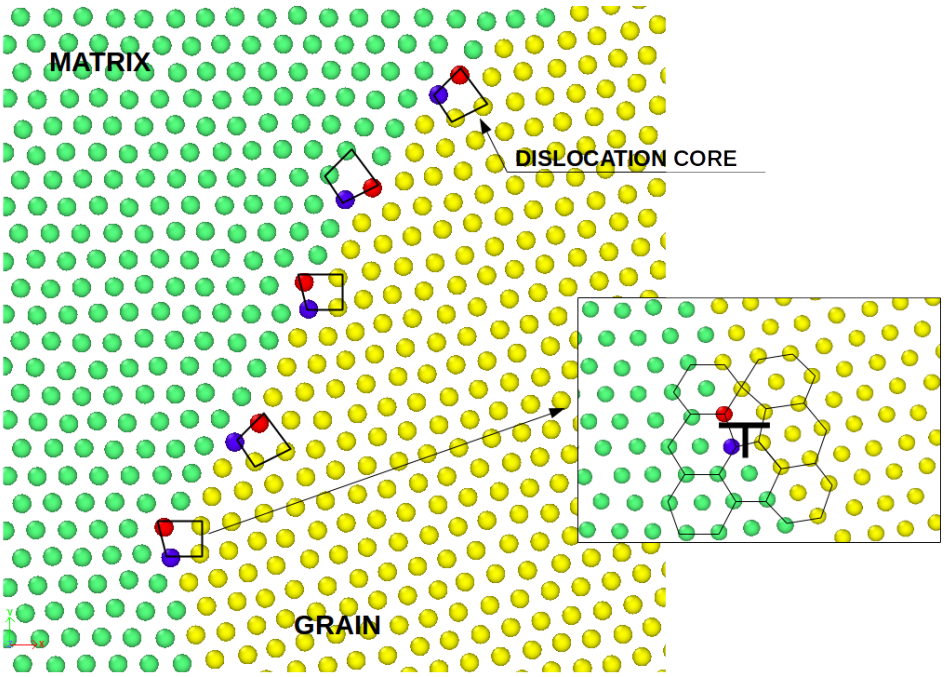

Figure 4.5.1: *The four-sided polyhedrons formed by the 5-7 pairs (red and blue atoms) intepreted as dislocation cores for the low misorientation grain boundary* $\theta = 10°$. *The matrix is represented in green and the circular grain in yellow.*

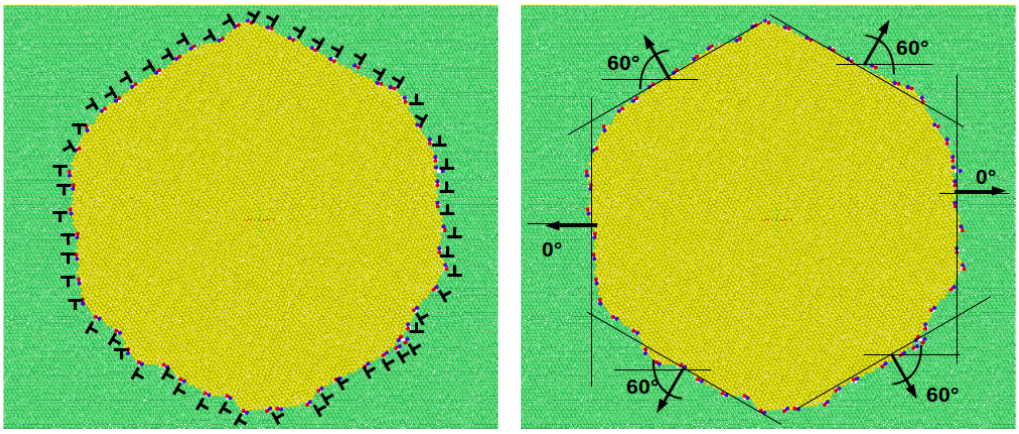

Figure 4.5.2: *In this snapshot, six facets are highlighted. The facets are mostly composed by a single dislocation set and their normal is oriented parallel to the corresponding Burgers vector.*

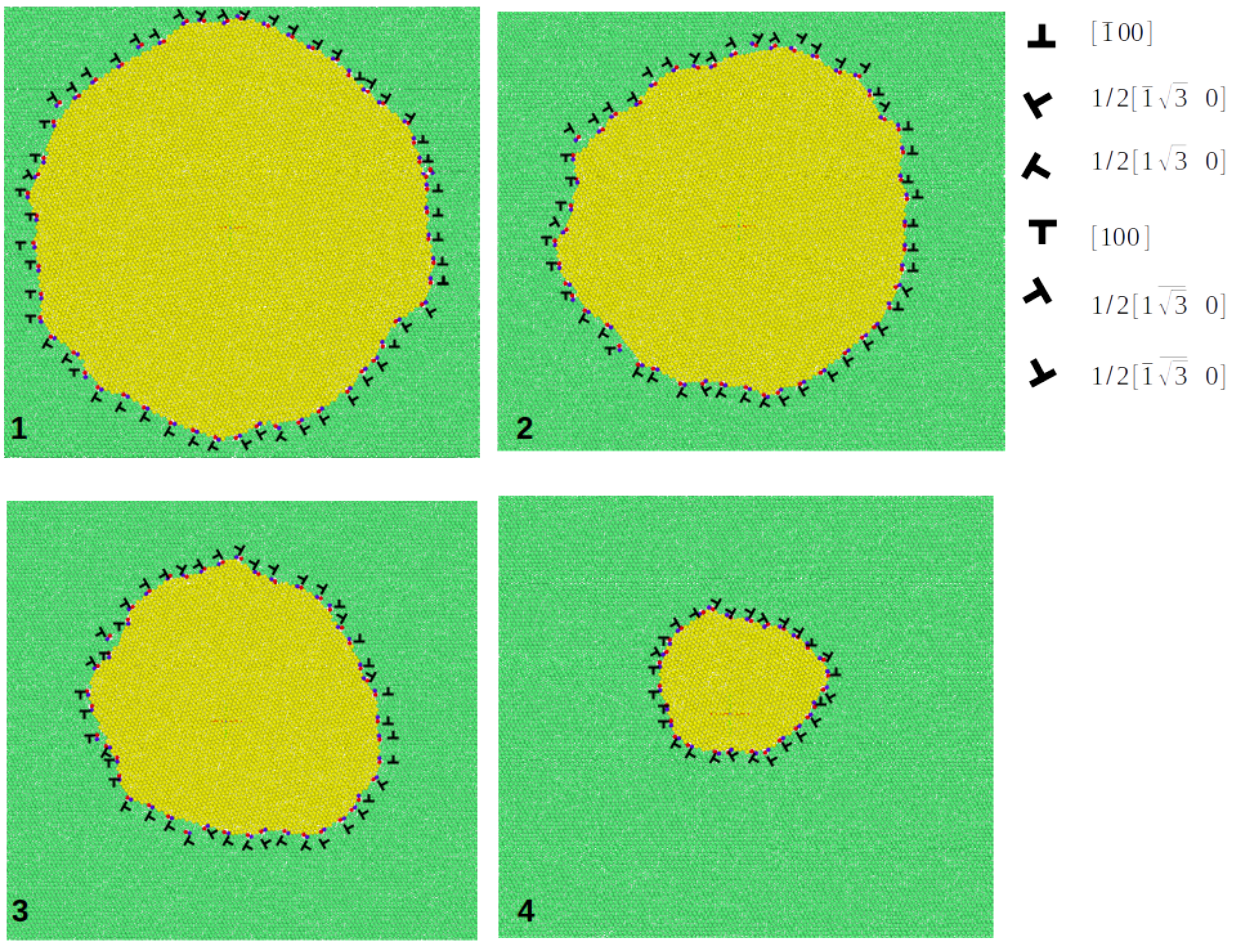

Figure 4.5.3: *Four snapshots of the grain while shrinking. Dislocations are highlighted by couples of atoms in red-blue colour. Six Burgers vectors were identified during simulations.*

Grain boundary migration The grain boundary migrates towards its centre of curvature until the grain totally disappears. No defects are left in the matrix after the grain shrinkage. During the GB migration, there is an increase in the misorientation θ and a corresponding increase in the dislocation density ρ_D at the boundary, which is defined as:

$$\rho_D = \frac{N_D}{p} \tag{4.5.1}$$

where N_D is the number of dislocation cores along the boundary and p is the boundary perimeter. We report the evolution of these two quantities as a function of the grain area (normalized by their initial values θ_0 and ρ_{D_0}) in Fig. 4.5.4. We can see that ρ_D increases by approximately 40% from its initial value. Its evolution strictly follows the change in the misorientation angle although it displays some local peaks, due probably to the approximated and arbitrary method used to estimate the perimeter of the grain (see section 4.3.2).

We go now more in detail on the microscopic processes driving the migration. In our simulations, we observed two different reactions between dislocations:

1. partial or total annihilation between two or more dislocations. An example of this reaction is shown in Fig. 4.5.5, where we observe the following reaction in terms of Burgers vectors and with obvious notations:

$$A : 1/2[1\sqrt{3}0] + B : [100] + C : 1/2[1\overline{\sqrt{3}}0] \rightarrow B : [100] + B : [100]$$

   Note that this three-to-two dislocation reaction may also be analysed as resulting from three smaller scale reactions, namely the splitting of the middle [100] Burgers vector into $1/2[1\sqrt{3}0]$ and $1/2[1\overline{\sqrt{3}}0]$ followed by the merging of these two Burgers vectors with dislocation A and C, respectively. However, as the overall process occurs at really small time and space scales, it is not possible to assert if this three step process does exist. Therefore, we simply refer to this process as an annihilation mechanism through which three initial dislocations react and generate only two dislocations;

2. the interaction between two dislocations. This mechanism is presented in Fig. 4.5.6. The glide of the dislocations labelled A and B in Fig. (4.5.6)-a, with Burgers vectors [100] and $1/2[1\overline{\sqrt{3}}0]$, necessarily brings the two dislocations close to each other. When the distance between the dislocations is of the order of two interatomic distances, a rapid movement of a few atoms inside the overlapping dislocation cores leads to an effective exchange of the Burgers vectors of the two dislocations. This mechanism, sketched in Fig. (4.5.6)-c, is better shown in Fig. 4.5.7(a-c) where the additional planes of the two dislocations are shown in dotted line. We look at the atoms forming the grey lozenge. When the two dislocation cores approach the surrounding lattice is highly distorted and the lozenge becomes a square. This configuration is unstable and quickly collapse thus causing a rotation of the two Burgers vectors. The displacement induced in the surroundings by this process are represented by arrows. The final result can be interpreted as a crossing of two dislocations supplemented by a displacement outside their

gliding planes, without the need of a vacancy assisted climb with a pre-existing surrounding atom vacancy. For this reason, we will refer to this first mechanism as *"effective climb"*. As above, we note that this process could also be analysed as a splitting of dislocation A into dislocations $1/2[1\overline{\sqrt{3}}0]$ and $1/2[1\sqrt{3}0]$ followed by a merging of the latter with dislocation B but again, as the overall process occurs at very small time and space scales, we simply refer to the overall mechanism as a climb process, because this is the process we observe when we compare the initial and final states.

In order to better understand what role dislocations play in the overall GB migration, we track the dislocations gliding planes by following the movement of the 5-7 pairs. In Fig. 4.5.8 we report four snapshots in which we coloured the gliding plane in dark green. The grain is highlighted in yellow colour and the matrix in light green. From these snapshots we can observe that the migration takes place *via* a combination of dislocation glide and reactions, as clearly appears from the numerous crossing points between dislocation gliding planes. Moreover, the planes sheared by dislocations draw a regular pattern of hexagonal cells. These cells decrease their size when approaching the grain centre. This observation is in agreement with the fact that the dislocation density increases during the grain shrinkage so their average distance along the boundary decreases (see top row in Fig. 4.4.1). In Fig. 4.5.9 we show a colour map of the magnitude of atomic displacements after the grain boundary passage. This map strictly follows the patterns of the dislocation gliding planes. Moreover, it suggests that the GB migration proceeds by the formation of several cellular "hexagonal shaped rings" which result from a combination of glide, effective climb (which allows the propagation of dislocations along the boundary) and annihilation. A *simplified* description of this phenomenon is given in the following.

We describe the grain boundary as an hexagon, as shown in Fig. 4.5.9-b. This of course is an idealization that oversimplifies the observed shape of the grain boundary. However, during the course of its shrinking, we do often observe that the initially circular grain displays well defined facets that all together form a shape that is not far from an hexagon. This is particularly clear in Fig. 4.5.9-a, where we display the residual atomic displacements map after a grain has disappeared. We indeed observe that, during grain shrinking, the grain boundary follows in average an hexagonal symmetry. Then, the migration of this grain boundary can be described as follows (see Fig. 4.5.10):

- the dislocations glide until an unstable situation is reached when the dislocations at the corners arrive close one to the other (Fig. 4.5.10-a);
- effective climb of the dislocations meeting at the six corners (see green circles

in Fig. 4.5.10-a and b);

- subsequent propagation of effective climb along the hexagon sides (see red circles in Fig. 4.5.10-b and c);

- after propagation, a first hexagonal shaped ring is closed by partial annihilation between two or more dislocations (see for example the blue circles in Fig. 4.5.10-c and d).

In brief, the grain collapse proceeds through a succession of dislocation glide perpendicularly to the hexagonal facets, propagation of climb events along the facets and one annihilation event per facet. The overall effect of this mechanism is an increase of the misorientation angle θ that follows the decrease of the grain area.

The link between the misorientation angle θ and grain area A may be identified as follows. As explained above, the process is analysed as the successive formation of hexagons. We label the hexagons by the index n. At stage n, we note l_n, R_n, θ_n, N_n^{side} and d_n the length of the facets, the distance of the facets from the centre of the hexagon, the misorientation angle, the number of dislocations along each facet and the average distance between dislocations, respectively. Using Frank formula, we have:

$$d_n = \frac{\| \mathbf{b} \|}{2\sin(\theta_n/2)} \sim \frac{\| \mathbf{b} \|}{\theta_n}$$

The facet length l_n and the distance R_n are geometrically linked (see Fig. 4.5.9-b):

$$l_n = \frac{2}{\sqrt{3}} R_n$$

and d_n is defined by:

$$d_n = \frac{l_n}{N_n^{side}}$$

Now, we analyse the transition from hexagon n to hexagon $(n+1)$ as follows:

- first, all the dislocations that sit along the facets glide perpendicularly to the facets and their number remains constant. Under the hypothesis that the distance between two neighbouring dislocations that are separated by a corner is equal to the average distance, a simple geometrical analysis shows that an unstable situation (i.e. two dislocations come close to each other) is reached after a gliding equal to d_n;

- then, effective climb events start at the corners, propagate along the boundary and stop when the new hexagon is closed through one annihilation event per side.

Obviously, this kinematics is associated to the following recursive relations:

$$
\begin{aligned}
R_{n+1} &= R_n - d_n \\
N_{n+1}^{side} &= N_n^{side} - 1 \\
d_{n+1} &= \frac{2}{\sqrt{3}} \frac{R_{n+1}}{N_{n+1}^{side}}
\end{aligned}
$$

It is straightforward to integrate step by step these relations and to calculate, for each index n, the actual value of the misorientation angle θ_n and hexagon area A_n:

$$
\begin{aligned}
\theta_n &= \sin^{-1}\left(\frac{\| \mathbf{b} \|}{2d_n}\right) \\
A_n &= 2\sqrt{3}R_n
\end{aligned}
$$

We used this kinematics to estimate the co-evolution of the misorientation θ and grain area A for a grain with initial misorientation $\theta_0 = 10°$ and area $A_0 = 2\sqrt{3}R_0$ with $R_0 = 44.74\ \sigma$. The result is shown in Fig. 4.5.11 where, for comparison, we also report the result obtained by the atomistic simulations (already shown in Fig. 4.5.4). First, we observe that the model reproduces the grain rotation. This means that a coupled normal-tangential motion of grain boundary is embedded into the local mechanisms at the root of our model (glide, effective climb, annihilation). Second, we observe that our approximate hexagonal kinematics reproduces qualitatively the atomistic simulation, even if a quantitative agreement is not obtained, which is not surprising, taking into account the simplicity of the geometrical model we have proposed.

That said, we think that the overall agreement between the simulation and the simple model confirms the validity of the local mechanisms (glide, effective climb and three-to-two annihilation processes) that we identified as been at the root of the grain shrinking mechanism for small initial misorientation. These mechanisms generate grain rotation (more precisely, an increase of the misorientation) in agreement with the atomistic simulations, thereby confirming the existence of a coupled motion.

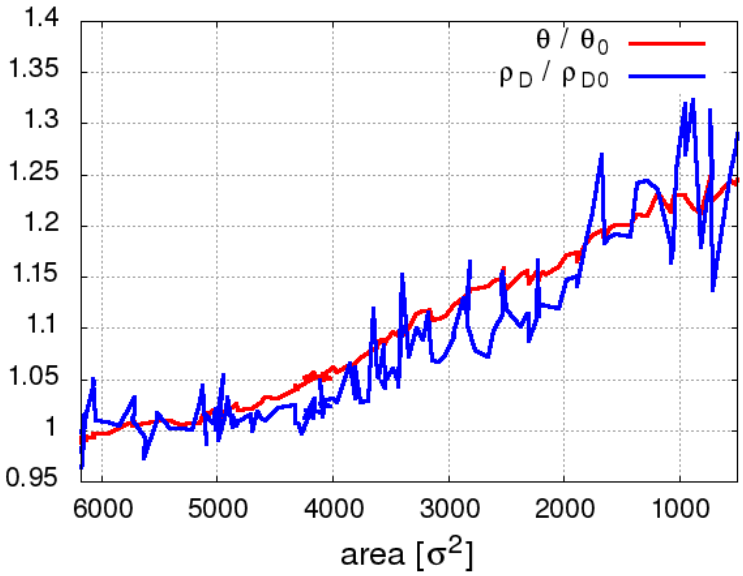

Figure 4.5.4: *Normalized dislocation density ρ_D/ρ_{D_0} along the grain boundary (blue curve) and change in the misorientation angle θ/θ_0 (red curve) during grain shrinkage for the initial misorientation $\theta_0 = 10°$.*

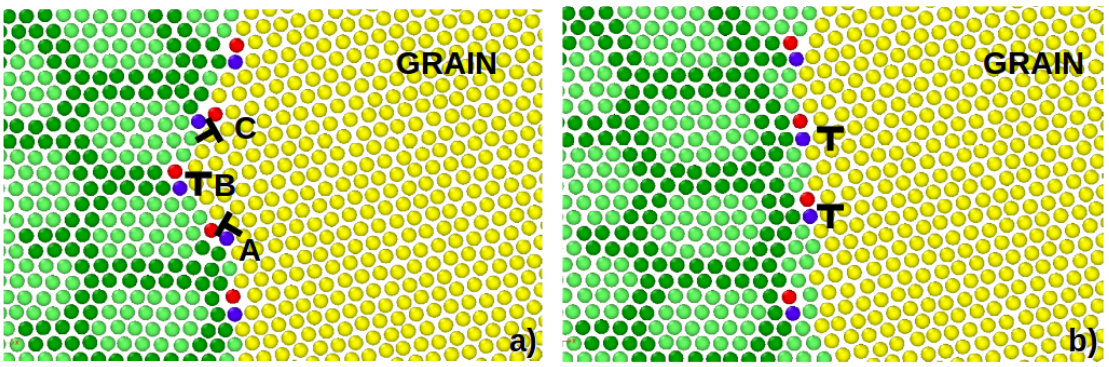

Figure 4.5.5: *Dislocation annihilation. In this figure dislocations are highlighted by a 5-7 couple in blue-red colour. The grain is shown in yellow, the matrix in light green. We coloured the planes along which the dislocations have glided in dark green in order to keep track of their paths. The three dislocations A, B, C with Burgers vectors* $1/2[1\sqrt{3}0]$, $[100]$, $1/2[1\overline{\sqrt{3}}0]$ *recombine to form two dislocations with Burgers vectors* $[100]$.

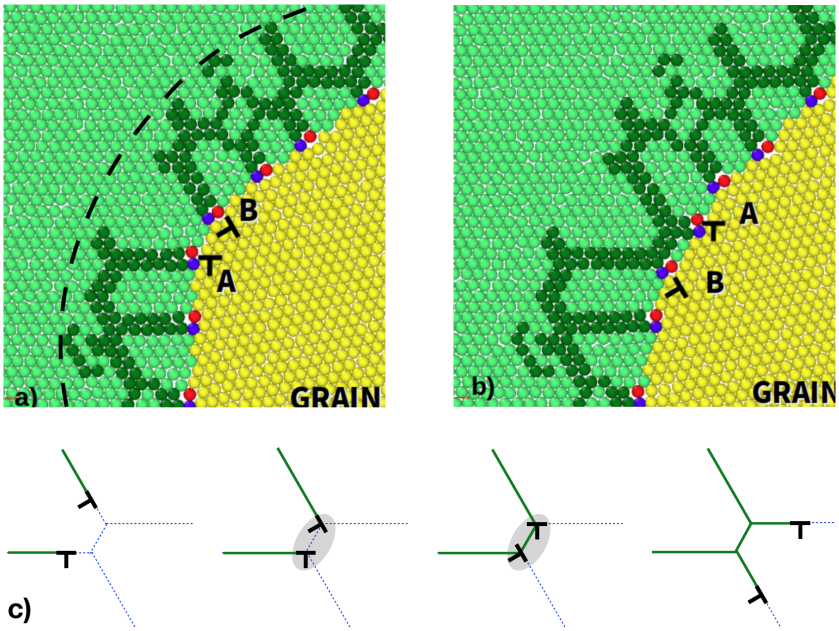

Figure 4.5.6: *Effective climb (see text). Direct interaction of two dislocations A and B with Burgers vectors* [100] *and* $1/2[1\sqrt{30}]$*; a) initial configuration; b) final configuration; c) sketch of the mechanism. The dashed line indicates the initial position of the grain boundary. The colour code is the same as the one used in Fig. 4.5.5.*

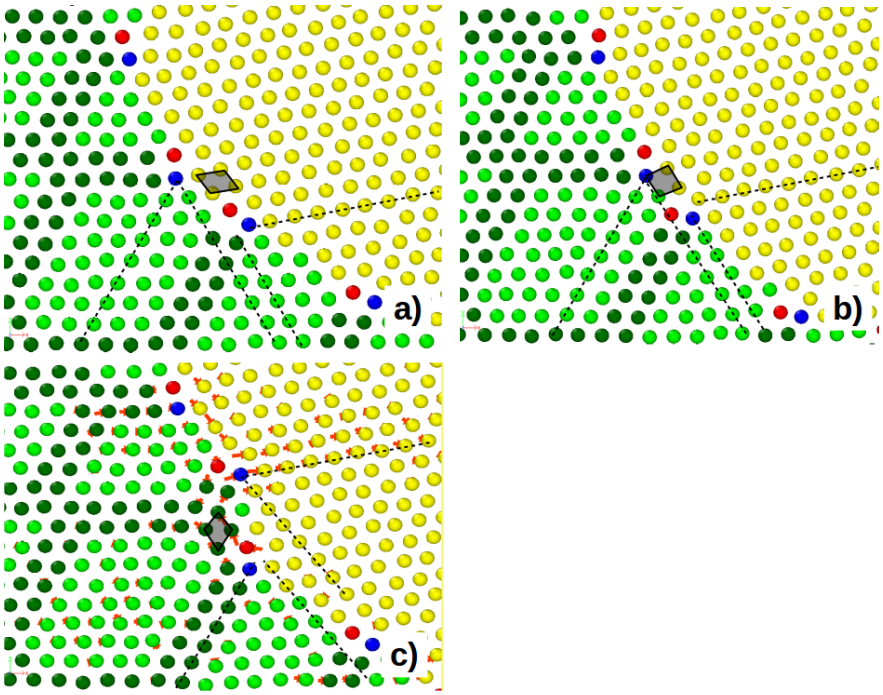

Figure 4.5.7: *Effective climb (see text). In this figure: a) two dislocations approach one to the other (center of the figure) b) they arrive at a distance comparable to two interatomic spacings thus inducing a strong distortion in the surrounding lattice c) a local slip of atoms induces a rotation of the original Burgers vector (atom displacements are represented by arrows). For the colour code see Fig. 4.5.5.*

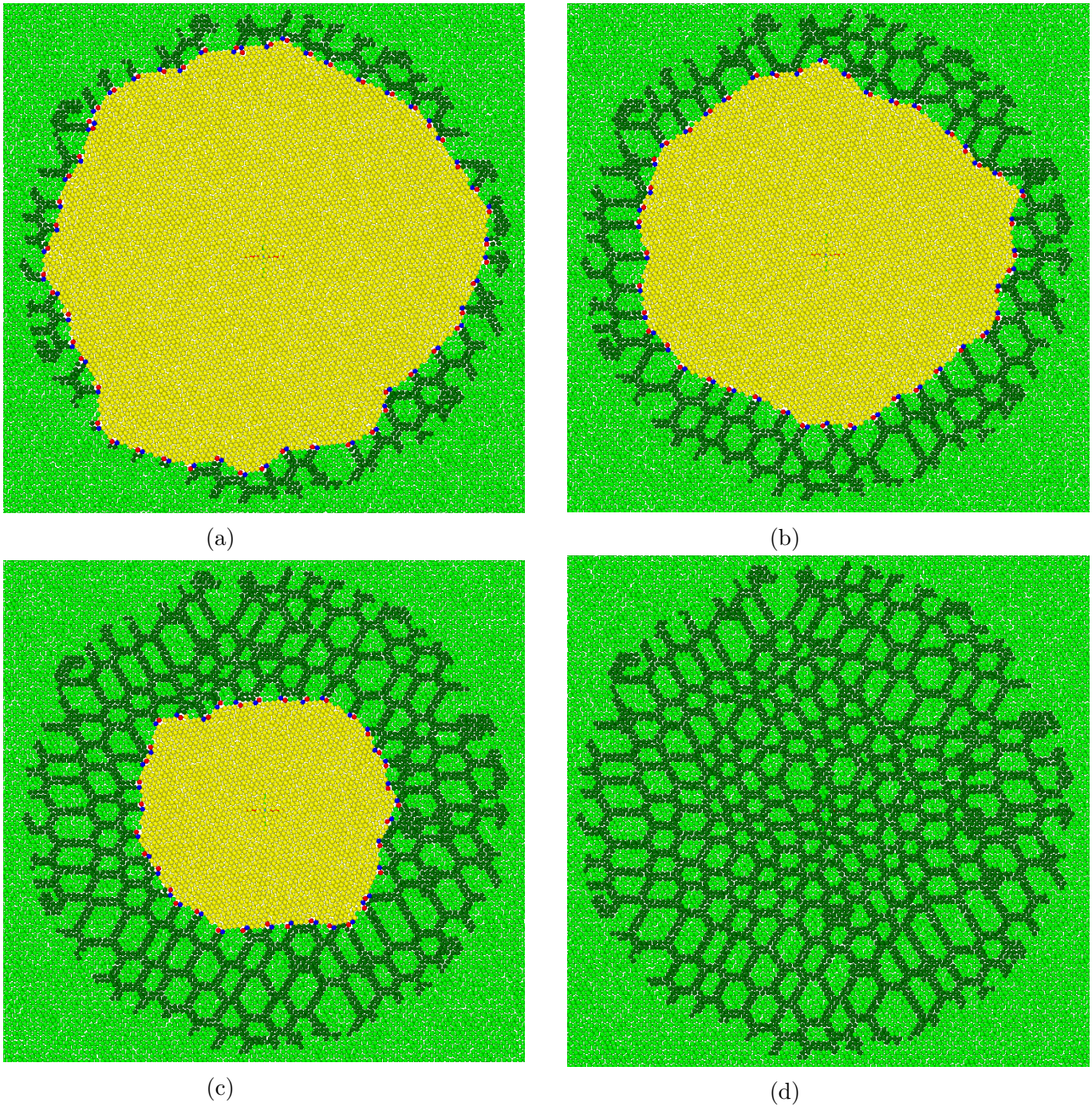

(a) (b) (c) (d)

Figure 4.5.8: *In this figure dislocations are highlighted by a 5-7 couple in blue-red colour. The grain is painted in yellow, the matrix in light green. We coloured the planes along which the dislocations have glided in dark green. These traces form a regular pattern consisting in hexagonal-shaped cells.*

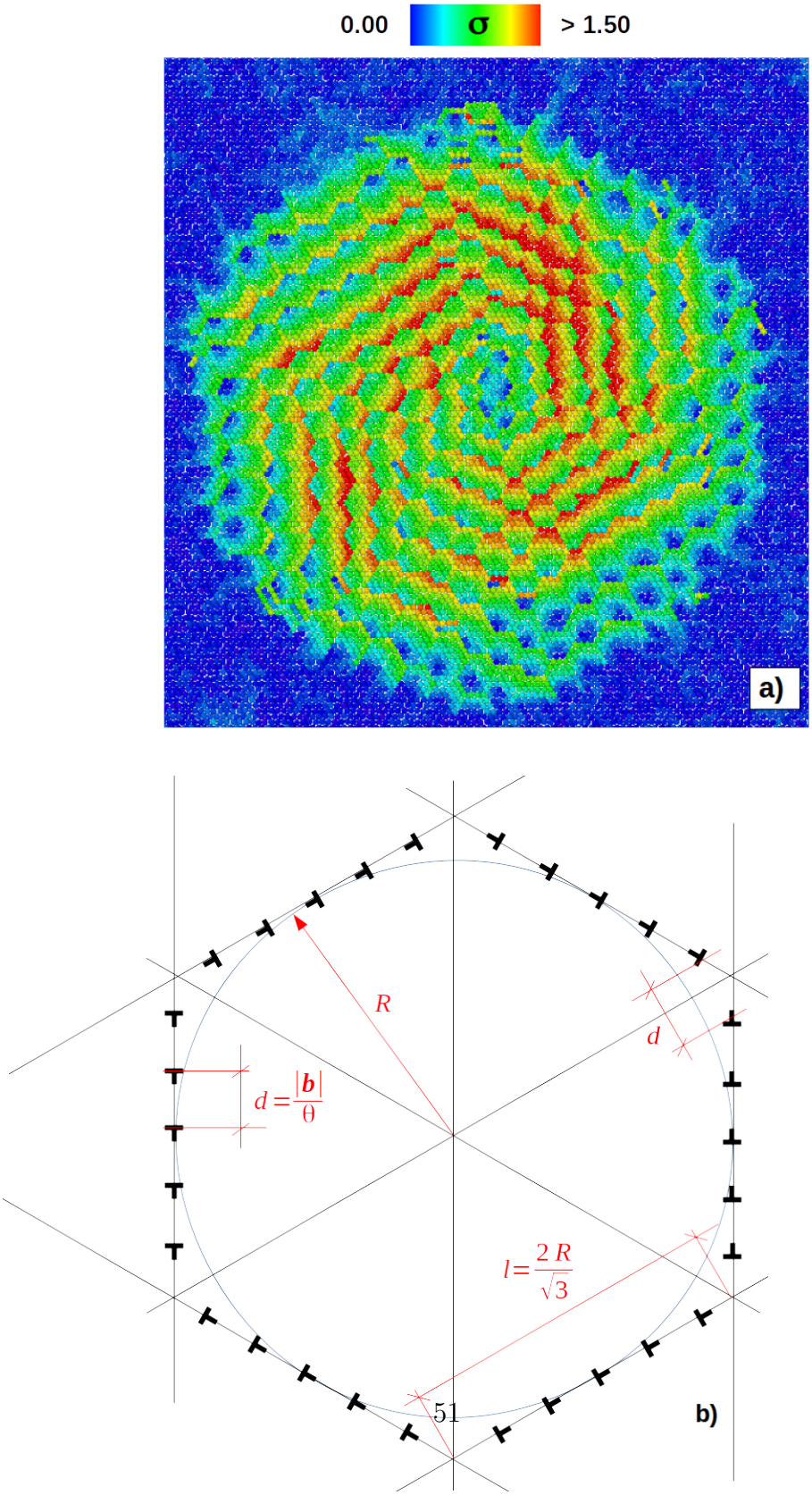

Figure 4.5.9: *In this figure: a) colour map of the residual atomic displacements map after a grain has disappeared for the low misorientation case $\theta = 10°$; b) toy model to describe the boundary migration mechanism. The boundary is simplified by a circumscribed hexagon. The average distance between dislocations on each facet is function of the misorientation θ on the basis of Frank formula.*

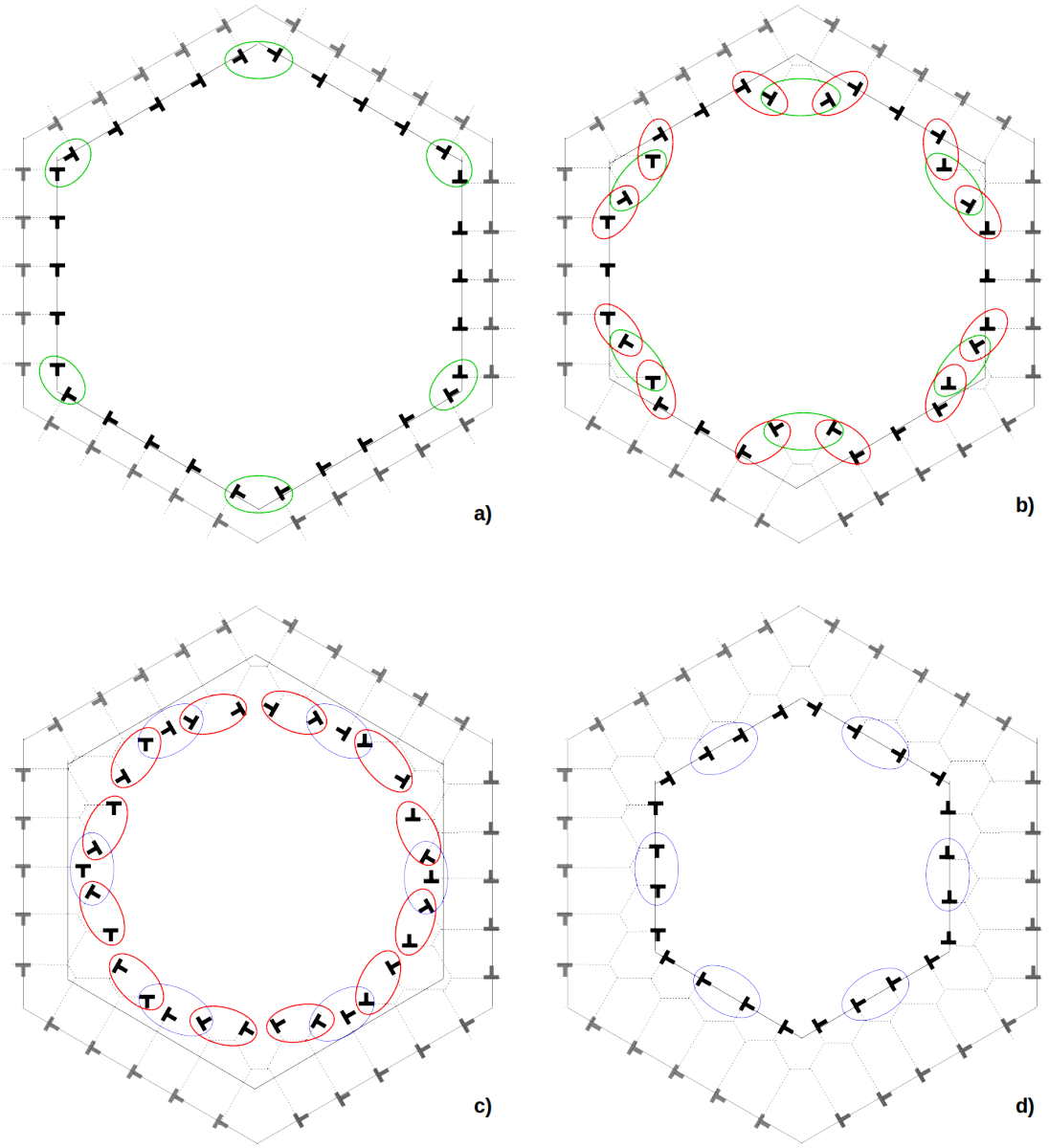

Figure 4.5.10: *A simplified model is proposed to explain the boundary migration by progressive cellular rings: a) simple glide of dislocations; b) an unstable situation is reached at the corners when dislocations with Burgers vectors rotated by* 60° *approach one to the other and proceed to an effective climb mechanism. Pairs of dislocations that undergo this climb process are highlighted by green circles just before -in a)- and just after -in b)- the climb process; c) the dislocations at the corners propagate along the sides by a chain of effective climb events, see red circles in b) and corresponding red circles in c); d) a cellular hexagonal-shaped ring is closed and the dislocation number per side is lowered of 1 thorugh a three-to-two annihilation reaction, see blue circles in c) and d).*

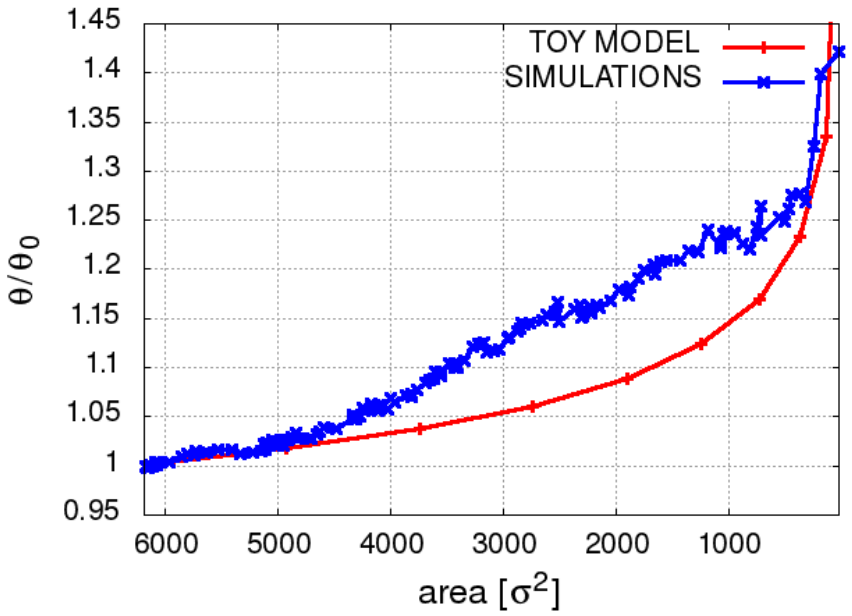

Figure 4.5.11: *Evolution of the misorientation θ in function of the grain size as predicted by the toy model (in red) compared with the results obtained by atomistic simulations (in blue) for $\theta_0 = 10°$.*

4.5.2 High misorientation case

For the high misorientation case, we performed simulations taking different values of the initial misorientation angle θ_0. In Fig. 4.5.12, we report the evolution of the misorientation angle for $\theta_0 = 21.8°$, $27.8°$, $38.2°$, $46.8°$. In all cases, the coupling effect -resulting in a change in θ - is present except for the case of $\theta_0 = 21.8°$ and $\theta_0 = 38.2°$. We also highlight that the rotation sense of the grain (i.e. the sign of coupling) changes in function of θ_0. This fact with the observation that for some particular initial misorientations no coupling effect is present were already highlighted in previous works [58, 52]. A justification presented for the absence of coupling has been the fact that the misorientations $38.2°$ and $21.8°$ correspond to Coincidence Sites Lattice (CSL) for the hexagonal grid. However, this justification is incomplete because, as we can see from Fig. 4.5.12, also the value $27.8°$ and $46.8°$ correspond to CSL. In this section, we illustrate in detail the atomistic mechanism at the origin of the GB migration for the value $\theta_0 = 38.2°$. We will show that the particular mechanism at the origin of the GB migration without coupling is linked not just to the fact that this misorientation corresponds to a CSL but also to the fact that this CSL is the one with lowest periodicity.

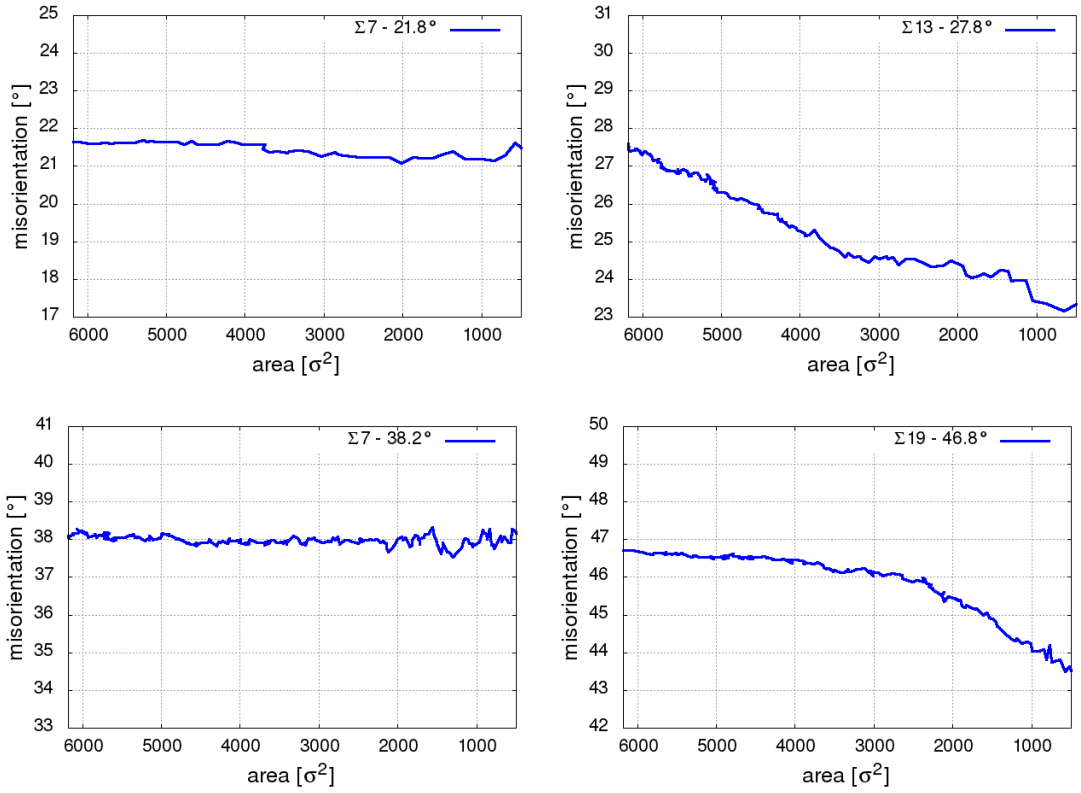

Figure 4.5.12: *Evolution of the misorientation angle for the initial values* $\theta_0 = 21.8°, 27.8°, 38.2°, 46.8°$*, corresponding to different coincidence site lattices.*

Grain boundary structure The GB structure consists of several 5-7 pairs with a spacing of the order of an atomic distance, as shown in Fig. 4.5.13-a. We describe the GB in terms of structural units. Their migration is no longer describable in terms of dislocation dynamics but can be explained in terms of local atomic position readjustments, which lead to the transformation from one lattice to the other [66]. Two main units, highlighted by regular polyhedron in Fig. 4.5.13-a, were identified from our simulations:

- unit A, identified by a single couple (5-7);
- unit B, identified by a double couple (5-7).

These two units are already identifiable by looking at the dichromatic pattern of the boundary, as shown in Fig. 4.5.13-b. Units A are comprised between two coincidence sites along the direction named $\mathbf{e}_1$ while units B are comprised between two coincidence sites along the direction named $\mathbf{e}_2$. In our simulations, the orientation of the units strictly follows this arrangement all along the boundary.

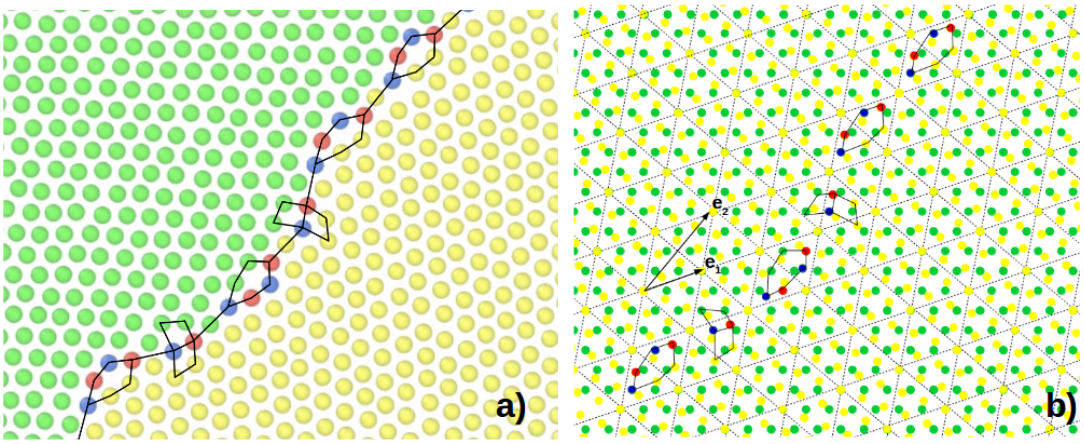

Figure 4.5.13: *In this figure: a) the structural units identified at the GB consisting in a single and in double 5-7 pair; b) the same units identified in the dichromatic pattern.*

Grain boundary migration The grain boundary migrates towards its centre of curvature till the grain totally disappears. No defects are left in the matrix after the grain shrinkage. As already highlighted, during the GB migration there is no significant change in the misorientation θ and accordingly the 5-7 pairs density ρ_{5-7} at the boundary remains constant. We report the evolution of these two quantities as a function of the grain area (normalized by their initial values θ_0 and ρ_{5-7_0}) in Fig. 4.5.14.

In order to clarify the kinematics of migration we kept track of the neighborhood of each atom during the grain shrinkage and, at the same time, we map the magnitude of atomic displacements after the GB passage (see Fig. 4.5.16). Crossing these two informations we observed that:

- there is a set of atoms that hardly move;
- the first neighbour shell of these atoms remains unchanged, even though the atoms within these shells are displaced.

The positions of these "fixed" atoms, shown in Fig. 4.5.16, are not random but are locally distributed on a $\Sigma 7$ coincidence sites grid. In this figure, there are different regions where a $\Sigma 7$ coincidence sites grid can be observed, with transition zones between them. This is linked to the fact that 7 different CSL grids can be defined for a $\Sigma 7$ grain boundary, the different grids being related by a translation. All the above observations suggest that, for the special case of $\theta_0 = 38.2°$, the

migration of the boundary occurs by *local* adjustment of atoms rotating around these "fixed" positions. To verify this hypothesis, using the approach illustrated in section 4.3.3, we calculate a local deformation gradient $\mathbf{F}_i$ and the corresponding non-affine-square displacement $D^{(i)^2}$. The results of this calculation are reported in Fig. 4.5.17a, where we can see that the deviation $D^{(i)^2}$ is almost zero for atoms that are on the coincidence sites while it takes high values for the atoms around them. Furthermore, for atoms inside the inital grain and for which $D^{(i)^2} < 0.1$, we have analyzed the deformation gradient $\mathbf{F}^i$. The histogram of the four components of $\mathbf{F}^i$ are presented in Fig. 4.5.17b. From these histograms, we conclude that all the considered atoms have the deformation gradient

$$\overline{\mathbf{F}} = \begin{pmatrix} 0.9320 & -0.3738 \\ 0.3735 & 0.9291 \end{pmatrix} \tag{4.5.2}$$

with a standard deviation smaller than 1.5 10^{-3} on each component. Because the standard deviations are small, $\overline{\mathbf{F}}$ can reasonably be thought as representative of the local deformation gradient $\mathbf{F}^i$. We can verify that $\det \overline{\mathbf{F}} \approx 1$ and $\overline{\mathbf{F}}^T \overline{\mathbf{F}} \approx \mathbf{I}$. These properties allow us to identify $\overline{\mathbf{F}}$ as a rotation matrix. In conclusion, the movements of neighbours around atoms in coincidence site position can be interpreted as rigid rotation. The entity of this rotation can be calculated as $\theta \approx \sin^{-1}(\overline{F}_{21}) = 21.9°$. This value is coherent with the rotation needed to bring the lattice in the grain coincident with the lattice in the matrix.

The fact that atoms on coincidence position behave as "fixed points" implies that no rotation of the grain can occur during the boundary migration i.e. the boundary must move normally to its plane. The local atomic movement which leads to this normal migration can be described in terms of dynamics of 5-7 defects (Fig. 4.5.15(b-e)). These 5-7 defects (blue-red atom pairs), located at the grain boundary, migrate in between the coincidence lattice sites atoms (black atoms), the latter keeping their 6 nearest neighbours. The evolution of the orientation of the 5-7 defects during their migration reveals that their migration cannot be described as a glide mechanism.

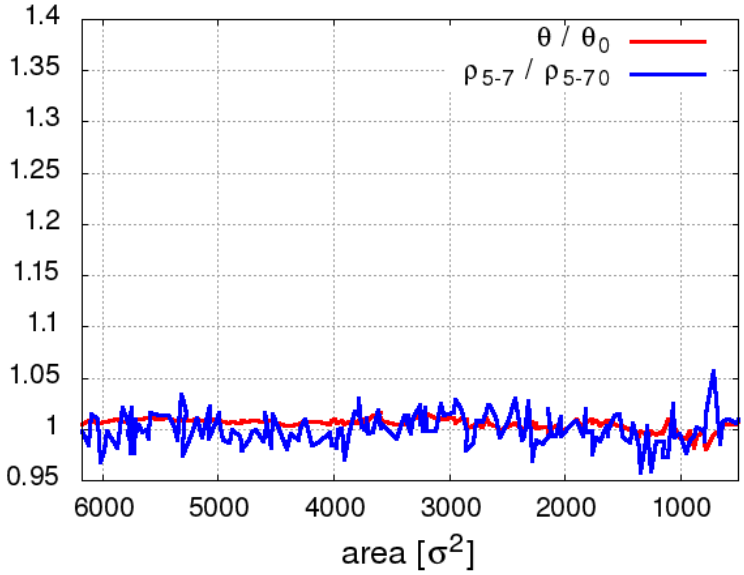

Figure 4.5.14: *Normalized 5-7 pairs density* ρ_{5-7}/ρ_{5-7_0} *along the boundary (blue curve) and change in the misorientation angle* θ/θ_0 *(red curve) during grain shrinkage for the initial misorientation* $\theta_0 = 38.2°$.

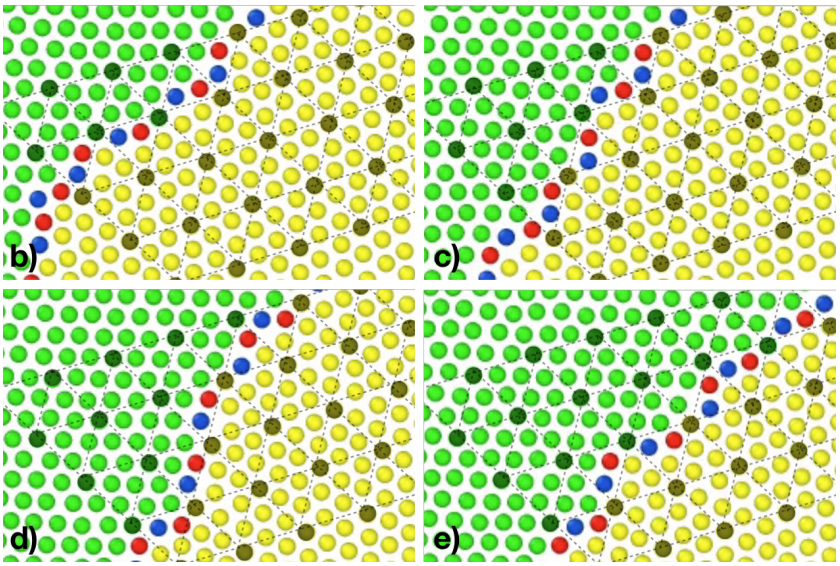

Figure 4.5.15: *Snapshots illustrating the movement of structural units around the coincidence sites during the grain shrinkage. The coincidence sites are highlighted in black and the structural units A and B by single or double red-blue couples, respectively. The matrix is coloured in light green while the grain in yellow.*

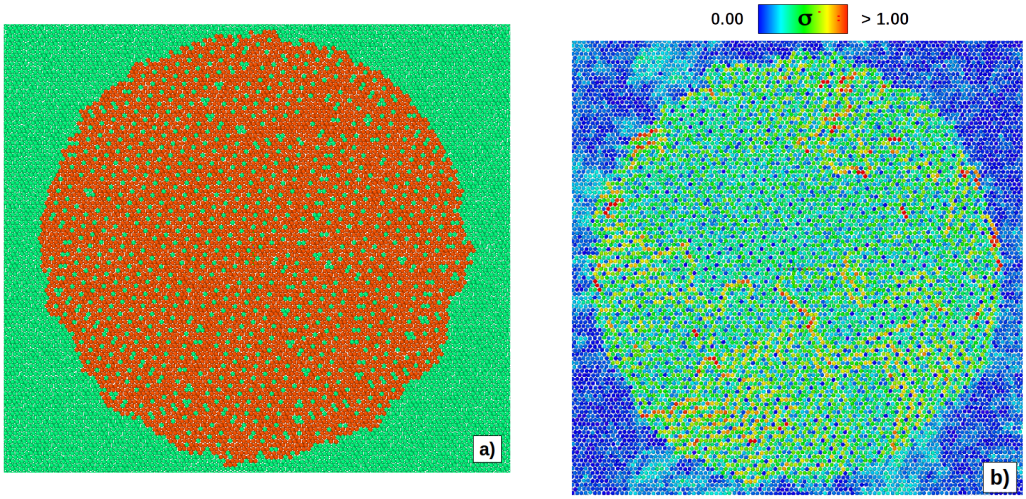

Figure 4.5.16: *Atomic structure after the grain shrinkage for* $\theta = 38.2°$*: a) atoms which have not seen a change in their nearest neighbours are highlighted in green while the other atoms in orange; b) the map of atomic displacement magnitude after the grain boundary passage.*

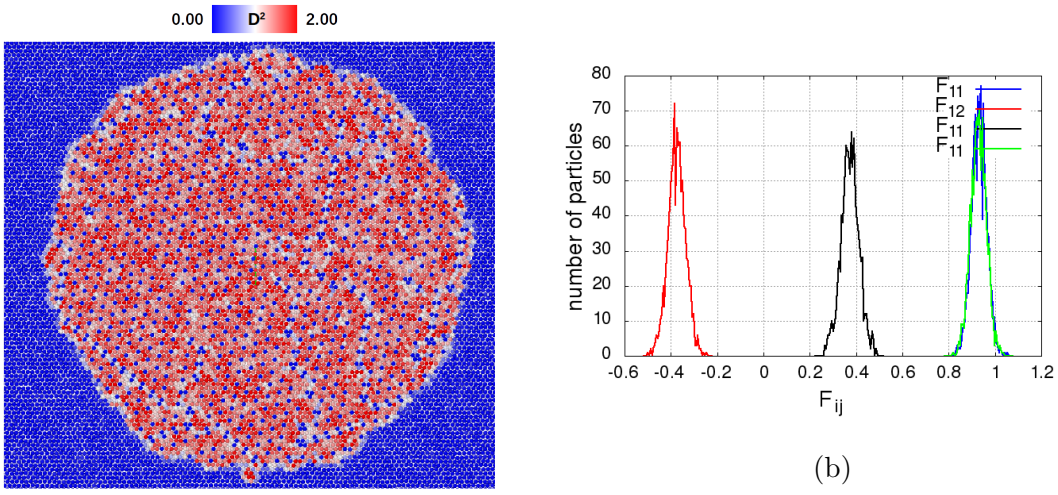

(a) (b)

Figure 4.5.17: *a) colour map of the non-affine square displacement* $D^{(i)^2}$ *for* $\theta = 38.2$*; b) histograms of the local deformation gradient coefficient for atoms, initially belonging to the central grain, with* $D^{(i)^2} < 0.1$.

4.6 Discussion

In this chapter we have shown the results of a first application of the overdamped Langevin dynamics to GB migration. For this purpose, we simulated the shrinking of a 2D circular island grain embedded in a monocrystalline matrix at fixed temperature. This study has lead to two main results:

- the validation of the modelling approach proposed by comparison with Molecular Dynamics simulations;
- the analysis of the atomic mechanisms at the base of GB migration in the low and high misorientation case.

The comparison between LG and MD simulations has been done by following the evolution of two observables: (i) the misorientation angle θ, (ii) the number of defects along the boundary. The agreement between the two methods is really good so we are confident in the applicability of the stochastic dynamics illustrated in chapter 2 to the study of crystalline materials.

By analysing the structure and the atomic mechanisms of migration for different misorientation, we highlight that:

- for $0° < \theta_0 < 10°$ the migration proceeds through a combination of different dislocation mechanisms. The GB motion proceeds by steps, lowering progressively the number of dislocations *via* propagation of the Burgers vectors along the boundary and three-to-two annihilation mechanism. The propagation is promoted by a particular type of interaction between dislocations that we named "effective climb". This migration mechanism has been further explained by the use of a toy model;
- we verified that for the particular high angle grain boundary $\theta_0 = 38.2°$, which corresponds to a coincidence site $\Sigma 7$, the migration occurs by local readjustment of atomic positions. These local movements correspond to a rotation around atoms in coincidence site position, which hardly move. The fact that coincidence sites act as "fixed points" during the GB migration prevents the embedded grain to rotate and thus exclude the presence of coupled tangential-normal motion.

The simulations performed in this first step of our work have a rather "abstract" character, in the sense that we limited our studies to 2D cases and we use a simple pair potential to describe atomic interactions. In the next chapter, we show the results of the second application of the model proposed in 3D for which we used a many-body potential which represents the thermo-mechanical properties of a specific material of interest (Titanium).

Chapter 5

2nd application: $\beta \rightarrow \alpha$ phase transition in pure titanium

5.1 Introduction

After the study of curvature driven grain boundary motion, we decided to apply the model to another important phenomenon involved in metals microstructural evolution i.e. martensitic phase transition. Early works on the atomistic modelling of martensitic phase transition date back to 1980 [67, 68, 69]. From that time, thanks also to the development of new many-body potentials in 1990, a wide range of atomistic studies on the stress or temperature induced transition have been performed. Each of these studies address a specific problematic and/or a particular material. Here we give a list of some relevant works: Rubini et al. [70] (Ni-Al alloys, 1993), Entel et al. [71, 72, 73] (Fe-Ni, 1998-2000), Grujiicic et al. [74, 75, 75] (Fe-Ni and titanium alloys, 1995-1996), Morris [76] (Zr, 2001), Ackland et al. [77, 78, 79, 80] (Zr, 1998 to 2011), Morrison et al. [81, 82] (Ni-Al, 2014), Ding et al. [83, 84, 85, 86], Ma et al. [87] (Ni-Ti, 2017), Li et al. [88] (Ti, 2015), Ko et al. [89, 90] (Ni-Ti, 2015-2017).

In the present study, we focused on the $\beta \rightarrow \alpha$ transition in pure titanium and, in particular, on the effect of mechanical constraints in the resulting microstructure. The first step of our work was to find a suitable interatomic potential for simulating the transition and implement it in our code. The second step was to perform atomistic simulations of the microstructure evolution with different loading conditions.

5.2 Basics on titanium

In this section, we give a general introduction to titanium basic properties and to its behaviour in different temperature-pressure conditions.

5.2.1 General properties

Titanium has several attractive properties; low density if compared with other structural alloys such as steel, high strength and elastic modulus with respect to other light weight metals such as aluminium, good resistance to corrosion and bio-compatibility. Some indicative values are reported in Tab. 5.1. In the aeronautic field, titanium is combined with other elements (such as molybdenum, nickel, aluminium, etc.) to obtain high-performance alloys used for aero-frames and engines. Furthermore, its low reactivity makes it attractive for nuclear waste storage, chemical and power industries, instrumentation and implantation in the bio-medical field. From this brief summary, the interest in understanding the behaviour of this material under thermo-mechanical solicitations clearly emerges.

	Ti	Fe	Ni	Al
Melting temperature [°C]	1670	1538	1455	660
Room temperature E [GPa]	115	215	200	72
Density [g/cm^3]	4.5	7.9	8.9	2.7

Table 5.1: *Some guiding values of titanium main properties compared with other metals (from [5]).*

5.2.2 Phase diagram and polymorphism

Similarly to other transition metals such as zirconium and hafnium, titanium exhibits a temperature induced as well as pressure induced polymorphism i.e. it adopts different crystal structures under different thermo-mechanical conditions. Its phase diagram is reported in Fig. 5.2.1.

Three different solid phases exists for this material. At a temperature $T > 1150$ K and atmospheric pressure, titanium has an open BCC structure (the so-called β phase). When temperature is lowered, this structure becomes unstable and the material adopts a close-packed HCP structure under atmospheric conditions (the so-called α phase) or an hexagonal structure (referred as ω phase) in high pressure conditions [91]. In the present work we focused on the temperature induced $\beta \rightarrow \alpha$ phase transition.

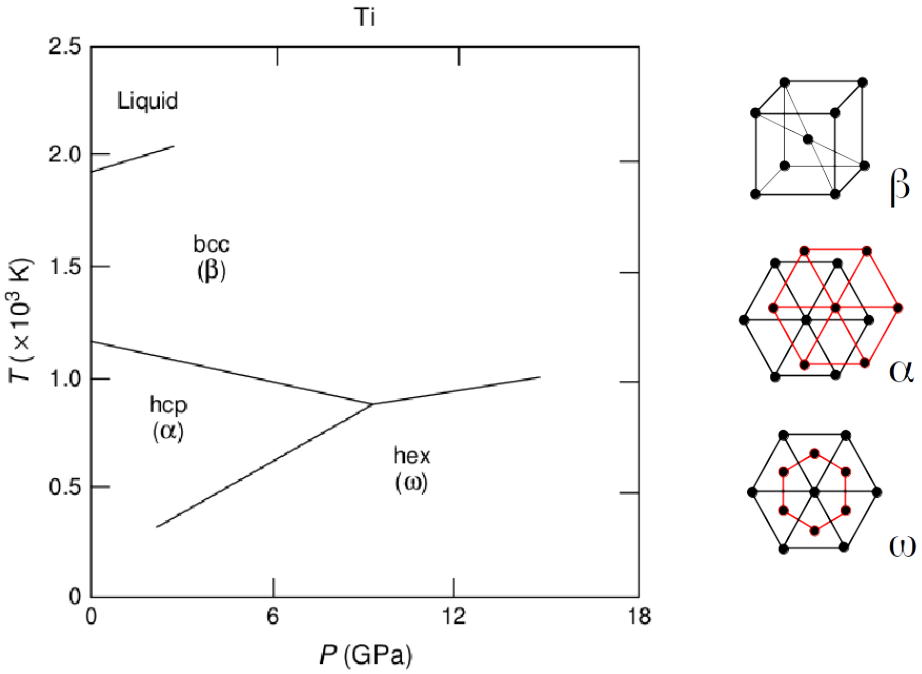

Figure 5.2.1: *Experimental temperature-pressure phase diagram [2] for pure titanium (image modified from [3]).*

5.2.3 Crystallography of the $\beta \rightarrow \alpha$ phase transition

Here we give some basic concepts in the crystallographic analysis of the $\beta \rightarrow \alpha$ transition. For a more detailed treatment of the subject we address the reader to the following texts [3, 92].

Local lattice deformation

The transition from the open BCC to the close-packed HCP structure occurs martensitically in the sense that each atom in one structure can be mapped to a particular site in the other and no diffusion is involved. It is commonly accepted that locally the transition proceeds by the so-called "Burgers mechanism" which states the following correspondence between the lattices of the parent and child phase [93]:

$$(110)_{BCC} \| (0001)_{HCP} \; ; \; [\bar{1}11]_{BCC} \| [11\bar{2}0]_{HCP} \tag{5.2.1}$$

The $(0001)_{HCP}$ basal plane is derived from the $(110)_{BCC}$ plane in the parent phase. The close-packed directions $[1\bar{1}1]_{BCC}$ and $[\bar{1}11]_{BCC}$ lying on the $(110)_{BCC}$ plane transform to two close-packed directions $\langle 11\bar{2}0\rangle_{HCP}$. On the basis of this correspondence, the transformation involves a contraction η_1 along the $[001]_{BCC}$ direction and an elongation η_2 along the $[\bar{1}10]_{BCC}$ direction, as schematically shown in Fig. 5.2.2. An elongation η_3 along the $[110]_{BCC}$ direction and an alternate shuffling of $(110)_{BCC}$ planes give the final HCP structure.

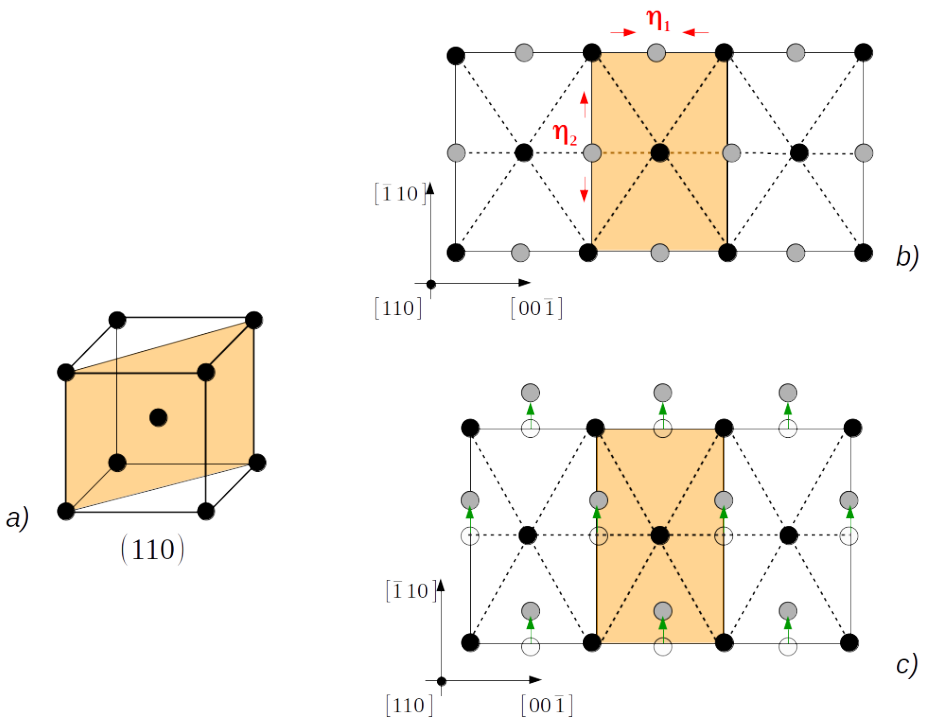

Figure 5.2.2: *In the figure: a) the* $(110)_{BCC}$ *plane becoming the basal plane of the HCP structure. The transition involves b) a deformation of the plane and c) an alternate shuffling of* $(110)_{BCC}$ *planes.*

Taking as a basis the three vectors $\mathbf{e_1}' = [0,0,\bar{1}]$, $\mathbf{e_2}' = [\bar{1},1,0]/\sqrt{2}$, $\mathbf{e_3}' = [1,1,0]/\sqrt{2}$ in the cubic frame, this lattice deformation is described by the matrix:

$$\mathbf{U}' = \begin{pmatrix} \eta_1 & 0 & 0 \\ 0 & \eta_2 & 0 \\ 0 & 0 & \eta_3 \end{pmatrix}$$

In the following, we will refer to this deformation as *Bain strain*. We underline that it describes the overall change in shape of the cell comprised between two

HCP basal planes i.e. it does not describe the alternate shuffling movement of $(110)_{BCC}$ planes. Knowing the lattice parameters a_0 and (a, c) of the parent and child phase, the principal strains η_1, η_2, η_3 can be computed:

$$\eta_1 = \frac{a}{a_0};\ \eta_2 = \sqrt{\frac{3}{2}}\frac{a}{a_0};\ \eta_3 = \frac{c}{\sqrt{2}a_0} \tag{5.2.2}$$

Rewriting matrix $\mathbf{U}'$ in the cubic base $\mathbf{e_1} = (1, 0, 0)$, $\mathbf{e_2} = (0, 1, 0)$, $\mathbf{e_3} = (0, 0, 1)$ we obtain:

$$\mathbf{U} = \frac{1}{2}\begin{pmatrix} \eta_2 + \eta_3 & \eta_3 - \eta_2 & 0 \\ \eta_3 - \eta_2 & \eta_3 + \eta_2 & 0 \\ 0 & 0 & 2\eta_1 \end{pmatrix}$$

The original BCC structure has six equivalent $(110)_{BCC}$ planes. Consequently, six different Bain strain can be defined. The matrix representing these strains are listed in Tab. 5.2. In the following, we will refer the term *variant* to this distinction in terms of Bain strain. In this sense, there are six possible HCP variants.[1]

[1]Some works (see for example [94, 95]) report 12 different variants of the HCP phase. The contradiction with our analysis is only apparent. In these works the term variant refers to a distinction in terms of *orientation* of the child phase with respect to the parent phase. As already underlined, in our work the term variant refers to a distinction in terms of *local strain* of the lattice.

BAIN STRAIN MATRIX	
$\mathbf{U_1} = \frac{1}{2}\begin{pmatrix} 2\eta_1 & 0 & 0 \\ 0 & \eta_2+\eta_3 & \eta_3-\eta_2 \\ 0 & \eta_3-\eta_2 & \eta_2+\eta_3 \end{pmatrix}$	$\mathbf{U_2} = \frac{1}{2}\begin{pmatrix} 2\eta_1 & 0 & 0 \\ 0 & \eta_2+\eta_3 & \eta_2-\eta_3 \\ 0 & \eta_2-\eta_3 & \eta_2+\eta_3 \end{pmatrix}$
$\mathbf{U_3} = \frac{1}{2}\begin{pmatrix} \eta_2+\eta_3 & 0 & \eta_3-\eta_2 \\ 0 & 2\eta_1 & 0 \\ \eta_3-\eta_2 & 0 & \eta_2+\eta_3 \end{pmatrix}$	$\mathbf{U_4} = \frac{1}{2}\begin{pmatrix} \eta_2+\eta_3 & 0 & \eta_2-\eta_3 \\ 0 & 2\eta_1 & 0 \\ \eta_2-\eta_3 & 0 & \eta_2+\eta_3 \end{pmatrix}$
$\mathbf{U_5} = \frac{1}{2}\begin{pmatrix} \eta_2+\eta_3 & -\eta_2+\eta_3 & 0 \\ -\eta_2+\eta_3 & \eta_2+\eta_3 & 0 \\ 0 & 0 & 2\eta_1 \end{pmatrix}$	$\mathbf{U_6} = \frac{1}{2}\begin{pmatrix} \eta_2+\eta_3 & \eta_2-\eta_3 & 0 \\ \eta_2-\eta_3 & \eta_2+\eta_3 & 0 \\ 0 & 0 & 2\eta_1 \end{pmatrix}$

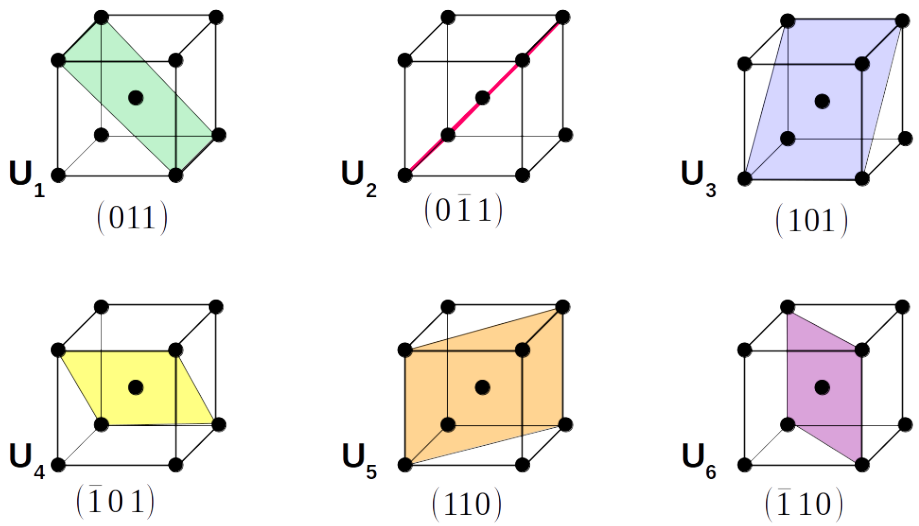

Table 5.2: *The six* $\{110\}_{BCC}$ *planes that can become the* $(0001)_{HCP}$ *basal plane and the corresponding six Bain strains.*

Twinning modes

Martensitic microstructures are typically characterized by the occurrence of twins. A twin is a visible coherent interface in a crystal which satisfies the following [96]:

- the lattice on one side can be obtained by a simple shear of the lattice on the other;
- the lattice on one side can also be obtained by a rotation of the lattice on the other.

The possible twin planes between two different variants can be obtained by solving the so-called "twinning equation":

$$\mathbf{Q}\mathbf{U}_j - \mathbf{U}_i = \mathbf{a} \otimes \mathbf{n} \tag{5.2.3}$$

where $\mathbf{Q}$ is a rotation, $\mathbf{U}_j$ and $\mathbf{U}_i$ are the associated Bain strain, $\mathbf{n}$ is the normal to the twin plane and $\mathbf{a}$ is the shear direction. When equation (5.2.3) is solvable, it leads to two solutions for $\mathbf{n}$ and $\mathbf{a}$. It can be verified that for all the possible couples of variants listed in Tab. 5.2 equation (5.2.3) admits solutions. Moreover, there are three possible twinning modes for the transformation considered:

- the variants pairs 1-2, 3-4 and 5-6 (which do not share a $\langle 111 \rangle_{BCC}$ direction) can form *compound twins* with a $\{100\}_{BCC}$ plane which becomes the $\{2\bar{1}\bar{1}0\}_{HCP}$ plane in the child phase (see Fig. 5.2.3);
- the other possible variants pairs (which all share a $\langle 111 \rangle_{BCC}$ direction) can form a *Type I twin* with a $\{110\}_{BCC}$ plane which becomes a $\{10\bar{1}1\}_{HCP}$ plane in the child phase (see Fig. 5.2.4)) and the reciprocal *Type II twin* .

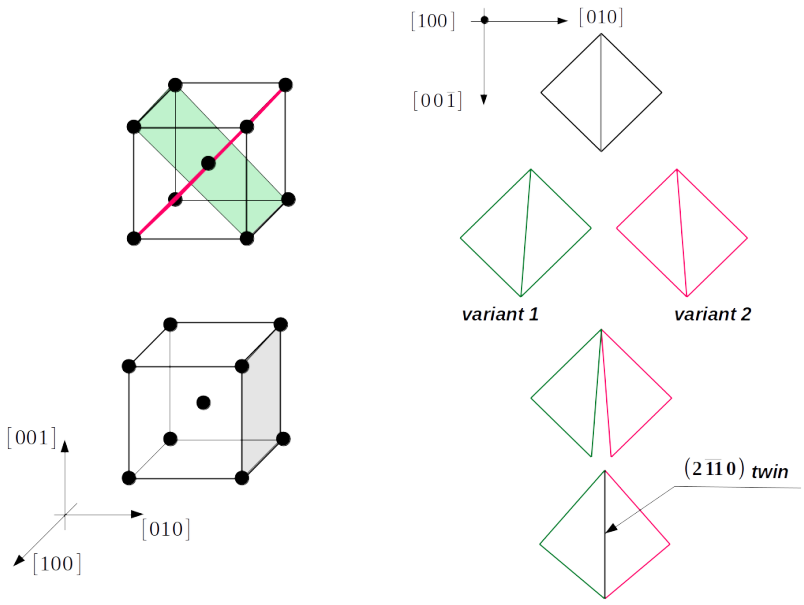

Figure 5.2.3: *Example of compound twin between variant 1 and 2 (the future basal planes are highlighted in colours while the twinning plane in grey).*

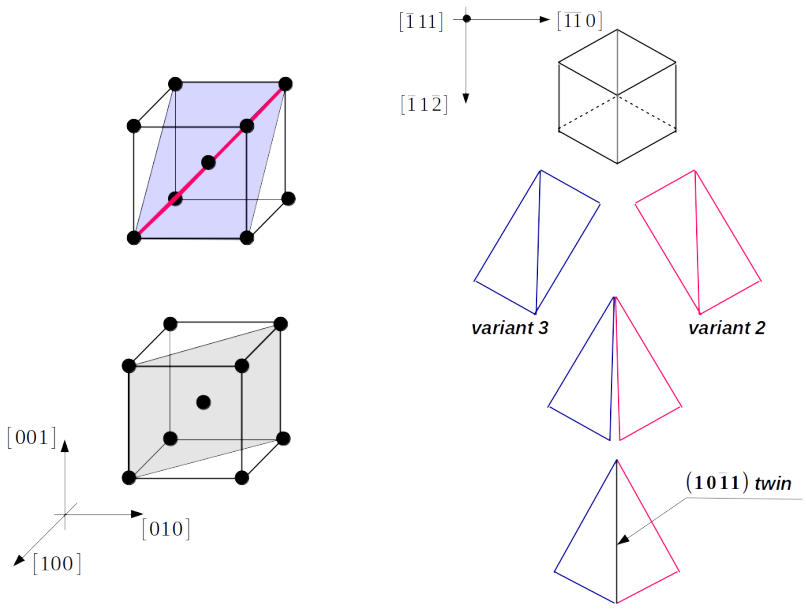

Figure 5.2.4: *Example of Type I twin between variant 2 and 3 (the future basal planes are highlighted in colours while the twinning plane in grey).*

5.3 Post-processing tools

Before discussing numerical simulation results, we describe in this section the post-processing tools used to identify the different phases and variants in our simulations.

5.3.1 Phases identification

The crystallography of the different phases is identified by the use of the Polyhedral Template Match analysis (PTM in the following) [97], a rather newly developed tool implemented in the visualization software OVITO. This algorithm allows the identification of different crystallographic structures even when strong thermal vibrations are present. We address the reader to the specific documentation at: https://www.ovito.org/manual/particles.modifiers.polyhedral_template_matching.html.

5.3.2 Variants identification

The identification of the different variants is done by using a code of our own. In simulations as well as in experiments, variants identification is crucial for the analysis of microstructures. This can be done in different ways:

1. by studying the orientation of the HCP final products with respect to the parent BCC phase. This orientation is the result of the lattice distortion and of the subsequent accommodation phenomena;

2. in a finer way, when working with atomistic simulations, by calculating a local strain to describe the lattice distortion, as proposed in [98].

To analyse our results we choose this second option. To calculate the local atomic strain we implemented the following procedure:

- we start from a BCC structure with crystal axis $\langle 100 \rangle_{BCC}$ parallel to the main frame axis. For every atom i, we consider six possible sets of neighbours by taking six different configurations defined on the basis of the six cubic cells which can deform into the orthorhombic one, as schematically illustrated in Fig. 5.3.1. The alternate shuffling of $\{110\}_{BCC}$ planes is not described by the overall deformation of the lattice so half of the atoms must be considered in the six possible configurations;

- using the approach illustrated in chapter 4, section 4.3.3, we calculate for each atom i six deformation gradients $\mathbf{F}_i^*$ and, by polar decomposition, six strains $\mathbf{U}_i^*$ each one associated to a $\{110\}_{BCC}$ plane in the undeformed configuration;

- the local strain for atom i is defined as the $\mathbf{U}_i^*$ with minimum D^2. On the basis of this assignment, we label the atom i as belonging to the corresponding variant.

The non-affine displacement D^2 quantifies the degree at which the local change in the lattice can be described using an affine transformation. In the results later shown, we set a threshold D^2_{lim} for this parameter above which the approximation is considered not meaningful and atoms are then excluded by calculations. On the basis of the definition of D^2 (see chapter 4, section 4.3.3), this corresponds to impose a limit *on average* on the mean square difference between the actual relative position $\Delta\mathbf{r}_{ij}(t^*)$ between the atom i and its neighbour j and the one estimated by the action of $\mathbf{F}_i$ on $\Delta\mathbf{r}_{ij}(0)$.

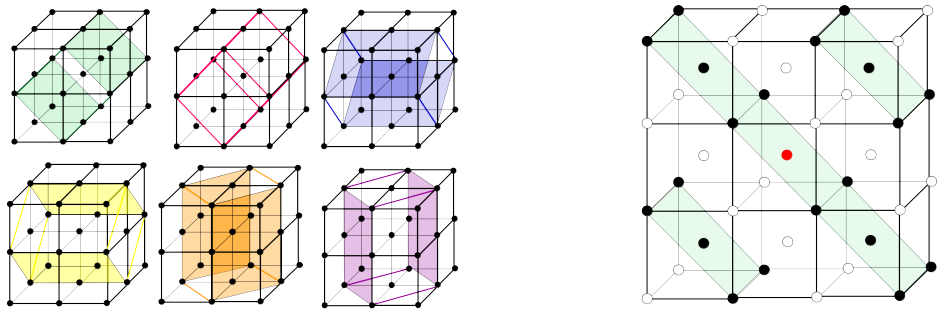

(a) (b)

Figure 5.3.1: *a) the six cubic cells which can deform in the orthorhombic cell are highlighted in different colours (note that central atoms are not shown for sake of simplicity); b) an example of neighbour set (coloured in black) for a given atom i (coloured in red) for one of the six configurations considered.*

5.4 Choice of the interatomic potential

The first step of our work was the selection of a relevant interatomic potential for simulating the $\beta \rightarrow \alpha$ transition. After a literature review, we selected three "candidates". Because these potential were already implemented in the code LAMMPS, we performed preliminary tests in Molecular Dynamics to choose the most suitable one. We then implemented this potential in the Langevin code.

5.4.1 Literature review on interatomic potentials

From the library "Interatomic Potentials repository project" (https://www.ctcms.nist.gov/potentials/) we found the following potentials developed for titanium:

- a Finnis-Sinclair potential proposed by Ackland and co-workers in 1992 [99]. This potential has been used to study plastic behaviour and defects properties of pure titanium at low temperature [100, 101, 102, 85]. However, we found no application to modelling temperature induced phase transition;
- an EAM type potential proposed by Johnsons and co-workers in 2003 [103]. This potential was developed in the specific context of vapor-deposited multilayers. Furthermore, we did not find any application of this potential to the atomistic modelling of titanium. Consequently, we decided to discard it;
- EAM type potentials recently proposed by Mendelev and Ackland in 2016 [104]. The authors developed three different potentials, one of them (the Ti1, see the article) with the specific purpose of describing the $\beta \rightarrow \alpha$ phase transition. Maybe because recently developed, we have not been able to find any application of this potential;
- a MEAM type potential proposed by Hennig and collaborators in 2008 [105]. This potential was developed with the specific purpose of being able to catch the polymorphism of the material. It has mainly been used for the study of the pressure induced $\alpha \rightarrow \omega$ phase transition [88, 86], although an application in the field of temperature induced $\beta \rightarrow \alpha$ transition can be found in [106].

5.4.2 Pilot tests

As previously mentioned, to choose between the above listed "candidates" the one to be implemented in the Langevin code we performed some pilot tests with Molecular Dynamics, described in the following section.

Simulation setup

The simulations performed consist in two steps:

- equilibration of a BCC monocrystalline structure at high temperature (T =1400 K);
- quenching of the structure previously equilibrated (T =700 K).

The simulation box size is set equal to $36 \times 36 \times 36\ a_0^3$, where a_0 is the BCC lattice constant. The number of atoms is 93312. Periodic boundary conditions are applied

in all the directions. The simulations are performed in the (N**P**T) ensemble with a Nosé-Hoover thermostat and barostat to control temperature and pressure. The quenching is simulated by an instantaneous rescaling of temperature.

The result expected from this test is an initially stable BCC structure and a subsequent transition to HCP when temperature is lowered.

Results

We performed simulations with the three potentials listed in section 5.4.1 and we obtained the following results:

1. the EAM potential proposed in [99] does not show a stable BCC structure at high temperature. Independently from the temperature value, the system was always becoming unstable and switching to an HCP structure;

2. the EAM potential proposed by Mendelev and Ackland in [104] shows a stable BCC structure at high temperature. However, no transition was seen after quenching even after 1 nano-second of annealing at 700 K;

3. the MEAM potential proposed by Hennig [105] shows a stable BCC structure at high temperature and the transition to HCP as a consequence of quenching.

Comments

The first potential tested does not predict a stable BCC phase at 1400 K. A possible reason is that this potential was developed by fitting only the properties of HCP titanium, ignoring the presence of the BCC phase stable at high temperatures.

For the two other potentials, a stable BCC phase exists at high temperatures. However, only with the MEAM potential we observe transition after quenching. The reason why the transition is not seen using the other potential can be:

- the absence of any angular dependence in the embedding term (which on the other side is present in MEAM potential) so that the directional nature of bonding typical of transition metals such as titanium is not described;

- a high energy barrier for the nucleation of the HCP phase.

In conclusion, on the basis of the results obtained from the pilot tests, we decided to use the MEAM potential developed by Hennig. We underline that the MEAM has a higher computational costs if compared to the EAM. Consequently, a computational efficient implementation becomes important. For this purpose, we referred to the following work [107, 108] and enriched it by implementing the computation of the virial terms.

5.5 Study of the influence of mechanical constraints on martensite microstructures

In this section, we present and discuss the results of our study on the effect of mechanical constraints preventing a free volume and/or shape change of the region where the martensitic transition takes place. These constraints can be due to the presence of neighbouring grains in a polycrystal or, for example, to a specific growth sequence of martensite plates (see section 5.6). Their influence on the martensitic microstructure in terms of number of variants, type of interfaces and other defects generated, has been mentioned in several experiences on martensite [109, 4, 110] and also on bainite [111, 112]. The impact of the microstructural morphology on the final mechanical properties of a material justifies the interest in a deeper investigation of this influence.

5.5.1 Simulations setup

The simulations performed consist in the equilibration of a BCC structure at 1400 K and subsequent quenching at 700 K. The quenching is realized by instantaneous rescaling of the temperature. The simulation box size is set equal to $36 \times 36 \times 36\ a_0^3$ and periodic boundary conditions are applied in all directions. The total number of atoms is 93312. The simulations are performed with the Langevin code in the (NVT) ensemble and compared with the ones performed with MD in the (N**P**T) ensemble. Real conditions experienced by a given region in a material are expected to be an intermediate between these two cases. However, these two extreme scenarios are useful for a global understanding of the influence of local constraints which prevent a free change of shape and/or volume of the matrix around the martensite nuclei.

5.5.2 Simulations results

Unconstrained conditions (NPT ensemble)

In unconstrained conditions, the simulation box is free of changing shape and the system evolution is guided by the minimization of Gibbs free energy. The microstructure evolution has been analysed by performing MD simulations in the (N**P**T) ensemble.

After equilibration, the system turns to an HCP structure as a consequence of quenching. We report in Fig. 5.5.1a the evolution of the BCC and HCP phases percentages during the transition (the RMSD cutoff for the PTM analysis is set equal to 0.14). As we can see, almost no BCC phase is left after the transformation is completed. The simulation box develops a large shear and some defects are

generated. These defects consist in twin boundaries, stacking fault and antiphase boundaries and are later discussed. In Fig. 5.5.1b we report the number of atoms belonging to a given variant as a function of the time step ($D^2_{lim} = 6.5$, number of neighbours $N_n = 22$). As we can see, at the really beginning of the transition all the six variants nucleate. However, quickly two of them become dominant and form the final microstructure. In the case here examined, the variants selected are the 2 and 3 (see Tab. 5.2). This pair shares the $[\bar{1}11]_{BCC}$ direction so the final microstructure can be analysed by taking a slice orthogonal to this direction, as shown in Fig. 5.5.3.

In Fig. 5.5.2 four snapshots of the microstructural evolution are reported. In the figure we show only the atoms classified as HCP on the basis of the PTM analysis. At the beginning, stable nuclei of all the six variants appear. In a first step, all the different HCP domains develop. Later, some domains disappear leaving some defects in the final structure composed by only two variants. As typically seen in martensite, the two variants form a laminate microstructure which consists of parallel $\{10\bar{1}1\}$ twins, shown more in detail in Fig. 5.5.4-a. As shown by atomistic calculations [113], the $\{10\bar{1}1\}$ boundary has lower energy than the $\{2\bar{1}\bar{1}0\}$. Consequently, it is reasonable to expect that the system favours the formation of this type of boundaries and consequently the selection of a variant pair which share a $\langle 111\rangle_{BCC}$ direction. The twins span all the simulation box thus showing that periodic BC have a rather strong influence in the final microstructure for small systems. Various stacking faults are generated after transition. Some of them extend through two twins. In previous works, their formation has be imputed to the rigid rotation of variant domains to form the $(10\bar{1}1)$ boundary [79] (see Fig. 5.2.4). When a given $\langle 110\rangle_{BCC}$ plane deforms, two different directions of shuffling are possible. This give rise to two possible HCP structures rotated of 180° around the c-axis, which have been called a couple of *anti-variants* [84]. In our simulations, when two HCP domains with opposite shuffle directions meet they form an interface which corresponds to a stacking fault when parallel to the basal plane or to an anti-phase defect when parallel to the $(10\bar{1}1)_{HCP}$ pyramidal plane, as shown in Fig. 5.5.4-b and c.

In Fig. 5.5.5 and 5.5.6 we report the histograms of the strain coefficients calculated. The histograms include only the atoms classified as HCP on the basis of the PTM analysis and for which $D^2 < D^2_{lim}$. The main values of these coefficients are reported in Tab. 5.3 and compared to the ones corresponding to the Bain strain. For calculating the Bain strains we used: $a_0 = 3.367$ Å, $a = 2.960$ Å and $c = 4.706$ Å. These lattice parameters values were calculated after the system has reached equilibrium at $T = 1400$ K and $T =$700 K. Using these lattice parameters,

we calculated the atomic volume V_a for the two phases as:

$$(V_a)_{BCC} = \frac{a_0^2}{2} = 17.968 \text{ Å} \tag{5.5.1}$$

$$(V_a)_{HCP} = \frac{\sqrt{3}a^2c}{4} = 17.854 \text{ Å} \tag{5.5.2}$$

This calculation clearly shows that the transformation mostly involves a change in shape of the lattice rather than a change in volume.

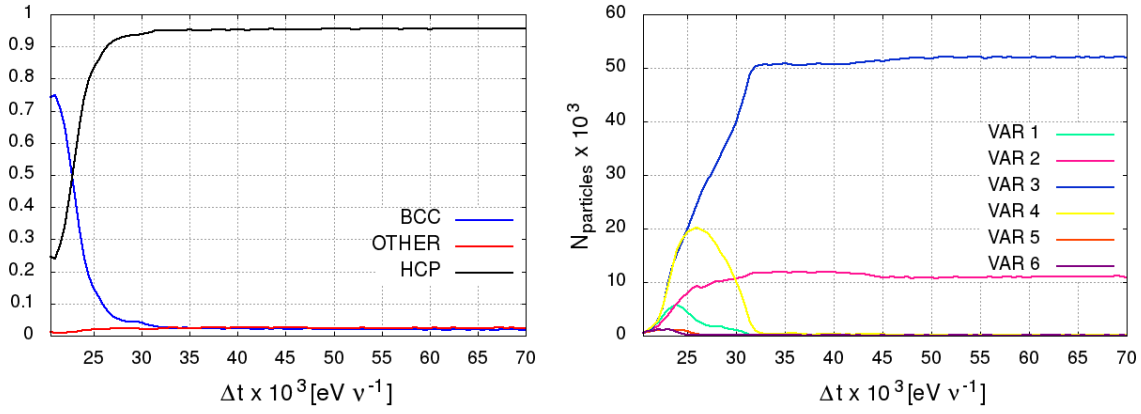

(a) (b)

Figure 5.5.1: *In the diagrams: a) evolution of the fractions of HCP and BCC phases; b) evolution of the number of atoms classified as belonging to a given variant. MD simulations in the (N**P**T) ensemble (P=0 Pa).*

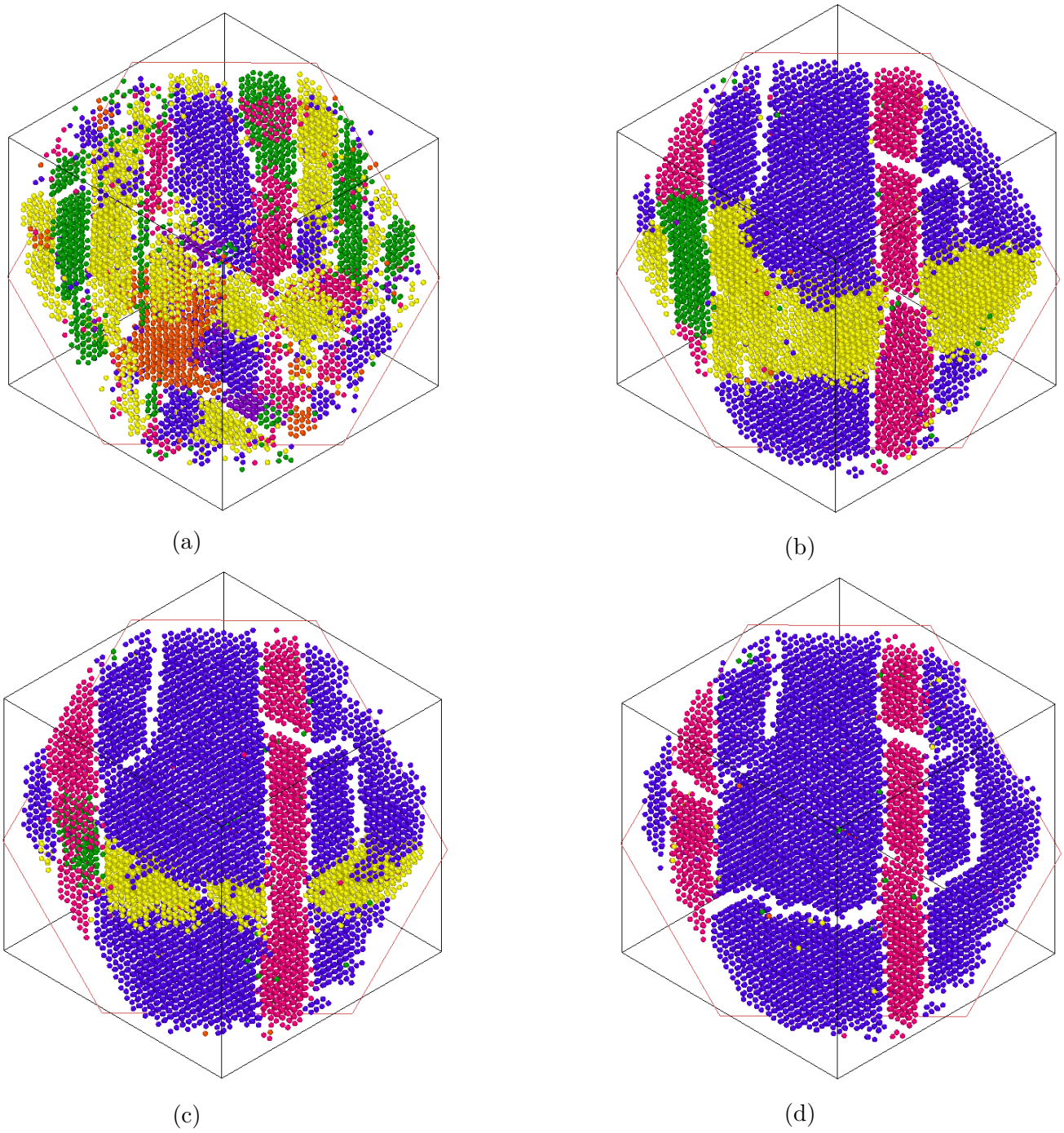

Figure 5.5.2: *A sequence of four snapshots taken during the transition in the (N**P**T) ensemble. Only atoms classified as HCP are shown and coloured on the basis of the variant to which they belong: a) small stable nuclei of the six variants when transition begins; b)-c) coarsening of the microstructure; d) final laminate microstructure with only two variants.*

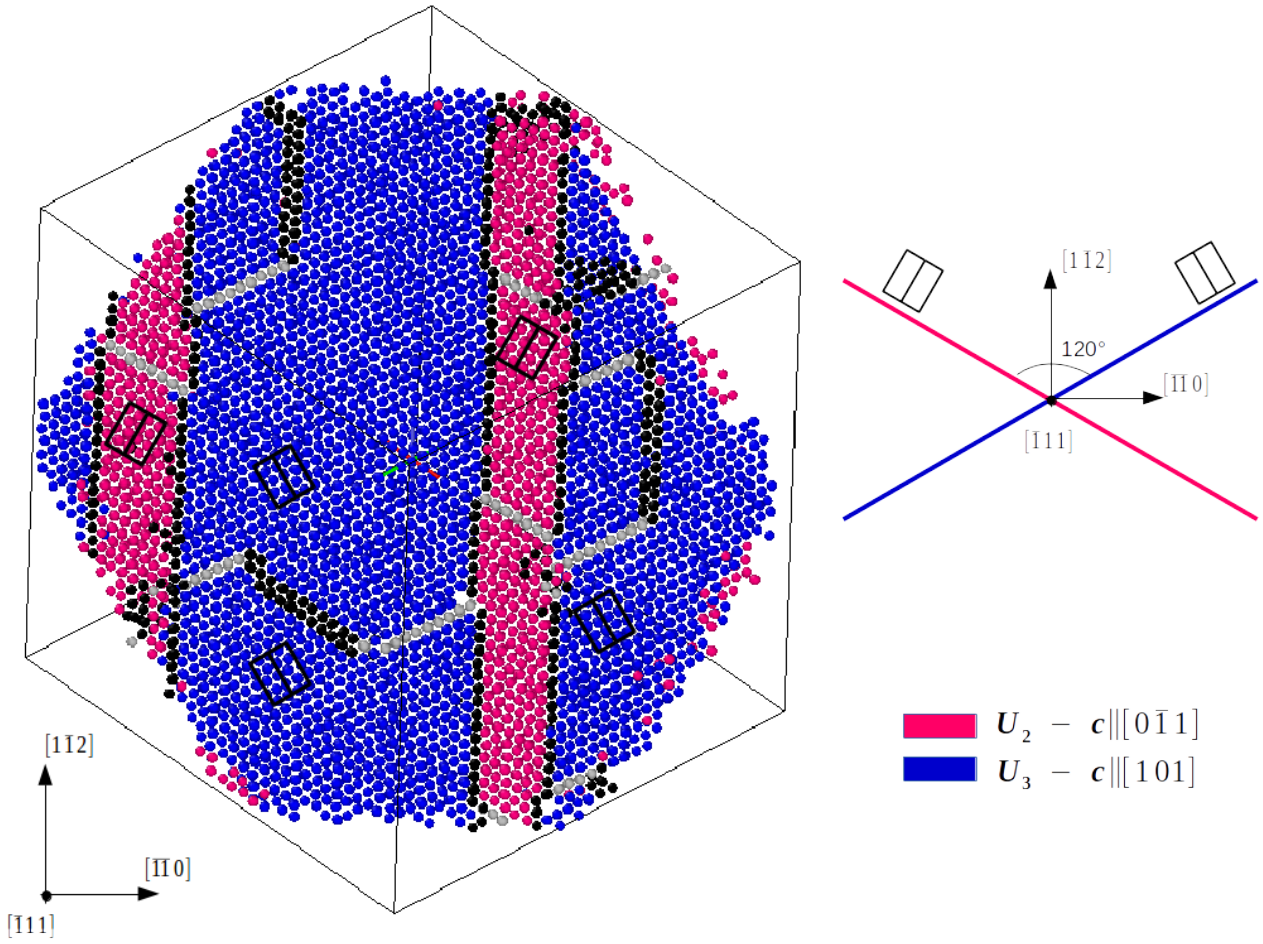

Figure 5.5.3: *Microstructure obtained at 700 K in the (N**P**T) ensemble (P=0 Pa). Atoms classified as HCP are coloured on the basis of the variant to which they belong, atoms classified as FCC (indicating a stacking fault) are coloured in grey, while atoms not classifiable in black. The orientation of the basal planes around the* $[\bar{1}11]$ *direction and the orientation of the* $\boldsymbol{c}$ *axis are reported on the left.*

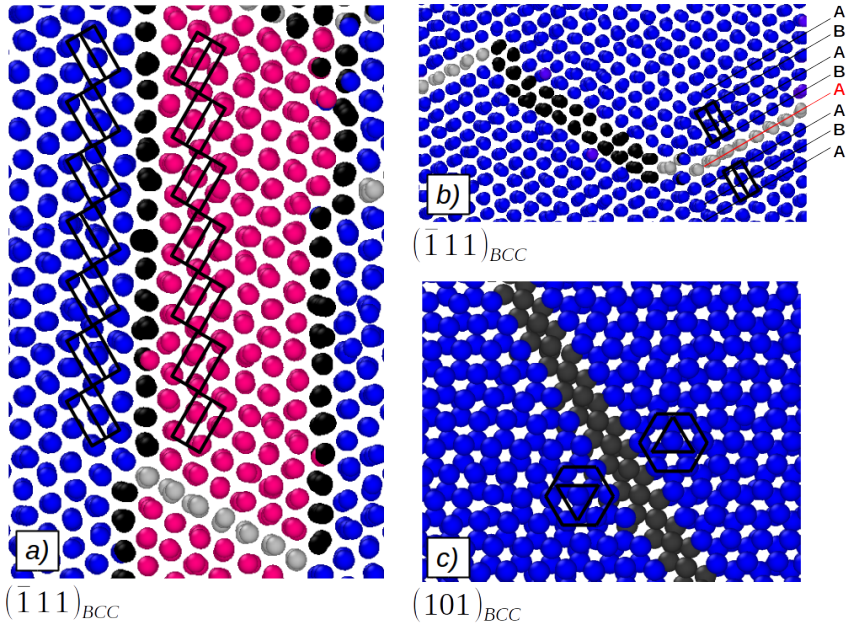

Figure 5.5.4: *a) atomic structure of the low energy* $(\bar{1}011)$ *boundary between variant 3 and 2; b) boundary between two domains with same Bain strain, corresponding to variant 3, but opposite shuffling direction. The interface between the anti-variants is composed by stacking faults (in grey) and antiphase defects (in black), which are shown more in detail c). Notice that the planes are referred to the original cubic frame.*

VARIANT 2						
	U_{11}	U_{22}	U_{33}	U_{12}	U_{13}	U_{23}
$\mathbf{U}_{num}$	0.893	1.023	1.030	0.003	0.002	0.033
$\mathbf{U}_{Bain}$	0.880	1.030	1.030	0.000	0.000	0.044
deviation [%]	1.47	-0.60	0.00	0.30	0.20	-25.00
VARIANT 3						
$\mathbf{U}_{num}$	1.028	0.0.885	1.030	0.002	-0.034	0.002
$\mathbf{U}_{Bain}$	1.030	0.880	1.030	0.000	-0.044	0.000
deviation [%]	-0.19	0.57	0.00	0.20	22.72	0.20

Table 5.3: *Mean values of the local strain coefficient numerically calculated compared with the Bain strain for the two variant selected in the simulations using the (N**P**T) ensemble (T=700 K, P= 0 Pa).*

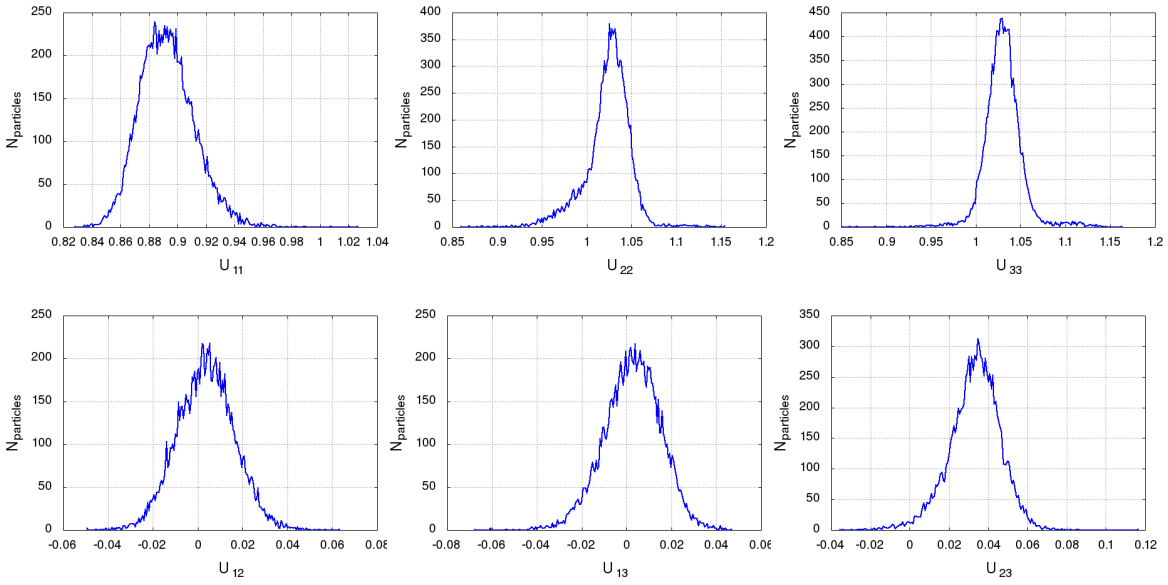

Figure 5.5.5: *The histograms of the Bain strain coefficients for variant 2 calculated for the simulation in the (N**P**T) ensemble (T=700 K, P=0 Pa).*

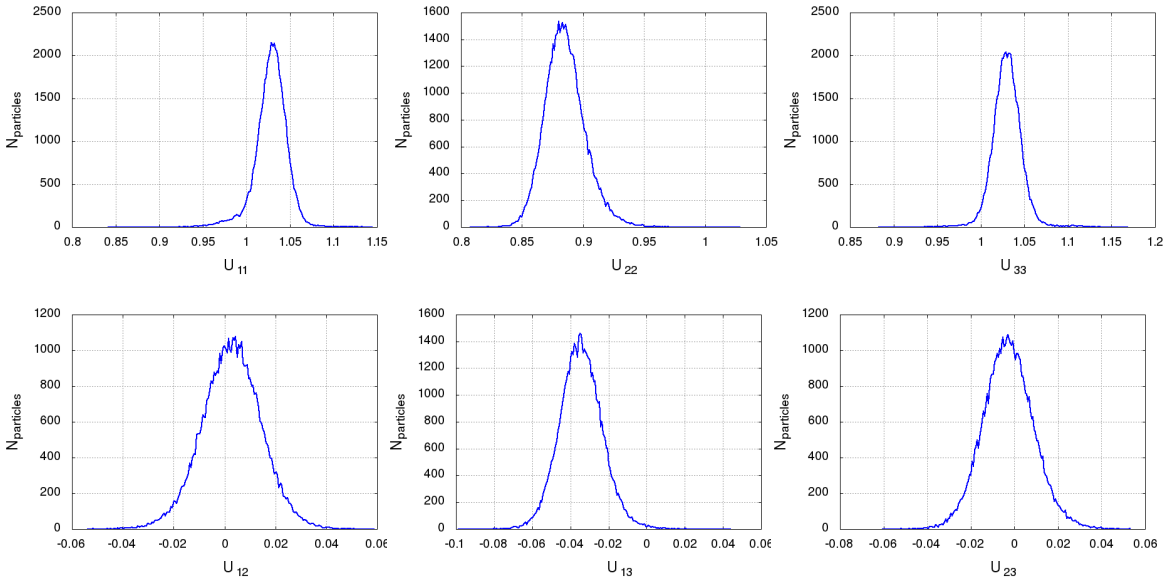

Figure 5.5.6: *The histograms of the Bain strain coefficients for variant 3 calculated for the simulation in the (N**P**T) ensemble (T=700 K, P=0 Pa).*

Constrained conditions (NVT ensemble)

A rather strong constraint is imposed to the system by preventing the simulation box to change its shape and volume. Its evolution is guided by the minimization of Helmoltz free energy. The microstructure evolution has been analysed by performing Langevin simulations in the (NVT) ensemble.

After quenching the system turns to an HCP structure and almost no BCC phase is left as for the case of unconfined conditions. We report in Fig. 5.5.7a the evolution of the BCC and HCP phase percentages during the transition (RMSD cutoff = 0.14). Differently from the unconstrained case, we can distinguish two regimes in these curves. When the system is quenched, the percentage of HCP phase grows to reach approximately the 85%. In this first step, its evolution is similar to the one in unconfined conditions. At this point there is still a 15% of BCC phase. In a second step, the HCP percentage increases to reach its final value of 95% and the BCC percentage further decreases. In Fig. 5.5.7b we report the evolution of the number of atoms classified as belonging to a given variant as a function of the time step ($D^2_{lim} = 6.5$, $N_n = 22$). As we can see, at the beginning of the transition there is a significant nucleation of all the six possible variants as in the unconfined case. This first phase coincides with the first part of the curves in Fig. 5.5.7a. Then, three of these variants start growing at the expense of the others and form the final microstructure. In the present case the selected variants are the triplet 2-4-6 (see Tab. 5.2). These variants share the $[111]_{BCC}$ direction in the parent phase so that it is easier to analyse the final microstructure by taking a slice orthogonal to this direction, as shown in Fig. 5.5.8.

The resulting microstructure is richer in interfaces than the one in unconfined conditions as it could be expected by the fact that a greater number of variants is present. The three variants organize themselves by forming several triple junctions involving only boundaries along the $\{10\bar{1}1\}_{HCP}$ planes. As shown by atomistic calculations [113], the $\{10\bar{1}1\}$ boundary has lower energy than the $\{11\bar{2}2\}$. Consequently, it is reasonable to expect that the system favours the formation of this type of boundaries. Some accommodation must be present to form this particular junction because these planes form an angle of 61.5° with the basal plane and not of 60° (see Fig. 5.5.9). In Fig. 5.5.10 four snapshots of the microstructural evolution are reported. In the figure we show only the atoms classified as HCP on the basis of the PTM analysis. The four snapshots are identified by stars along the HCP percentage curve in Fig. 5.5.7a. At the beginning, stable nuclei of all the six variants appear. Two triple junctions are already identifiable. This observation highlights the stability of these points and suggests that once formed they guide the overall textural evolution. While the transition proceed, all the different HCP domains develop. Later, the microstructure coarsens till only three variants remain. We repeated the simulation in the (NVT) ensemble several times by

changing the seed for the random noise. The evolution of the variants domains for four different simulations is reported in Fig. 5.5.11. From these diagrams, we can see that in all the cases the system behaves similarly and, after the nucleation of all the possible variants, progressively selects three variants with a similar volume fraction. In all the simulations, the selected triplets share a $[111]_{BCC}$ direction. In terms of microstructures, almost all the simulations performed show the selected triplet organizing around triple junctions. However, in some simulations we observed the co-existence of FCC domains with the HCP. One example of such a microstructure is shown in Fig. 5.5.12. In this case the selected triplet is the 2-4-5 (see Tab. 5.2). Variant 4 forms two laminates, consisting of parallel twins along the $(\bar{1}011)_{HCP}$ plane, with variant 2 and 5. These two laminates develop parallel to the two pyramidal planes of variant 4. At the crossing between variants 2 and 5, an FCC domain acts as a "buffer" by forming a coherent interface with both the basal planes along two $\langle 111\rangle_{FCC}$ planes which share the $[\bar{1}10]_{FCC}$ direction.

In Fig. 5.5.13, 5.5.14, 5.5.15 we report the histograms of the strain coefficients calculated for the three variants forming the microstructure in Fig. 5.5.8. The histograms include only the atoms classified as HCP on the basis of the PTM analysis and for which $D^2 < D^2_{lim}$. The main values of these coefficients are reported in Tab. 5.4 and compared to the ones corresponding to the Bain strain. For calculating the Bain strains we used: $a_0 = 3.30$ Å, $a = 2.960$ Å and $c = 4.706$ Å. These lattice parameters values were calculating after the system has reached equilibrium at $T = 1400$ K and $T = 700$ K and essentially do not differ from the ones calculated from simulations in the (N**P**T) ensemble.

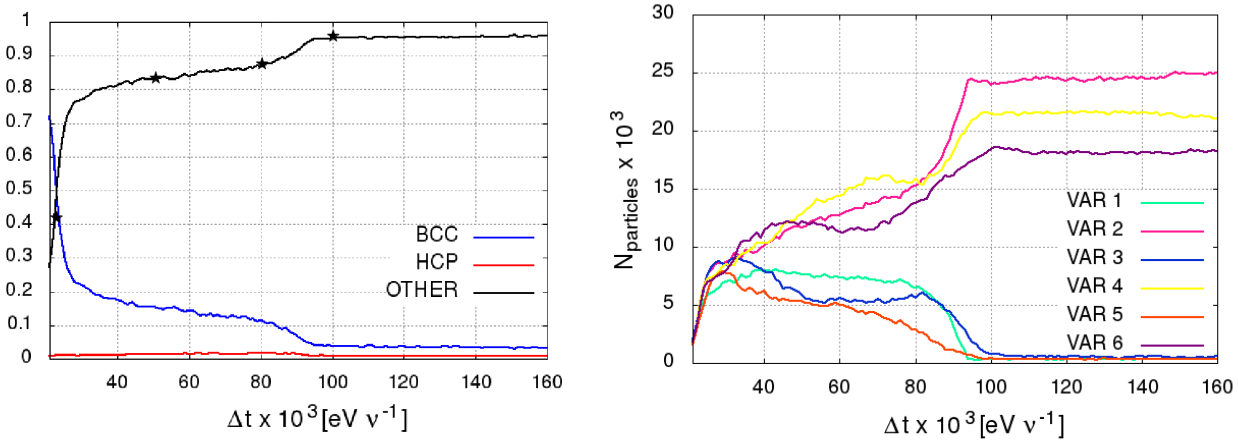

(a) (b)

Figure 5.5.7: *a) evolution of the fractions of HCP and BCC phases; b) evolution of the number of atoms classified as belonging to a given variant. Simulations in the (NVT) ensemble (constrained conditions).*

VARIANT 2						
	U_{11}	U_{22}	U_{33}	U_{12}	U_{13}	U_{23}
$\mathbf{U}_{num}$	0.918	1.046	1.038	-0.0145	-0.0158	0.0234
$\mathbf{U}_{Bain}$	0.897	1.053	1.053	0.000	0.000	0.045
deviation [%]	2.34	-0.66	-1.42	-1.45	-1.58	-48.00
VARIANT 4						
$\mathbf{U}_{num}$	1.049	0.916	1.039	-0.0152	0.0243	-0.0169
$\mathbf{U}_{Bain}$	1.053	0.897	1.053	0.000	0.045	0.000
deviation [%]	-0.38	2.11	-1.33	-1.52	-46.00	-1.70
VARIANT 6						
$\mathbf{U}_{num}$	1.051	1.041	0.913	0.0262	-0.0165	-0.187
$\mathbf{U}_{Bain}$	1.053	1.053	0.897	0.045	0.000	0.000
deviation [%]	-0.20	-1.14	1.78	-41.77	-1.65	-1.87

Table 5.4: *Mean values of the local strain coefficient numerically calculated compared with the Bain strain for the three variant selected in constrained conditions (NVT simulation).*

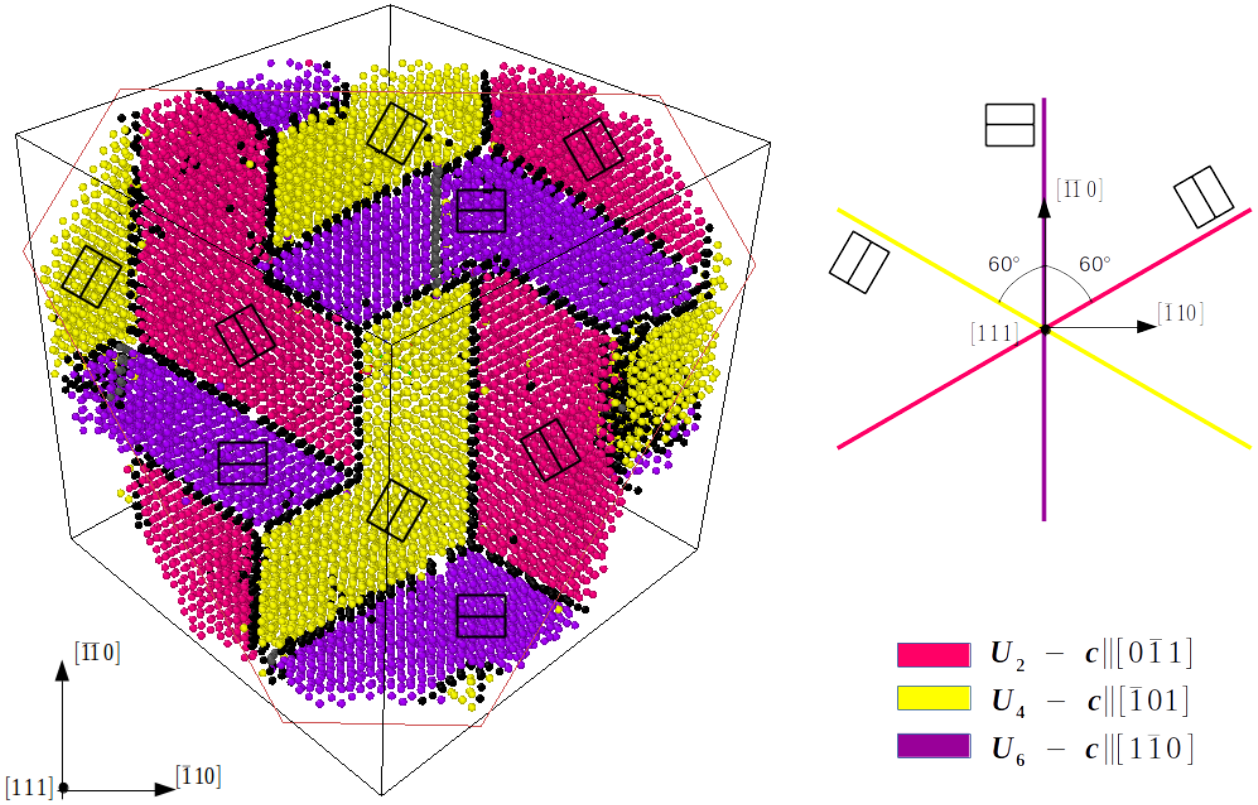

Figure 5.5.8: *Microstructure obtained at 700 K in the (NVT) ensemble. Atoms classified as HCP are coloured on the basis of the variant to which they belong while atoms not classifiable are coloured in black. The orientation of the basal planes around the* [111] *direction and the orientation of the* **c** *axis are listed on the left.*

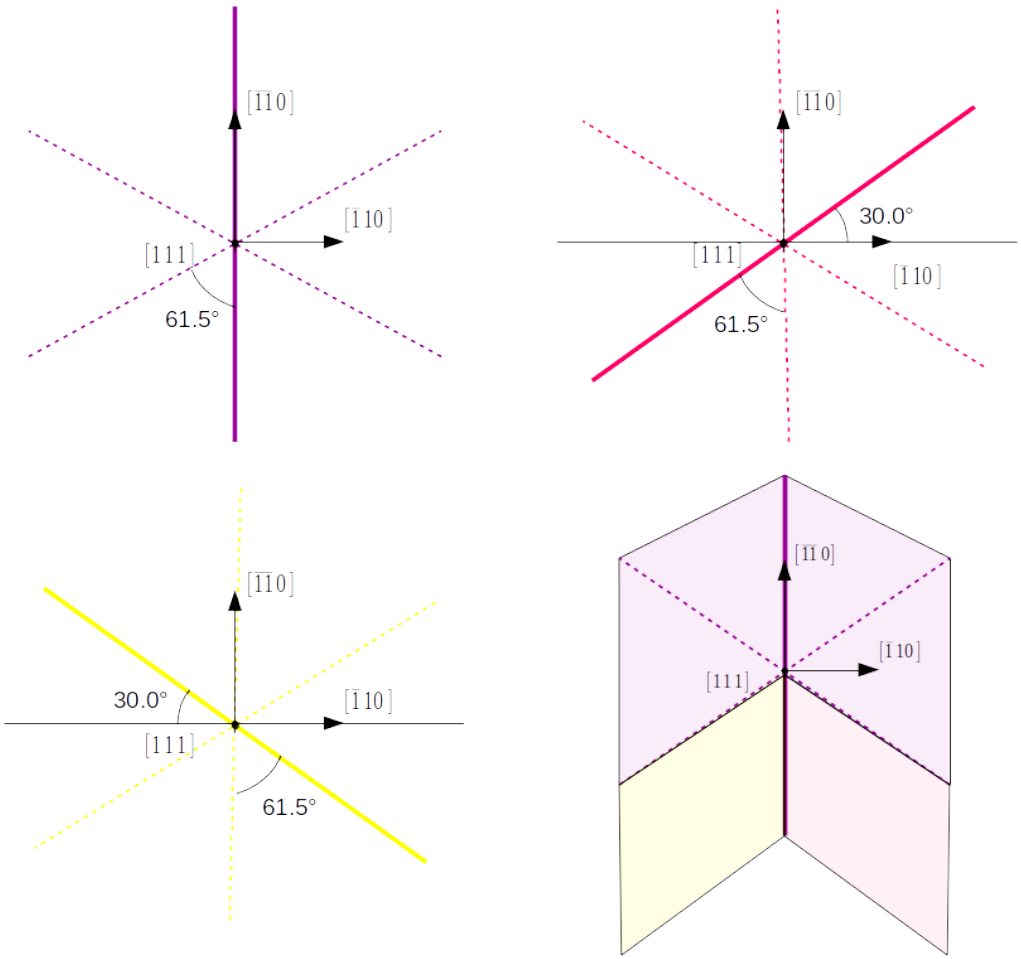

Figure 5.5.9: *Three variants sharing a common* [111] *direction have the basal planes relatively rotated of* 60° *degrees around this axis. This misorientation is close to the* 61.5° *symmetric tilt boundary along the* $\{10\bar{1}1\}$ *pyramidal plane. Actually, with little accommodation, the three variants can form a triple junction.*

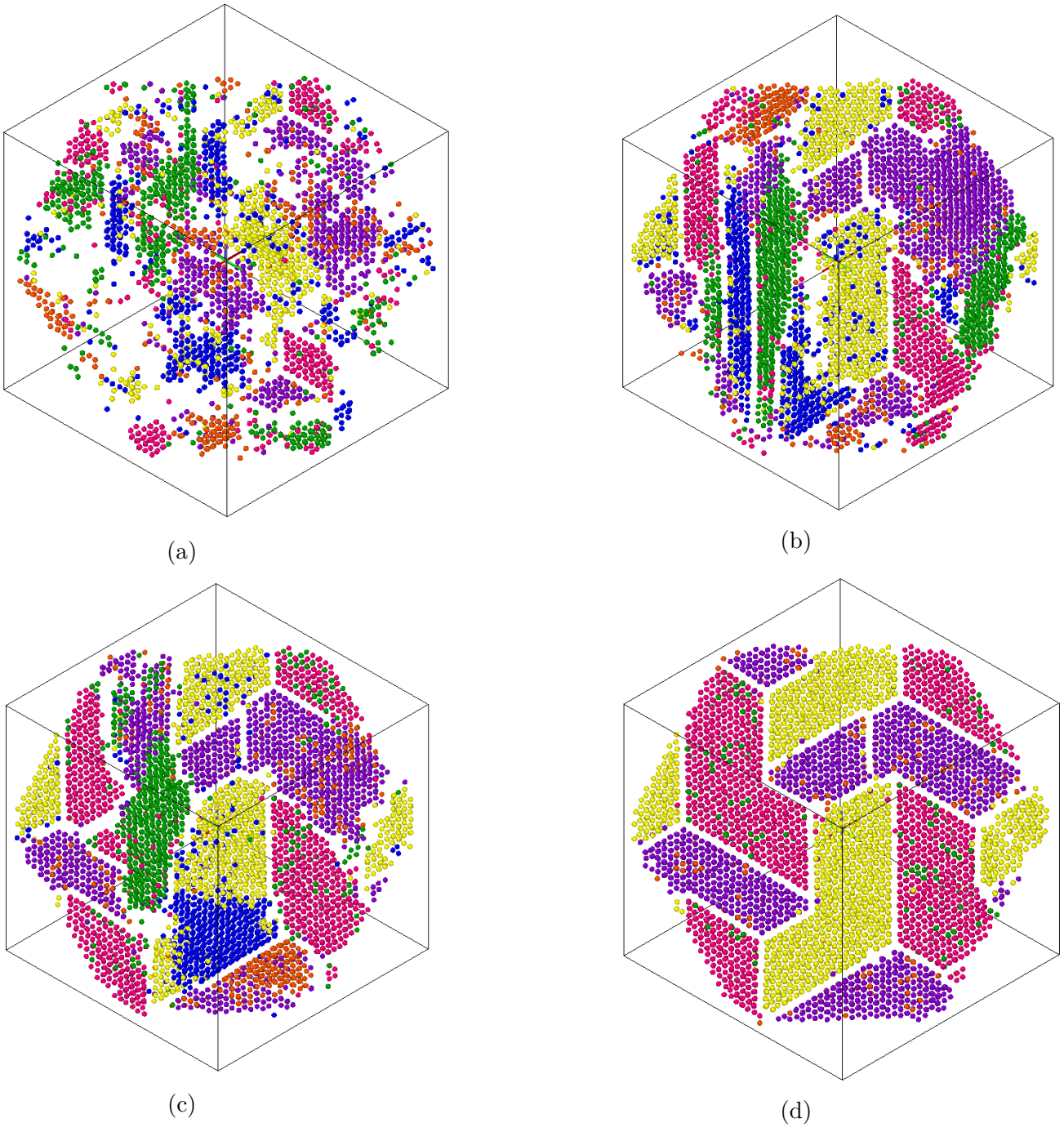

Figure 5.5.10: *A sequence of four snapshots taken during the transition in the (NVT) ensemble. Only atoms classified as HCP are shown and coloured on the basis of the variant to which they belong: a) small stable nuclei of the six variants when transition begins. Two triple junctions are already identifiable; b) growth of the HCP nuclei; c) coarsening of the microstructure after almost all of the BCC phase has disappeared; d) final microstructure with only three of the six variants initially nucleated.*

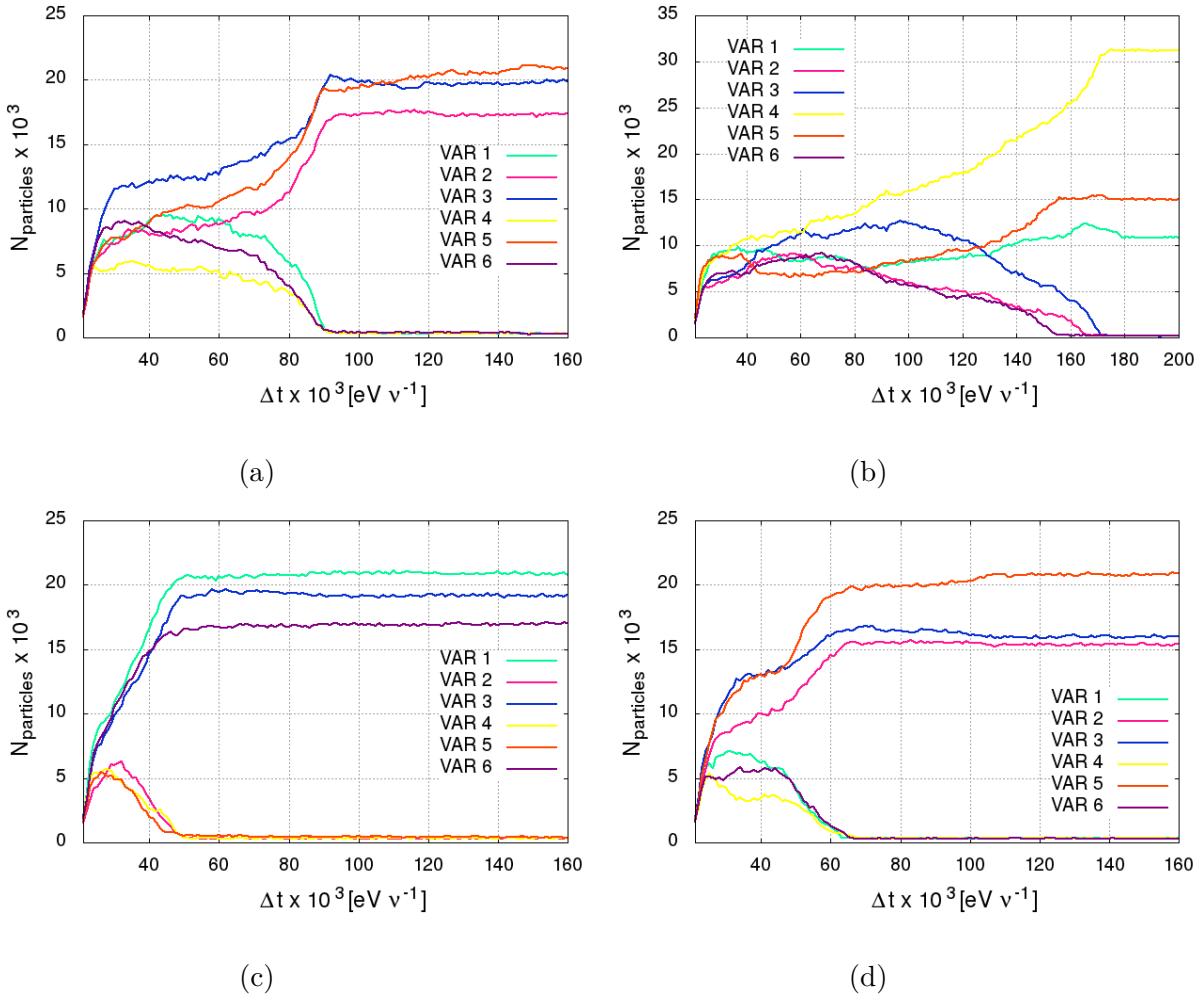

Figure 5.5.11: *Evolution of the number of atoms belonging to a given variant in function of the time step for four simulations in the (NVT) ensemble where the noise terms have been changed.*

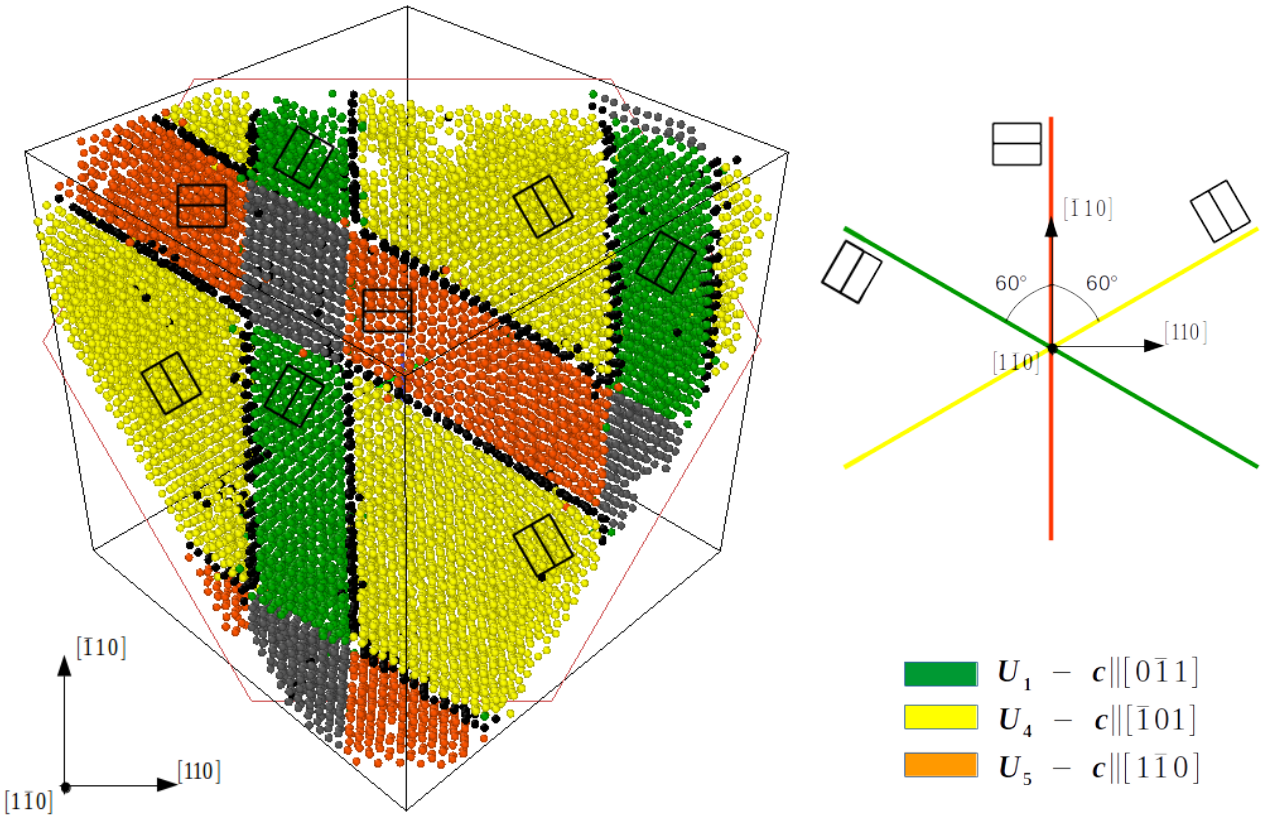

Figure 5.5.12: *Microstructure obtained at 700 K in the (NVT) ensemble with FCC domains. Atoms classified as HCP are coloured on the basis of the variant to which they belong, atoms classified as FCC are coloured in grey while atoms not classifiable are coloured in black. The orientation of the basal planes around the* [111] *direction and the orientation of the* **c** *axis are listed on the left.*

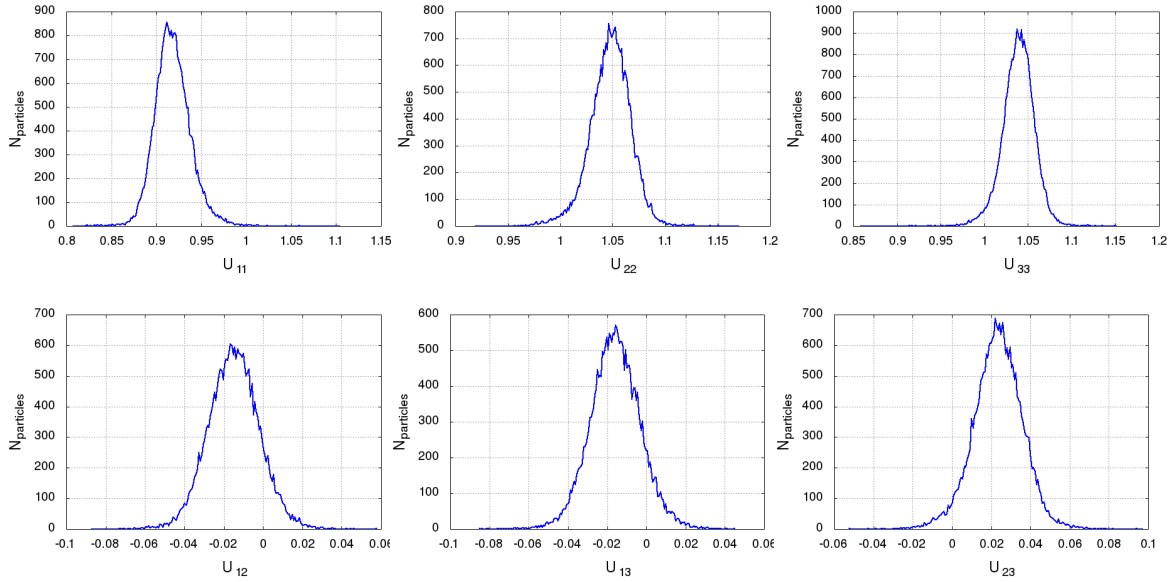

Figure 5.5.13: *The histograms of the Bain strain coefficients for variant 2 (microstructure of Fig. 5.5.8) calculated for the simulation in the (NVT) ensemble at 700 K.*

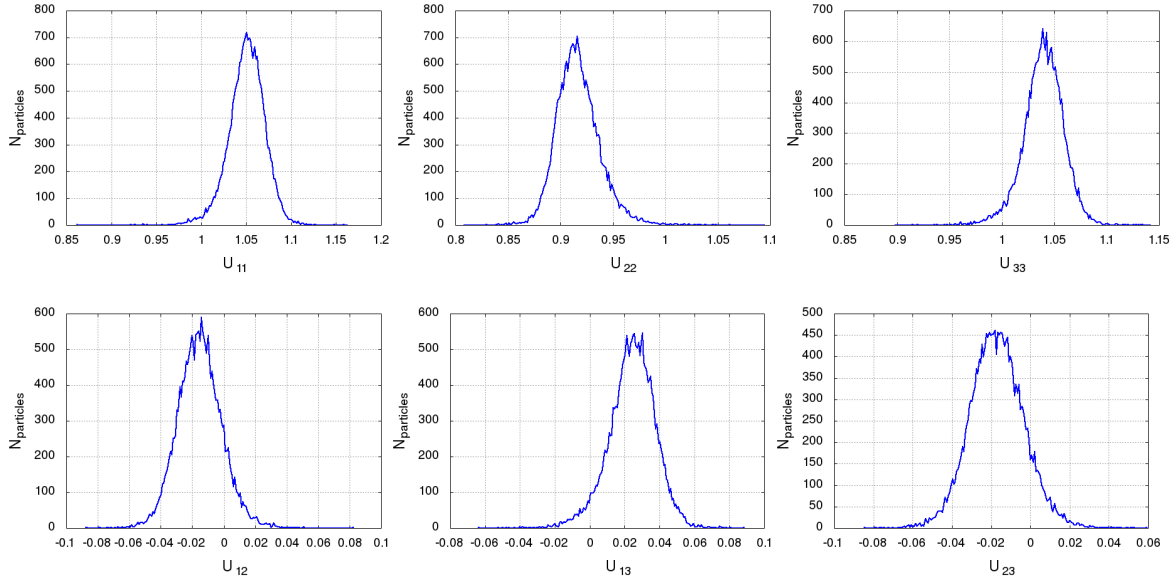

Figure 5.5.14: *The histograms of the Bain strain coefficients for variant 4 (microstructure of Fig. 5.5.8) calculated for the simulation in the (NVT) ensemble at 700 K.*

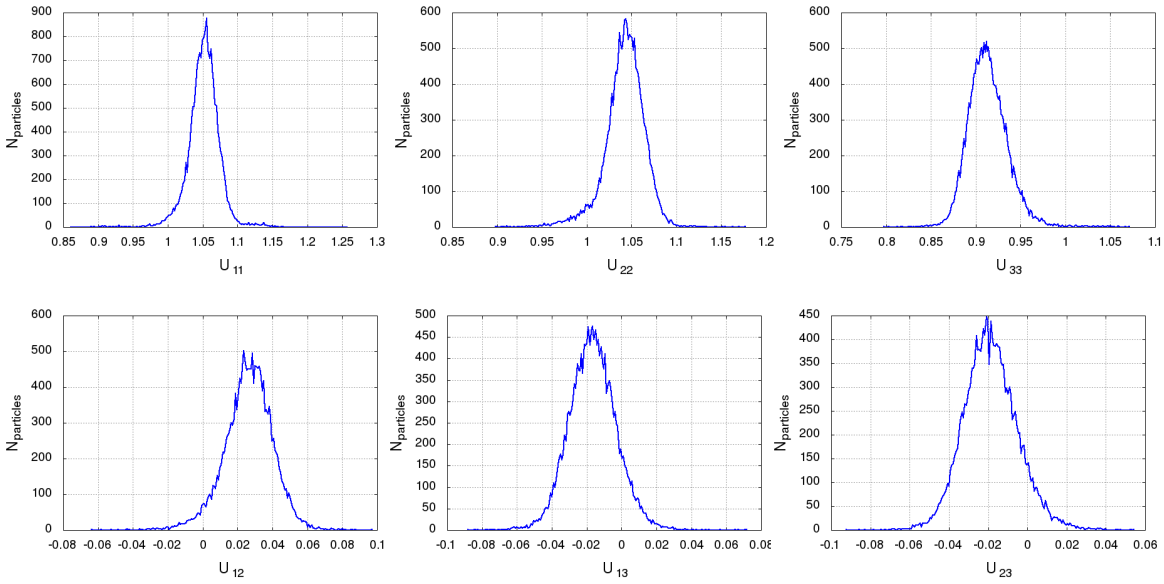

Figure 5.5.15: *The histograms of the Bain strain coefficients for variant 6 (microstructure of Fig. 5.5.8) calculated for the simulation in the (NVT) ensemble at T=700 K.*

5.6 Discussion

From the results of simulations in the (N**P**T) ensemble (section 5.5.2) and in the (NVT) ensemble (section 5.5.2), the deep influence of local mechanical constraints in the final microstructural morphology clearly emerges. Our observations can be summarized in the following points:

- the transition principally implies a change in shape with negligible change in volume;
- in absence of mechanical constraints, the system forms a laminate microstructure of parallel twins along the low energy boundary $\{10\bar{1}1\}$;
- the presence of a mechanical constraint, which prevents the change in shape and volume of the surroundings, induces the selection of three between the six possible variants with a common $\langle 111 \rangle_{BCC}$ direction in the parent phase;
- several simulations performed reveal that the selected variants have the tendency of self-organizing by forming triple junctions consisting of low energy $\{10\bar{1}1\}$ boundaries.

The selection of a triplet of variants is explicable in terms of self-accommodation. The strain induced in the surroundings by a given triplet can be estimated as

the average of the three associated Bain strain. By taking the lattice parameters values calculated from simulations, this calculation gives:

$$\bar{\mathbf{U}} = \frac{1}{2}\begin{pmatrix} \eta_2+\eta_3+2\eta_1 & \pm 1/3(\eta_3-\eta_2) & \pm 1/3(\eta_3-\eta_2) \\ \pm 1/3(\eta_3-\eta_2) & \eta_3+\eta_2+2\eta_1 & \pm 1/3(\eta_3-\eta_2) \\ \pm 1/3(\eta_3-\eta_2) & \pm 1/3(\eta_3-\eta_2) & 2\eta_1+\eta_3+\eta_2 \end{pmatrix} \tag{5.6.1}$$

$$= \begin{pmatrix} 0.986 & \pm 0.015 & \pm 0.015 \\ \pm 0.015 & 0.986 & \pm 0.015 \\ \pm 0.015 & \pm 0.015 & 0.986 \end{pmatrix} \tag{5.6.2}$$

where the plus or minus sign of the off-diagonal coefficients depends on the selected triplet. The average strain $\bar{\mathbf{U}}$ clearly approach the identity matrix so the variant selection in our simulation can be reasonabbly justified in terms of a self-accomodation criterion [114, 109].

Our observations are consistent with the experimental one reported in [4] for zirconium alloys. In the paper, the authors highlight the presence of three characteristic plate morphologies resulting from the martensitic transformation:

- large internally twinned plates arranged in a triangular morphology, referred in the paper as *primary plates* (Fig. 5.6.1a and 5.6.1b);
- smaller 3-plate clusters located in the volume enclosed by the primary plates, referred in the paper as *secondary plates* (Fig. 5.6.1c);
- packets of martensite laths arranged parallely (Fig. 5.6.1d).

Moreover, the authors suggested the following growth sequence:

- formation of large primary martensite plates internally twinned;
- transformation of the volume included between primary plates into secondary plates clusters.

This dynamics suggests a nucleation of secondary plates in conditions where self-accommodation plays an important role in dictating the martensite plates arrangement because the change in shape and volume of the surrounding matrix is limited. A micrography of the secondary plates around the $[111]_{BCC}$ is shown in Fig. 5.6.2. The three variants A-B-C which compose the cluster correspond to variants 6-4-2 in Tab. 5.2. They share a $\langle 11\bar{2}0\rangle_{HCP}$ dense direction and are related by $\{10\bar{1}1\}$ twins. This geometry strictly corresponds with the results of our simulations in the (NVT) ensemble i.e. in constrained conditions. The presence of clusters of three variants related by $\{10\bar{1}1\}$ twins has been documented and related to self-accommodation also in recent experimental works on Ni-Ti shape memory alloys [110].

We discuss now the strain numerically calculated from simulations. We can observe that for the simulations in the (N**P**T) ensemble the numerical strain is in agreement with the Bain distortion. The greatest deviation is seen in the non-zero off-diagonal coefficient and can be justified by the fact that these coefficients are really small so they are more difficult to accurately calculate. This is coherent with the fact that, in this case, the system forms a laminate of parallel twins and the elastic strain of a periodic structure of parallel coherent interfaces is zero. On the other side, for the simulations in the (NVT) ensemble the deviation of the numerical strain from the Bain strain is much higher (see Tab. 5.4) and differs also of one order of magnitude from the case in the (N**P**T) ensemble. This is particularly evident for the off-diagonal coefficients. In this case, boundary conditions prevent the system by forming a mono-variant or laminate structure with zero elastic energy. Thanks to the negligible volume change involved in the BCC→HCP transition, the system can select a specific triplet of variants in order to form a microstructure which minimizes the elastic strain energy. However, as pointed out by the deviation of the numerically calculated strain from the ideal Bain strain, this microstructure presents some residual strain.

We want to highlight a last point regarding the microstructures obtained in constrained conditions. Occasionally, we observed the three variants forming two laminates with"buffer" FCC domains at the crossing. The presence of FCC phase after transition has little experimental evidence [115]. On the other side, it has been already documented in previous numerical works [76, 78, 80] and related to the impossibility of forming a "coherent" triple junction between three variants sharing a $(11\bar{2}0)_{HCP}$ direction. Our simulations show that in presence of mechanical constraints the self-organization of variants around triple junctions is possible and seems strongly favoured with respect to an arrangement involving the presence of FCC phase.

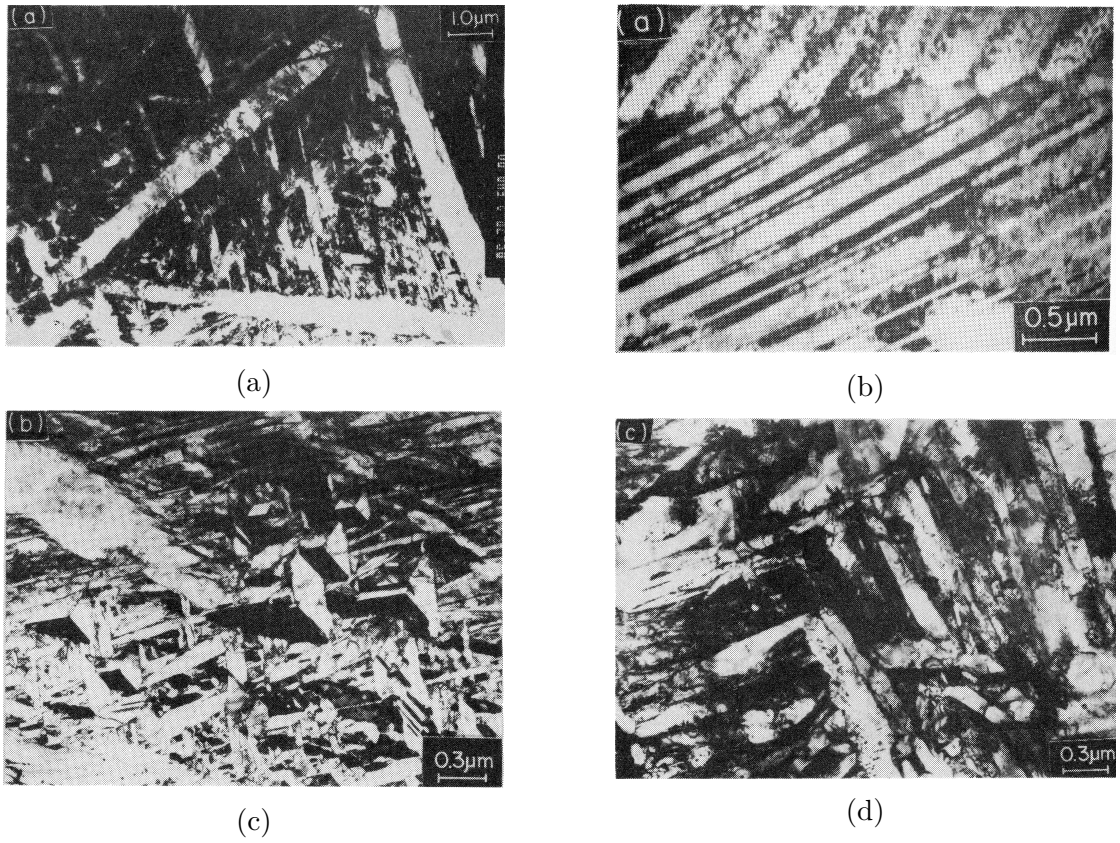

Figure 5.6.1: *TEM micrograph showing the martensite morphology obtained in Zr-2.5wt%Nb alloy: a) large primary plates (micrometer length scale) internally twinned as shown in the detailed b); c) secondary plates consisting in a 3-variants cluster (sub-micrometer length scale); d) packets of parallely stacked laths. Images from [4].*

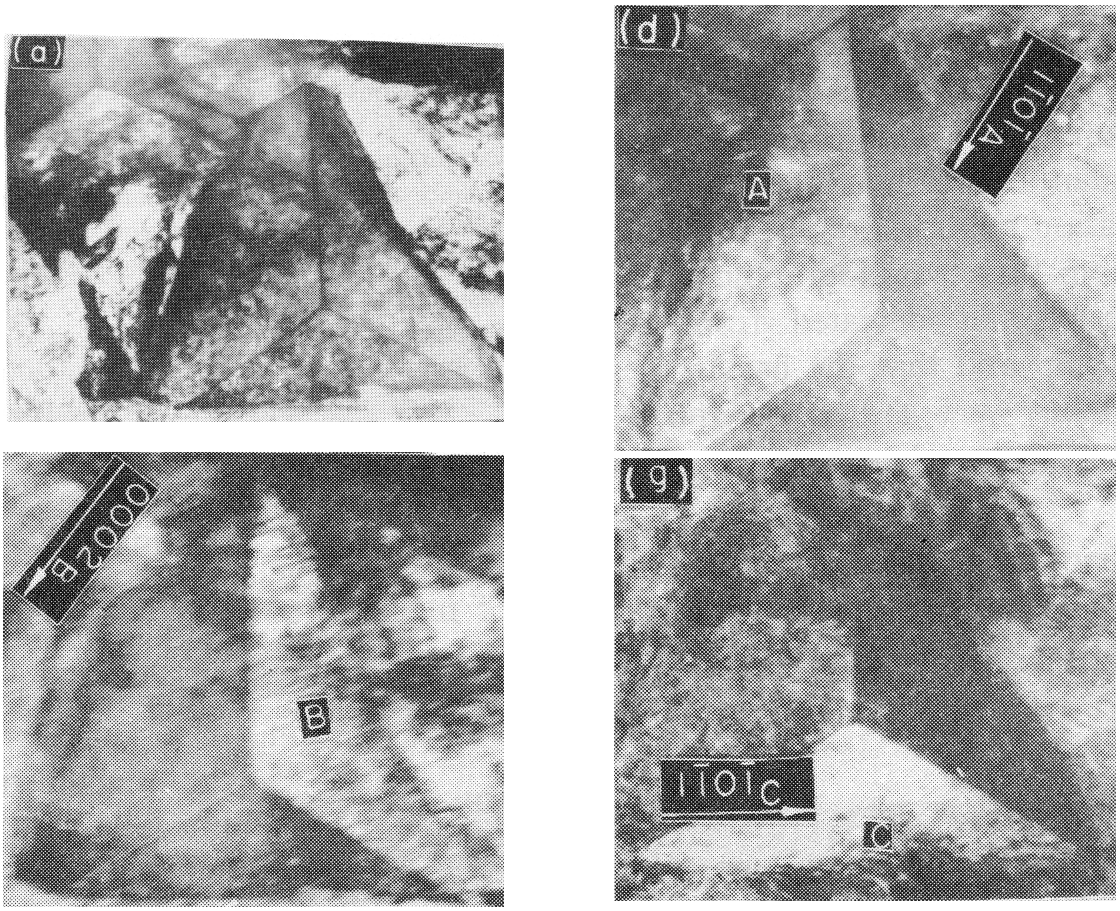

Figure 5.6.2: *TEM micrograph of a representative secondary plate composed by three variants, labelled A,B and C. Images from [4].*

Chapter 6

Conclusions and perspectives

The present work consisted in the development and application of a novel method for the atomistic study of crystalline materials. The method uses a first order in time stochastic dynamics in order to overcome the time scale limit associated with crystalline vibrations which characterizes current modelling techniques such as Molecular Dynamics. We formalized equations in the (NVT) as well as in the (N**P**T) thermodynamic ensembles. Finally, we gave an heuristic justification of the hypothesis at the basis of this formalism i.e. the presence of a time-scale separation between slow evolving DOFs (position variables) and fast evolving DOFs (momenta variables).

The model was implemented in a Fortran code of our own within a spline-formulated many-body potential. Different numerical schemes were tested for the time integration of stochastic differential equations within different search algorithms for the computation of interatomic forces.

Two applications of the model proposed were done.

The first application consisted in the study of curvature induced grain boundary motion. For this purpose, we considered the shrinking of a 2D circular island grain embedded in a monocrystalline matrix. We performed simulations with the Langevin dynamics as well as with Molecular Dynamics. We then compared the results in terms of evolution of two observables characterizing the phenomenon i.e. the misorientation of the grain and the number of defects along the boundary. The agreement between the two methods confirmed the applicability of our theory for the study of crystalline materials. After this validation, we investigated the migration mechanisms acting at the atomic scale for the high and low misorientation cases. For angles between 0° and 10° we verified that the grain boundary motion results from a combination of dislocation glide, reaction and annihilation. A toy model has been proposed to illustrate this mechanism. For the particular

high misorientation angle 38.2°, which corresponds to a coincidence site lattice Σ7, we verified that the boundary migration proceeds by local readjustment of atomic positions around atoms on coincidence sites. The fact that these atoms act as "fixed points" prevents any rotation of the embedded grain.

The second application has consisted in the study of the temperature induced $\beta \rightarrow \alpha$ phase transition in pure titanium, with particular focus on the effect of local mechanical constraints. For this purpose, we performed simulations in the (N**P**T) and (NVT) thermodynamical ensembles thus allowing/preventing a free change in shape of the simulation box. Our study highlighted that mechanical constraints have a strong influence on the final morphology of martensite and on variant selectivity. In particular, our simulations show that, in confined conditions, three between the six possible variants are selected. This selectivity is related to the minimization, on average, of the overall strain. The microstructures obtained are characterized by several triple junctions around which the selected variants organize by forming low energy $\{10\bar{1}1\}$ boundaries. These results are coherent with previous experimental observations in zirconium alloys and in Ni-Ti shape memory alloys.

Future perspectives are multiple and involve different aspects of the present work.

From the theoretical point of view, the passage from the deterministic Newton dynamics to the overdamped Langevin dynamics is still to be formalized. This operation would need a deeper analysis of the position and momenta autocorrelation functions in order to identify a suitable time span over which averaging the fast evolving degrees of freedom. This procedure is expected to lead to a time coarse-grained interatomic potential and to an explicit definition of the viscosity parameters, i.e. of the time scale characterizing equations.

In the framework of grain boundary migration and coupled motion, it would be of interest to further investigate the atomic mechanisms of migration for high misorientation angles corresponding to different coincidence site lattices in order to make a comparison with the "ideal" behaviour of the $\Sigma 7 - 38.2°$. Accordingly to the analysis in terms of dichromatic pattern for the high misorientation case, another fascinating perspective is the analysis of the grain boundary migration for the low misorientation case by the use of the 0-lattice theory. Linking the mechanisms acting at the atomic scale to purely geometrical features of a given boundary would be of strong interest to develop simple models of migration and in terms of grain boundary engineering.

In the framework of the $\beta \rightarrow \alpha$ phase transition in titanium, the study performed highlighted the deep influence of mechanical constraints on microstructural morphology during the martensitic phase transition. In this field, further inves-

tigations should be done by varying the level and typology of constraint applied to the simulation box. Another important study that should be done is the influence of possible thermal cycling in defects generation and accumulation. Finally, an intriguing field of research, which would combine the two topics addressed in this thesis, would be the analysis of interface influence in martensite nucleation, e.g. verifying the possible preference of martensite to nucleate at low/high angle tilt/twist grain boundaries and/or triple junctions.

Bibliography

[1] R. W. Balluffi, S. Allen, and W. C. Carter, *Kinetics of materials*. John Wiley & Sons, 2005.

[2] D. A. Young, *Phase diagrams of the elements*. Univ of California Press, 1991.

[3] S. Banerjee and P. Mukhopadhyay, *Phase transformations: examples from titanium and zirconium alloys*. Elsevier, 2010, vol. 12.

[4] D. Srivastava, K. Madangopal, S. Banerjee, and S. Ranganathan, "Self accomodation morphology of martensite variants in zr 2.5 wt% nb alloy," *Acta metallurgica et materialia*, vol. 41, no. 12, pp. 3445–3454, 1993.

[5] G. Lütjering and J. C. Williams, *Titanium*. Springer Science & Business Media, 2007.

[6] D. A. Molodov, *Microstructural design of advanced engineering materials*. John Wiley & Sons, 2013.

[7] F. Roters, P. Eisenlohr, L. Hantcherli, D. D. Tjahjanto, T. R. Bieler, and D. Raabe, "Overview of constitutive laws, kinematics, homogenization and multiscale methods in crystal plasticity finite-element modeling: Theory, experiments, applications," *Acta Materialia*, vol. 58, no. 4, pp. 1152–1211, 2010.

[8] A. Finel, Y. Le Bouar, A. Gaubert, and U. Salman, "Phase field methods: Microstructures, mechanical properties and complexity," *Comptes Rendus Physique*, vol. 11, no. 3-4, pp. 245–256, 2010.

[9] M. A. Miodownik, "A review of microstructural computer models used to simulate grain growth and recrystallisation in aluminium alloys," *Journal of Light Metals*, vol. 2, no. 3, pp. 125–135, 2002.

[10] B. Devincre and L. Kubin, "Mesoscopic simulations of dislocations and plasticity," *Materials Science and Engineering: A*, vol. 234, pp. 8–14, 1997.

[11] E. B. Tadmor and R. E. Miller, *Modeling materials: continuum, atomistic and multiscale techniques.* Cambridge University Press, 2011.

[12] M. S. Daw and M. I. Baskes, "Embedded-atom method: Derivation and application to impurities, surfaces, and other defects in metals," *Physical Review B*, vol. 29, no. 12, p. 6443, 1984.

[13] M. Baskes, "Modified embedded-atom potentials for cubic materials and impurities," *Physical review B*, vol. 46, no. 5, p. 2727, 1992.

[14] A. F. Voter, "Hyperdynamics: Accelerated molecular dynamics of infrequent events," *Physical Review Letters*, vol. 78, no. 20, p. 3908, 1997.

[15] A. Laio and M. Parrinello, "Escaping free-energy minima," *Proceedings of the National Academy of Sciences*, vol. 99, no. 20, pp. 12 562–12 566, 2002.

[16] K. Elder, M. Katakowski, M. Haataja, and M. Grant, "Modeling elasticity in crystal growth," *Physical review letters*, vol. 88, no. 24, p. 245701, 2002.

[17] A. B. Bortz, M. H. Kalos, and J. L. Lebowitz, "A new algorithm for monte carlo simulation of ising spin systems," *Journal of Computational Physics*, vol. 17, no. 1, pp. 10–18, 1975.

[18] S. Yip, *Handbook of materials modeling.* Springer Science & Business Media, 2007.

[19] F. El-Mellouhi, N. Mousseau, and L. J. Lewis, "Kinetic activation-relaxation technique: An off-lattice self-learning kinetic monte carlo algorithm," *Physical Review B*, vol. 78, no. 15, p. 153202, 2008.

[20] L. K. Béland, P. Brommer, F. El-Mellouhi, J.-F. Joly, and N. Mousseau, "Kinetic activation-relaxation technique," *Physical Review E*, vol. 84, no. 4, p. 046704, 2011.

[21] N. G. Van Kampen, *Stochastic processes in physics and chemistry.* Elsevier, 1992, vol. 1.

[22] M. Parrinello and A. Rahman, "Polymorphic transitions in single crystals: A new molecular dynamics method," *Journal of Applied physics*, vol. 52, no. 12, pp. 7182–7190, 1981.

[23] J. H. Jeans, *The dynamical theory of gases.* University Press, 1921.

[24] D. Pigozzi, *Appunti di meccanica razionale.* Progetto, 2009.

[25] B. Diu, B. Roulet, C. Guthmann, and D. Lederer, *Eléments de physique statistique*. Hermann, 1989.

[26] D. Tsai, "The virial theorem and stress calculation in molecular dynamics," *The Journal of Chemical Physics*, vol. 70, no. 3, pp. 1375–1382, 1979.

[27] R. J. Swenson, "Comments on virial theorems for bounded systems," *American Journal of Physics*, vol. 51, no. 10, pp. 940–942, 1983.

[28] M. J. Louwerse and E. J. Baerends, "Calculation of pressure in case of periodic boundary conditions," *Chemical physics letters*, vol. 421, no. 1-3, pp. 138–141, 2006.

[29] R. Toral and P. Colet, *Stochastic numerical methods: an introduction for students and scientists*. John Wiley & Sons, 2014.

[30] Z. Schuss, *Theory and applications of stochastic processes: an analytical approach*. Springer Science & Business Media, 2009, vol. 170.

[31] Q. Bronchart, Y. Le Bouar, and A. Finel, "New coarse-grained derivation of a phase field model for precipitation," *Physical review letters*, vol. 100, no. 1, p. 015702, 2008.

[32] K. Ito, "K. itô, proc. imp. acad.(tokyo) 20, 519 (1944)." in *Proc. Imp. Acad.(Tokyo)*, vol. 20, 1944, p. 519.

[33] R. Stratonovich, "A new representation for stochastic integrals and equations," *SIAM Journal on Control*, vol. 4, no. 2, pp. 362–371, 1966.

[34] P. Kloeden and E. Platen, "Numerical methods for stochastic differential equations," *Stochastic Hydrology and Hydraulics*, vol. 5, no. 2, pp. 172–172, 1991.

[35] L. Verlet, "Computer" experiments" on classical fluids. i. thermodynamical properties of lennard-jones molecules," *Physical review*, vol. 159, no. 1, p. 98, 1967.

[36] R. Hockney, S. Goel, and J. Eastwood, "Quiet high-resolution computer models of a plasma," *Journal of Computational Physics*, vol. 14, no. 2, pp. 148–158, 1974.

[37] A. Rollett, F. Humphreys, G. S. Rohrer, and M. Hatherly, *Recrystallization and related annealing phenomena*. Elsevier, 2004.

[38] L. Priester, *Grain boundaries: from theory to engineering.* Springer Science & Business Media, 2012, vol. 172.

[39] J. Burgers, "Geometrical considerations concerning the structural irregularities to be assumed in a crystal," *Proceedings of the Physical Society*, vol. 52, no. 1, p. 23, 1940.

[40] F. Frank, "Report of the symposium on the plastic deformation of crystalline solids," *Carnegie Institute of Technology, Pittsburgh*, pp. 150–154, 1950.

[41] B. Bilby, R. Bullough, and E. Smith, "Continuous distributions of dislocations: a new application of the methods of non-riemannian geometry," *Proc. R. Soc. Lond. A*, vol. 231, no. 1185, pp. 263–273, 1955.

[42] G. Gottstein and L. S. Shvindlerman, *Grain boundary migration in metals: thermodynamics, kinetics, applications.* CRC press, 2009.

[43] D. Gianola, S. Van Petegem, M. Legros, S. Brandstetter, H. Van Swygenhoven, and K. Hemker, "Stress-assisted discontinuous grain growth and its effect on the deformation behavior of nanocrystalline aluminum thin films," *Acta Materialia*, vol. 54, no. 8, pp. 2253–2263, 2006.

[44] K. Harris, V. Singh, and A. King, "Grain rotation in thin films of gold," *Acta materialia*, vol. 46, no. 8, pp. 2623–2633, 1998.

[45] J. W. Cahn and Y. Mishin, "Recrystallization initiated by low-temperature grain boundary motion coupled to stress," *International Journal of Materials Research*, vol. 100, no. 4, pp. 510–515, 2009.

[46] L. Margulies, G. Winther, and H. Poulsen, "In situ measurement of grain rotation during deformation of polycrystals," *Science*, vol. 291, no. 5512, pp. 2392–2394, 2001.

[47] P. Liu, S. Mao, L. Wang, X. Han, and Z. Zhang, "Direct dynamic atomic mechanisms of strain-induced grain rotation in nanocrystalline, textured, columnar-structured thin gold films," *Scripta Materialia*, vol. 64, no. 4, pp. 343–346, 2011.

[48] C. Rae and D. Smith, "On the mechanisms of grain boundary migration," *Philosophical Magazine A*, vol. 41, no. 4, pp. 477–492, 1980.

[49] J. W. Cahn and J. E. Taylor, "A unified approach to motion of grain boundaries, relative tangential translation along grain boundaries, and grain rotation," *Acta Materialia*, vol. 52, no. 16, pp. 4887–4898, 2004.

[50] D. Caillard, F. Mompiou, and M. Legros, "Grain-boundary shear-migration coupling. ii. geometrical model for general boundaries," *Acta Materialia*, vol. 57, no. 8, pp. 2390–2402, 2009.

[51] Y. Liu, X. Zou, and B. I. Yakobson, "Dislocations and grain boundaries in two-dimensional boron nitride," *ACS nano*, vol. 6, no. 8, pp. 7053–7058, 2012.

[52] Z. Trautt and Y. Mishin, "Grain boundary migration and grain rotation studied by molecular dynamics," *Acta Materialia*, vol. 60, no. 5, pp. 2407–2424, 2012.

[53] M. L. Falk and J. S. Langer, "Dynamics of viscoplastic deformation in amorphous solids," *Physical Review E*, vol. 57, no. 6, p. 7192, 1998.

[54] L. A. Barrales-Mora, J.-E. Brandenburg, and D. A. Molodov, "Impact of grain boundary character on grain rotation," *Acta Materialia*, vol. 80, pp. 141–148, 2014.

[55] L. A. Barrales-Mora and D. A. Molodov, "Capillarity-driven shrinkage of grains with tilt and mixed boundaries studied by molecular dynamics," *Acta Materialia*, vol. 120, pp. 179–188, 2016.

[56] J.-E. Brandenburg, L. Barrales-Mora, and D. Molodov, "On migration and faceting of low-angle grain boundaries: Experimental and computational study," *Acta Materialia*, vol. 77, pp. 294–309, 2014.

[57] K.-A. Wu and P. W. Voorhees, "Phase field crystal simulations of nanocrystalline grain growth in two dimensions," *Acta Materialia*, vol. 60, no. 1, pp. 407–419, 2012.

[58] M. Upmanyu, D. J. Srolovitz, A. Lobkovsky, J. A. Warren, and W. Carter, "Simultaneous grain boundary migration and grain rotation," *Acta Materialia*, vol. 54, no. 7, pp. 1707–1719, 2006.

[59] M. Upmanyu, R. Smith, and D. J. Srolovitz, "Atomistic simulation of curvature driven grain boundary migration," *Interface Science*, vol. 6, no. 1-2, pp. 41–58, 1998.

[60] Z. Trautt and Y. Mishin, "Capillary-driven grain boundary motion and grain rotation in a tricrystal: a molecular dynamics study," *Acta Materialia*, vol. 65, pp. 19–31, 2014.

[61] B. B. Rath, M. Winning, and J. Li, "Coupling between grain growth and grain rotation," *Applied physics letters*, vol. 90, no. 16, p. 161915, 2007.

[62] F. Mompiou, M. Legros, T. Radetic, U. Dahmen, D. Gianola, and K. Hemker, "In situ tem observation of grain annihilation in tricrystalline aluminum films," *Acta Materialia*, vol. 60, no. 5, pp. 2209–2218, 2012.

[63] T. Radetic, C. Ophus, D. Olmsted, M. Asta, and U. Dahmen, "Mechanism and dynamics of shrinking island grains in mazed bicrystal thin films of au," *Acta Materialia*, vol. 60, no. 20, pp. 7051–7063, 2012.

[64] S. Nosé, "A molecular dynamics method for simulations in the canonical ensemble," *Molecular physics*, vol. 52, no. 2, pp. 255–268, 1984.

[65] W. G. Hoover, "Constant-pressure equations of motion," *Physical Review A*, vol. 34, no. 3, p. 2499, 1986.

[66] J. W. Cahn, Y. Mishin, and A. Suzuki, "Coupling grain boundary motion to shear deformation," *Acta materialia*, vol. 54, no. 19, pp. 4953–4975, 2006.

[67] P. Clapp and J. Rifkin, "Nucleation of a martensite in a computer," *Solid to Solid Phase Transformations*, pp. 1165–1169, 1981.

[68] ——, "Simulated martensitic transformations," *MRS Online Proceedings Library Archive*, vol. 21, 1983.

[69] J. P. F. Rifkin, J. G. A. Kenyon, L. Tanner *et al.*, "Computer study of tweed as a precursor to a martensitic transformation of a bcc lattice," *Metallurgical Transactions A*, vol. 19, no. 4, pp. 783–787, 1988.

[70] S. Rubini and P. Ballone, "Quasiharmonic and molecular-dynamics study of the martensitic transformation in ni-al alloys," *Physical Review B*, vol. 48, no. 1, p. 99, 1993.

[71] R. Meyer and P. Entel, "Martensite-austenite transition and phonon dispersion curves of fe 1- x ni x studied by molecular-dynamics simulations," *Physical Review B*, vol. 57, no. 9, p. 5140, 1998.

[72] P. Entel, R. Meyer, and K. Kadau, "Molecular dynamics simulations of martensitic transitions," *Philosophical Magazine B*, vol. 80, no. 2, pp. 183–194, 2000.

[73] P. Entel, R. Meyer, K. Kadau, H. Herper, and E. Hoffmann, "Martensitic transformations: first-principles calculations combined with molecular-dynamics simulations," *The European Physical Journal B-Condensed Matter and Complex Systems*, vol. 5, no. 3, pp. 379–388, 1998.

[74] M. Grujicic and P. Dang, "Computer simulation of martensitic transformation in fe-ni face-centered cubic alloys," *Materials Science and Engineering: A*, vol. 201, no. 1-2, pp. 194–204, 1995.

[75] ——, "Atomic-scale analysis of martensitic transformation in titanium alloyed with vanadium part ii: molecular dynamics simulations," *Materials Science and Engineering: A*, vol. 205, no. 1-2, pp. 153–165, 1996.

[76] J. Morris and K. Ho, "Molecular dynamic simulation of a homogeneous bcc $\rightarrow$ hcp transition," *Physical Review B*, vol. 63, no. 22, p. 224116, 2001.

[77] M. Zelazny, R. Richardson, and G. Ackland, "Twinning hierarchy, shape memory, and superelasticity demonstrated by molecular dynamics," *Physical Review B*, vol. 84, no. 14, p. 144113, 2011.

[78] U. Pinsook and G. Ackland, "Simulation of martensitic microstructural evolution in zirconium," *Physical Review B*, vol. 58, no. 17, p. 11252, 1998.

[79] ——, "Atomistic simulation of shear in a martensitic twinned microstructure," *Physical Review B*, vol. 62, no. 9, p. 5427, 2000.

[80] G. J. Ackland, A. Jones, and R. Noble-Eddy, "Molecular dynamics simulations of the martensitic phase transition process," *Materials Science and Engineering: A*, vol. 481, pp. 11–17, 2008.

[81] K. R. Morrison, M. J. Cherukara, K. G. Vishnu, and A. Strachan, "Role of atomic variability and mechanical constraints on the martensitic phase transformation of a model disordered shape memory alloy via molecular dynamics," *Acta Materialia*, vol. 69, pp. 30–36, 2014.

[82] K. R. Morrison, M. J. Cherukara, H. Kim, and A. Strachan, "Role of grain size on the martensitic transformation and ultra-fast superelasticity in shape memory alloys," *Acta Materialia*, vol. 95, pp. 37–43, 2015.

[83] X. Ding, T. Suzuki, X. Ren, J. Sun, and K. Otsuka, "Precursors to stress-induced martensitic transformations and associated superelasticity: Molecular dynamics simulations and an analytical theory," *Physical Review B*, vol. 74, no. 10, p. 104111, 2006.

[84] L. Gao, X. Ding, H. Zong, T. Lookman, J. Sun, X. Ren, and A. Saxena, "Diffuse scattering as an indicator for martensitic variant selection," *Acta Materialia*, vol. 66, pp. 69–78, 2014.

[85] J. Ren, Q. Sun, L. Xiao, X. Ding, and J. Sun, "Phase transformation behavior in titanium single-crystal nanopillars under [0 0 0 1] orientation tension: A molecular dynamics simulation," *Computational Materials Science*, vol. 92, pp. 8–12, 2014.

[86] H. Zong, T. Lookman, X. Ding, C. Nisoli, D. Brown, S. R. Niezgoda, and S. Jun, "The kinetics of the ω to α phase transformation in zr, ti: Analysis of data from shock-recovered samples and atomistic simulations," *Acta Materialia*, vol. 77, pp. 191–199, 2014.

[87] G.-F. Ma, S.-J. Qin, J.-X. Shang, F.-H. Wang, and Y. Chen, "Atomistic study on the phase transformation in niti under thermal cycling," *Journal of Alloys and Compounds*, vol. 705, pp. 218–225, 2017.

[88] Y. Li, J. Li, and B. Liu, "Homogeneous shear-driven reversible α-to-α phase transformation and superelasticity of titanium investigated by molecular dynamics simulations," *Acta Materialia*, vol. 93, pp. 105–113, 2015.

[89] W.-S. Ko, S. B. Maisel, B. Grabowski, J. B. Jeon, and J. Neugebauer, "Atomic scale processes of phase transformations in nanocrystalline niti shape-memory alloys," *Acta Materialia*, vol. 123, pp. 90–101, 2017.

[90] W.-S. Ko, B. Grabowski, and J. Neugebauer, "Development and application of a ni-ti interatomic potential with high predictive accuracy of the martensitic phase transition," *Physical Review B*, vol. 92, no. 13, p. 134107, 2015.

[91] W. Petry, A. Heiming, J. Trampenau, M. Alba, C. Herzig, H. Schober, and G. Vogl, "Phonon dispersion of the bcc phase of group-iv metals. i. bcc titanium," *Physical Review B*, vol. 43, no. 13, p. 10933, 1991.

[92] M. Pitteri and G. Zanzotto, *Continuum models for phase transitions and twinning in crystals*. Chapman and Hall/CRC, 2002.

[93] W. Burgers, "On the process of transition of the cubic-body-centered modification into the hexagonal-close-packed modification of zirconium," *Physica*, vol. 1, no. 7-12, pp. 561–586, 1934.

[94] R. Shi and Y. Wang, "Variant selection during α precipitation in ti–6al–4v under the influence of local stress–a simulation study," *Acta Materialia*, vol. 61, no. 16, pp. 6006–6024, 2013.

[95] T. Furuhara, H. Kawata, S. Morito, and T. Maki, "Crystallography of upper bainite in fe–ni–c alloys," *Materials Science and Engineering: A*, vol. 431, no. 1-2, pp. 228–236, 2006.

[96] K. Bhattacharya, *Microstructure of martensite: why it forms and how it gives rise to the shape-memory effect*. Oxford University Press, 2003, vol. 2.

[97] P. M. Larsen, S. Schmidt, and J. Schiøtz, "Robust structural identification via polyhedral template matching," *Modelling and Simulation in Materials Science and Engineering*, vol. 24, no. 5, p. 055007, 2016.

[98] J.-F. Wu, C.-W. Yang, C.-S. Chen, and N.-T. Tsou, "The variant identification in molecular dynamics simulations for shape memory alloys."

[99] G. J. Ackland, "Theoretical study of titanium surfaces and defects with a new many-body potential," *Philosophical Magazine A*, vol. 66, no. 6, pp. 917–932, 1992.

[100] S. Wooding, D. Bacon, and W. Phythian, "A computer simulation study of displacement cascades in α-titanium," *Philosophical Magazine A*, vol. 72, no. 5, pp. 1261–1279, 1995.

[101] A. Girshick, D. Pettifor, and V. Vitek, "Atomistic simulation of titanium. ii. structure of $1/3\langle 1210\rangle$ screw dislocations and slip systems in titanium," *Philosophical Magazine A*, vol. 77, no. 4, pp. 999–1012, 1998.

[102] A. Ready, A. Sutton, P. Haynes, and D. Rugg, "Point, linear and planar defects in titanium," in *Proceedings of the 13th World Conference on Titanium*. Wiley Online Library, 2016, pp. 1029–1034.

[103] X. Zhou, R. Johnson, and H. Wadley, "Misfit-energy-increasing dislocations in vapor-deposited cofe/nife multilayers," *Physical Review B*, vol. 69, no. 14, p. 144113, 2004.

[104] M. Mendelev, T. Underwood, and G. Ackland, "Development of an interatomic potential for the simulation of defects, plasticity, and phase transformations in titanium," *The Journal of chemical physics*, vol. 145, no. 15, p. 154102, 2016.

[105] R. Hennig, T. Lenosky, D. Trinkle, S. Rudin, and J. Wilkins, "Classical potential describes martensitic phase transformations between the α, β, and ω titanium phases," *Physical Review B*, vol. 78, no. 5, p. 054121, 2008.

[106] T. Andersson, "One-shot free of energy calculations for techniques crystalline materials," 2012.

[107] S. Goedecker, "Optimization and parallelization of a force field for silicon using openmp," *arXiv preprint cond-mat/0201475*, 2002.

[108] T. J. Lenosky, B. Sadigh, E. Alonso, V. V. Bulatov, T. D. de la Rubia, J. Kim, A. F. Voter, and J. D. Kress, "Highly optimized empirical potential model of silicon," *Modelling and Simulation in Materials Science and Engineering*, vol. 8, no. 6, p. 825, 2000.

[109] K. Madangopal, J. Singh, and S. Banerjee, "Self-accommodation in ni ti shape memory alloys," *Scripta metallurgica et materialia*, vol. 25, no. 9, pp. 2153–2158, 1991.

[110] Y. Chai, H. Kim, H. Hosoda, and S. Miyazaki, "Self-accommodation in ti–nb shape memory alloys," *Acta Materialia*, vol. 57, no. 14, pp. 4054–4064, 2009.

[111] V. Pancholi, M. Krishnan, I. Samajdar, V. Yadav, and N. Ballal, "Self-accommodation in the bainitic microstructure of ultra-high-strength steel," *Acta Materialia*, vol. 56, no. 9, pp. 2037–2050, 2008.

[112] N. Takayama, G. Miyamoto, and T. Furuhara, "Effects of transformation temperature on variant pairing of bainitic ferrite in low carbon steel," *Acta Materialia*, vol. 60, no. 5, pp. 2387–2396, 2012.

[113] J. Morris, Y. Ye, K. Ho, C. T. Chan, and M. Yoo, "Structures and energies of compression twin boundaries in hcp ti and zr," *Philosophical Magazine A*, vol. 72, no. 3, pp. 751–763, 1995.

[114] K. Bhattacharya, "Self-accommodation in martensite," *Archive for Rational Mechanics and Analysis*, vol. 120, no. 3, pp. 201–244, 1992.

[115] Z. Nishiyama, S. Sato, M. Oka, and H. Nakagawa, "Transmission electron microscope study of the martensites in a titanium-3 wt% iron alloy," *Transactions of the Japan Institute of Metals*, vol. 8, no. 2, pp. 127–132, 1967.

Appendix A

Dimensionless equation

For the model implementation, we introduce dimensionless variables.

Let E_0 being a generic unit of energy, σ a unit of length. In the following, we will highlight dimensionless quantities by the symbol $\hat{}$. For example, dimensionless atom coordinates, lengths, potential energy and temperature are defined as:

$$\hat{x}_i^n = \frac{x_i^n}{\sigma}, \quad \hat{L} = \frac{L}{\sigma}, \quad \hat{\Phi} = \frac{\Phi}{E_0}, \quad \hat{T} = \frac{k_B T}{E_0}$$

We firstly consider equations (2.4.16) and rewrite them as:

$$\frac{\partial \tilde{x}_i^n}{\partial t} = -\nu E_0 \frac{\partial \hat{\tilde{H}}}{\partial \tilde{x}_i^n} + \sqrt{2\nu \hat{T} E_0}\eta_i^n(t) \tag{A.0.1}$$

We introduce the adimensional time:

$$\hat{t} = \nu E_0 t \tag{A.0.2}$$

Provided that:

$$\hat{\eta}_i^n(\hat{t}) = \frac{1}{\sqrt{\nu E_0}}\eta_i^n(t) \tag{A.0.3}$$

$\hat{\eta}_i^n(\hat{t})$ inherits the same statistical properties of $\eta_i^n(t)$:

$$\begin{cases} \langle \hat{\eta}_i^n(\hat{t}) \rangle = 0 \\ \langle \hat{\eta}_i^n(\hat{t}) \hat{\eta}_j^m(\hat{t}') \rangle = \frac{1}{\nu E_0} \langle \eta_i^n \left(\frac{\hat{t}}{\nu E_0} \right) \eta_j^m \left(\frac{\hat{t}'}{\nu E_0} \right) \rangle = \frac{1}{\nu E_0} \delta \left(\frac{\hat{t} - \hat{t}'}{\nu E_0} \right) = \delta \left(\hat{t} - \hat{t}' \right) \end{cases} \tag{A.0.4}$$

Substituting equations (A.0.2) and (A.0.3) in equation (A.0.1) we get the dimensionless Langevin equations for variables $\tilde{x}_i^n$:

$$\frac{\partial \tilde{x}_i^n}{\partial \hat{t}} = -\frac{\partial \hat{\tilde{H}}}{\partial \tilde{x}_i^n} + \sqrt{2\hat{T}}\hat{\eta}_i^n(\hat{t}) \tag{A.0.5}$$

With a similar procedure, from equations (2.4.17) we obtain the dimensionless equations for the deformation gradient components $F_{\alpha\beta}$:

$$\begin{aligned}\frac{\partial F_{\alpha\beta}}{\partial t} &= -\gamma E_0 \frac{\partial \hat{\tilde{H}}}{\partial F_{\alpha_\beta}} + \sqrt{2\gamma \hat{T} E_0}\zeta_{\alpha\beta} \\ &= -\frac{\gamma}{\nu}\frac{\partial \hat{\tilde{H}}}{\partial F_{\alpha\beta}} + \sqrt{\frac{2\gamma\hat{T}}{\nu}}\hat{\zeta}(\tilde{t})\end{aligned} \tag{A.0.6}$$

with:

$$\frac{\partial \hat{\tilde{H}}}{\partial F_{\alpha\beta}} = \sum_{n=1}^{N} \frac{\partial \hat{\Phi}}{\partial \hat{x}_\alpha^n}\hat{L}_\beta \tilde{x}_\beta^n + \hat{V}_0 \hat{P}_{\alpha\beta} - N\hat{T}\frac{C_{\alpha\beta}}{\det \mathbf{F}}(-1)^{\alpha+\beta} \tag{A.0.7}$$